Effective Date: June 27, 2025
Expiration Date: June 27, 2030

GSFC RST CMO
July 18, 2025
Released

RST-WFI-HDBK-0186, Revision -

Roman Space Telescope (RST), Code 448

RST Wide Field Instrument (WFI) Focal Plane Array Handbook

Roman Space Telescope Reviewed – Not Subject to Export Control

Goddard Space Flight Center
Greenbelt, Maryland

National Aeronautics and Space Administration

RST Wide Field Instrument (WFI) Focal Plane Array Handbook

Review/Signature/Approval Page

Prepared by:

Stephanie Cheung – GSFC 540, Relative Dynamics Inc.
Gregory Mosby – GSFC 665
Analia Cillis – GSFC 553, University of Maryland, Baltimore County
Michael Hickey – GSFC 554
Thushara Perera – GSFC 448, Conceptual Analytics LLC.
Mario Cabrera – Teledyne Imaging, formerly GSFC 448
Bernard Rauscher – GSFC 665

Approving Signature Authority:

John Gygax – GSFC 448

Electronic Approval available on-line at: https://ipdtdms.gsfc.nasa.gov

Preface

This document is a Roman Space Telescope (RST) Configuration Management (CM)-controlled document.

Note: Prior to May 20, 2020, the project name was Wide Field Infrared Survey Telescope (WFIRST).

For the purposes of configuration management, the prefixes “WFIRST” and “RST” are completely interchangeable. For example, RST-MGMT-PROC-0024 is the same as WFIRST-MGMT-PROC-0024.

Changes to this document require prior approval of the applicable Signature Authority or designee. Proposed changes shall be submitted to the RST CM Office (CMO), along with supportive material justifying the proposed change.

In this document, a requirement is identified by “shall,” a good practice by “should,” permission by “may” or “can,” expectation by “will,” and descriptive material by “is.”

Questions or comments concerning this document should be addressed to:

RST Configuration Management Office
Mail Stop 448
Goddard Space Flight Center
Greenbelt, Maryland 20771

Change History Log

Revision	Effective Date	Description of Changes (Reference the Signature Authority Approval Date)
Revision -	June 27, 2025	This initial version incorporates RST-SCoRe-8889. This was approved by the signature authority on the effective date shown.

Table of TBDs/TBRs/TBSs [optional]

Item No.	Location	Summary	Individual/ Organization Actionee	Due Date

Table of Contents

List of Figures

List of Tables

1 INTRODUCTION

1.1 Purpose

This document describes characteristics of the Roman Space Telescope (RST) Wide Field Instrument (WFI) Focal Plane Array (FPA). It is intended to be used as a reference by anyone analyzing Sensor Chip Assembly (SCA) detector data and includes analysis and results from SCA, Triplet, FPA, and WFI level testing.

1.2 Scope

This document will describe analysis methods for various metrics of the SCAs. Each section will include a summary of overall performance of the FPA, and sub-sections will have details on each detector's individual performance and quirks.

1.3 Related Documentation

The latest versions of all documents below should be used. RST documents can be obtained from URL: https://ipdtdms.gsfc.nasa.gov.

1.4 Applicable Documents

The following documents are referenced within this document and are directly applicable or contain policies or other directive matters that are binding for the contents of this document. In the event of conflict between an Applicable Document and the content of this document, the applicable Signature Authority has the final authority for conflict resolution.

Document Number	Title

1.4.1 Reference Documents

The following documents are referenced herein and amplify or clarify the information presented in this document. These documents are not binding on the content of this document.

Document Number	Title
RST-WFI-RPT-1375	DCL Acceptance Test Report SCA 22081
RST-WFI-RPT-0352	DCL Acceptance Test Report SCA 21815
RST-WFI-RPT-0424	DCL Acceptance Test Report SCA 21946
RST-WFI-RPT-1376	DCL Acceptance Test Report SCA 21115
RST-WFI-RPT-0405	DCL Acceptance Test Report SCA 21816
RST-WFI-RPT-0342	DCL Acceptance Test Report SCA 20663
RST-WFI-RPT-0452	DCL Acceptance Test Report SCA 22069
RST-WFI-RPT-0423	DCL Acceptance Test Report SCA 21641
RST-WFI-RPT-0404	DCL Acceptance Test Report SCA 21813
RST-WFI-RPT-0484	DCL Acceptance Test Report SCA 22078
RST-WFI-RPT-0406	DCL Acceptance Test Report SCA 21947
RST-WFI-RPT-0343	DCL Acceptance Test Report SCA 20829
RST-WFI-RPT-0433	DCL Acceptance Test Report SCA 22067
RST-WFI-RPT-0351	DCL Acceptance Test Report SCA 21814
RST-WFI-RPT-0350	DCL Acceptance Test Report SCA 21645

Document Number	Title
RST-WFI-RPT-0349	DCL Acceptance Test Report SCA 21643
RST-WFI-RPT-0356	DCL Acceptance Test Report SCA 21319
RST-WFI-RPT-0353	DCL Acceptance Test Report SCA 20833
RST-WFI-RPT-1291	Triplet Test Report (SCA 21815)
RST-WFI-RPT-1077	Triplet Test Report H4RG 21946
RST-WFI-RPT-1076	Triplet Test Report H4RG 21816
RST-WFI-RPT-0735	Triplet Test Report on SCA 20663
RST-WFI-RPT-1078	Triplet Test Report H4RG 22069
RST-WFI-RPT-1075	Triplet Test Report H4RG 21641
RST-WFI-RPT-0740	Triplet Test Report on SCA 21813
RST-WFI-RPT-0738	Triplet Test Report on SCA 22078
RST-WFI-RPT-0741	Triplet Test Report on SCA 21947
RST-WFI-RPT-1396	Triplet Testing Report (SCA 20829)
RST-WFI-RPT-0736	Triplet Test Report on SCA 22067
RST-WFI-RPT-1290	Triplet Test Report (SCA 21814)
RST-WFI-RPT-1289	Triplet Test Report (SCA 21645)
RST-WFI-RPT-0739	Triplet Test Report on SCA 21643
RST-WFI-RPT-0737	Triplet Report on SCA 21319
RST-WFI-RPT-1288	Triplet Test Report (SCA 20833)
RST-WFI-RPT-0546	Flight Mosaic Plate Assembly Metrology and Alignment Summary
RST-WFI-RPT-1351	Wide Field Instrument (WFI) Focal Plane System (FPS) Detector Dark Anomaly Review Board (DD-ARB) Final Report
RST-WFI-RPT-1815	RWFI-429/RSRCS-429 Requirement Verification Status
RST-WFI-RPT-0364	WFIRST Report FDNL 20833 Ma6 (DCL)
RST-WFI-RPT-0582	FDNL Test Report (DCL 21813)
RST-WFI-RPT-0635	FDNL Report (DCL 21645)
RST-WFI-RPT-0638	FDNL Report (DCL 21816)
RST-WFI-RPT-0639	FDNL Report (DCL 21814)
RST-WFI-RPT-0640	FDNL Report (DCL 21815)
RST-WFI-RPT-0642	FDNL Report (DCL 21643)
RST-WFI-RPT-0649	FDNL Report (DCL 21641)
RST-WFI-RPT-0650	FDNL Report (DCL 21946)
RST-WFI-RPT-0651	FDNL Report (DCL 22067)
RST-WFI-RPT-0653	FDNL Report (DCL 21319)
RST-WFI-RPT-0657	FDNL Report (DCL 20829)
RST-WFI-RPT-0670	FDNL Report (DCL 22078)
RST-WFI-RPT-0671	FDNL Report (DCL 22069)
RST-WFI-RPT-0722	FDNL Report (DCL 20663)
RST-WFI-TN-0597	RST FPS Persistence Characterization

Document Number	Title
RST-WFI-TN-0621	RST Flight Detectors Dark Current Trending
RST-WFI-TN-0620	RST Flight Detectors CDS Noise Trending
RST-WFI-TN-0619	RST Flight Detectors Total Noise Trending
RST-SCI-ANYS-0481	Roman Space Telescope Wide-Field Instrument Flight Sensor Chip Assembly Selection and Placement Overview

2 INTRO TO THE FPA

2.1 Assembly and Test Campaigns

The FPA is the heart of RST's WFI and consists of 18 HgCdTe (MCT) H4RG detectors and their associated Sensor Control Electronics (SCEs). Prior to FPA integration each SCA was subjected to multiple rounds of testing at the Detector Characterization Lab (DCL) at GSFC. *Properties and Characteristics of the Nancy Grace Roman Space Telescope H4RG-10 Detectors* (Mosby et al., 2020) covers additional information on the design and testing of the WFI detectors. All detector testing was conducted with a bias voltage of 1.0V, unless otherwise specified.

Acceptance testing of the SCAs with Leach electronics measured power dissipation, Correlated Double Sampling (CDS) and total noise, Quantum Efficiency (QE), linearity, dark current, persistence, Inter-Pixel Capacitance (IPC), pixel crosstalk, and guide window functionality. The nominal SCA operating temperature was 95K. The acceptance test reports are available on TDMS, their document numbers are listed in the table in Section 1.4.1.

Separately from acceptance testing most SCAs were also tested for Flux Dependent Non-Linearity (FDNL), which is covered in more detail in Section 8.2. The FDNL test reports are available on TDMS, their document numbers are listed in the table in Section 1.4.1.

After acceptance testing the SCAs were tested again in "triplet" configuration, with each SCA connected to an ACADIA (ASIC for Control and Digitization for Astronomy) ASIC (Application Specific Integrated Circuit), also referred to as an SCE, via a flexible cable. Conversion gain, dynamic range, IPC, thermal sensitivity, total noise, guide window noise, dark current, linearity, photometric stability, and crosstalk were measured during triplet testing. The triplet test reports are available on TDMS, their document numbers are listed in the table in Section 1.4.1.

Twenty eight SCAs passed flight acceptance testing and became the pool from which to select the flight SCA complement. The selection of flight SCAs and their placement in the focal plane is described in the Roman Space Telescope Wide Field Instrument (WFI) Flight Sensor Chip Assembly (SCA) Selection and Placement Overview document - RST-SCI-ANYS-0481. Flight FPA integration started in October 2021. Each of the 18 SCAs had a light shield installed to cover the wire bonds, then were mounted onto the Mosaic Plate Assembly (MPA). An iterative process of metrology and spacer installation was used to optimize flatness across the MPA, documented in RST-WFI-RPT-0546. A flexible harness connects each SCA to its corresponding SCE, and all together they become the FPA.

After the flight FPA was assembled it was tested with the Engineering Test Unit (ETU) Focal Plane Electronics (FPE) at GSFC between 12/6/2022-12/21/2022. This thermal vacuum (TVAC) test is often referred to as the "semiflight" Focal Plane System (FPS) test due to the mix of flight and ETU components. Detector data was collected at a temperature of 95K in both dark and flat-field illuminated conditions. During this test, it became apparent that multiple detectors were suffering from dark current degradation, and a Detector Degradation Anomaly Review Board (DD-ARB) was created to investigate the problem. The direction from the DD-ARB was to replace three of the 18 SCAs on the flight FPA, in locations 1, 4, and 12. The final report from

the DD-ARB is documented in RST-WFI-RPT-1351. A public conference proceeding on the DD-ARB findings was also published in *Resolving the Dark Current Anomaly in the Nancy Grace Roman Space Telescope Focal Plane* (Mosby et al, 2024).

Figure 1: SCAs on the flight FPA

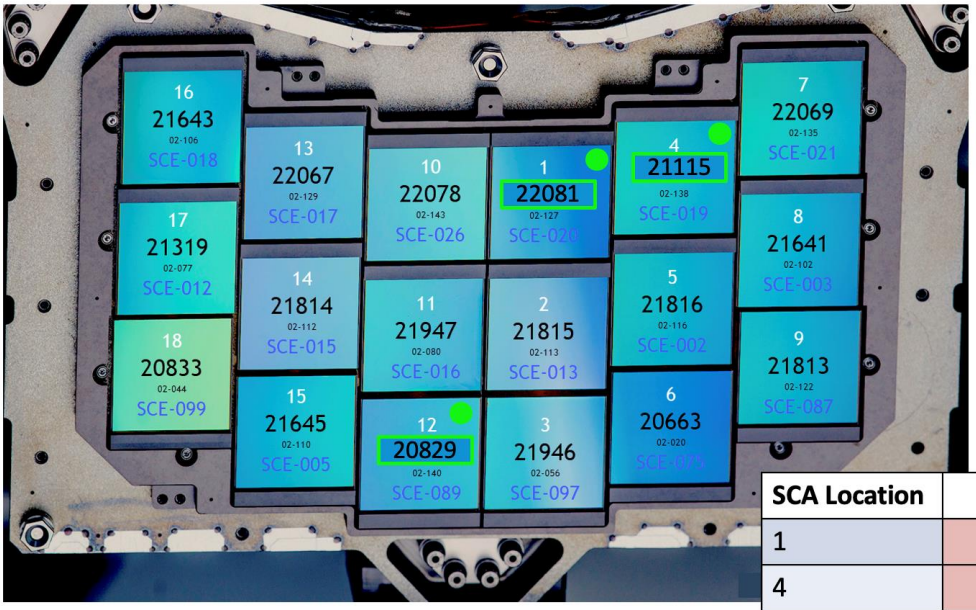

SCA Location	WAS	IS
1	22066	22081
4	22073	21115
12	22077	20829

Once re-assembly of the FPA was complete it was tested with the flight FPE between 4/14/2023-5/1/2023. The nominal temperature was 95K, but data were also collected during HotOp 101K and ColdOp 88/85K plateaus. After the flight FPS test was completed the flight FPS was shipped to BAE Systems (formerly Ball Aerospace) in Boulder, CO for integration into the WFI.
The WFI was subjected to two TVAC campaigns at BAE: TVAC1 between 9/11/2023-11/5/2023 and TVAC2 between 3/19/2024-4/7/2024. During these tests the detectors were tested in dark conditions and illuminated with the Stimulus of Ray Cones (SORC) and the simplified Relative Calibration System (sRCS). The nominal temperature of the MPA was also lowered to <90K.

Note: because of the file naming convention for FPS and WFI data, “SCA” and “SCU” (SCE Control Unit) are used interchangeably throughout this document.

The following table shows the tests that each detector has gone through in its lifetime. A green cell represents a test completed, and a white cell indicates that the SCA was not tested in that configuration.

Table 1: All SCA Test Campaigns

SCA #	SCA SN	Acceptance Testing (95K)	Triplet Testing (95K)	FDNL (95K)	Semiflight FPS (95K)	Flight FPS (95K)	WFI TVAC1 (89K)	WFI TVAC2 (89.5K)
1	22081							
2	21815							

3	21946							
4	21115							
5	21816							
6	20663							
7	22069							
8	21641							
9	21813							
10	22078							
11	21947							
12	20829							
13	22067							
14	21814							
15	21645							
16	21643							
17	21319							
18	20833							

2.2 Thermal

The temperature of the MPA is monitored and controlled by the FPE. The “primary” and “redundant” sensors are connected to the primary and redundant sides of the FPE. The diagram below shows the locations of the temperature sensors which are bonded to the back of the Mosaic Plate, with SCAs 16 and 7 included for orientation purposes. There are four heaters connected in parallel which are bonded to the sides of the Mosaic Plate, shown below in red.

Figure 2: MPA Thermal Diagram

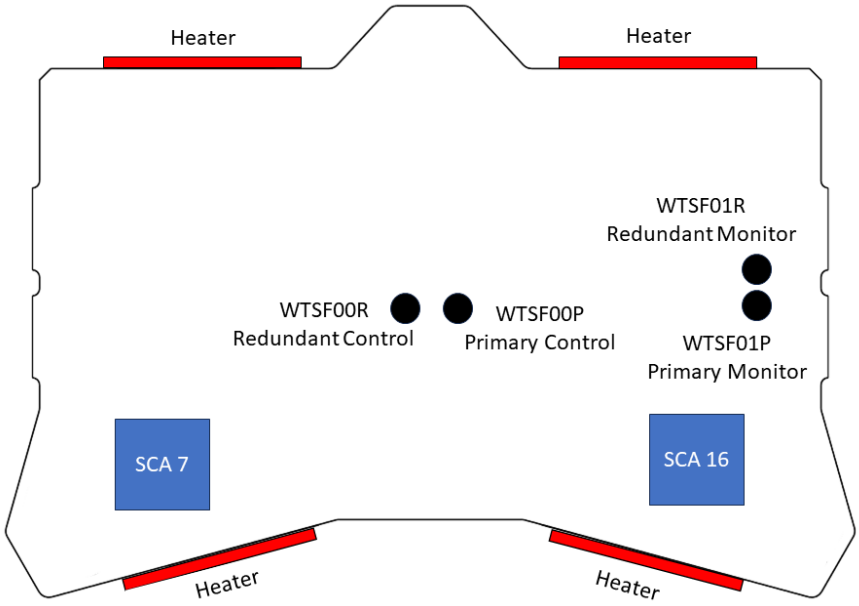

There are also two temperature sensors internal to each SCA: a serpentine resistor and a DT-670 sensor. These are monitored through telemetry points SCA_TEMP_V (serpentine resistor) and SCA_TISP_V (DT-670).
The temperature of the SCEs is also monitored by the FPE. The SCEs are mounted onto three shelves with 6 SCEs each. Primary and redundant monitor temperature sensors are bonded to the middle shelf, which holds the SCEs connected to SCAs 17, 14, 11, 2, 5, and 8. Each SCE also has an internal temperature sensor which is read out via telemetry point 40uA_4_V.

The average measured FPE-controlled temperature of the detectors and SCEs during each of the test campaigns is listed in the tables below.

Table 2: MPA Temperature During Test Campaigns

Test	Ambient	Bake Out	Cold	Nominal	Hot
Semi-flight	296	313	---	95	---
Flight FPS	296	---	88/85	95	101
WFI 1	296	---	88.8	89	95
WFI 2	296	---	89.5	89.5	92

Table 3: SCE Temperature During Test Campaigns

Test	Ambient	Bake Out	Cold	Nominal	Hot
Semi-flight	296	323	---	145	---
Flight FPS	296	---	138	147	162
WFI 1	296	---	148	153.3	164
WFI 2	296	---	150	152	160

2.3 Inspections

During FPA rework and SCA replacement following the DD-ARB, all the analog flex harnesses connecting the SCAs to the SCEs had to be removed. After removal of the analog flex harnesses inspection of the SCA connectors revealed that on SCA 21946 (SCA 3) the pin for output channel 13 was damaged. The damage and rework of this connector is documented in PR-RST-WFI-3490-001. The analog harness was successfully reconnected to SCA 21946, and subsequent testing has shown no adverse effects on data from this SCA.
The active area of each detector was photographed using a Nikon D850 with 100mm macro lens prior to installation of the FPA into the WFI. Various features in the detector material are visible, some of which appear in the data. The photos are attached to WOA-RST-WFI-3806, Event 170.

3 FUNCTIONAL TEST/CPT

The FPA was subjected to a suite of functional tests in ambient conditions at the beginning and end of each environmental test (including TVAC, vibration testing, and Electromagnetic Interference (EMI) testing). These data were also collected in cryogenic conditions during TVAC as part of Comprehensive Performance Testing (CPT). This included the following imaging tests:

- Shorted input noise
- 1-Frame detector data
- Test pattern data
- Guide window science
- Max rate compressed/uncompressed data
- Disconnected pixels (ambient test only)

3.1 Shorted Input Noise

During this test the inputs to the SCEs are shorted while the FPS collects a single exposure consisting of one reset-read frame and one science frame. This checks for any excessive noise on the SCE outputs, which is calculated as the standard deviation of the pixels in each output channel divided by the square root of 2. The noise is expected to be less than 3 Analog-Digital Units (ADU) in ambient conditions, and less than 2 when cold.

3.2 1-Frame Detector Data

This test is a single exposure consisting of one reset-read frame and one science frame. The intent was to verify that after the shorted input noise test the detectors were back in their expected state.

3.3 Test Pattern

This test sets the pixel values to a known pattern determined by the Multi-Accumulation (MA) table and collects a single exposure with one reset-read frame and one science frame. A data analysis script verifies that the data from the FPA matches the expected pattern.

Figure 3: Example of Test Pattern Image Data

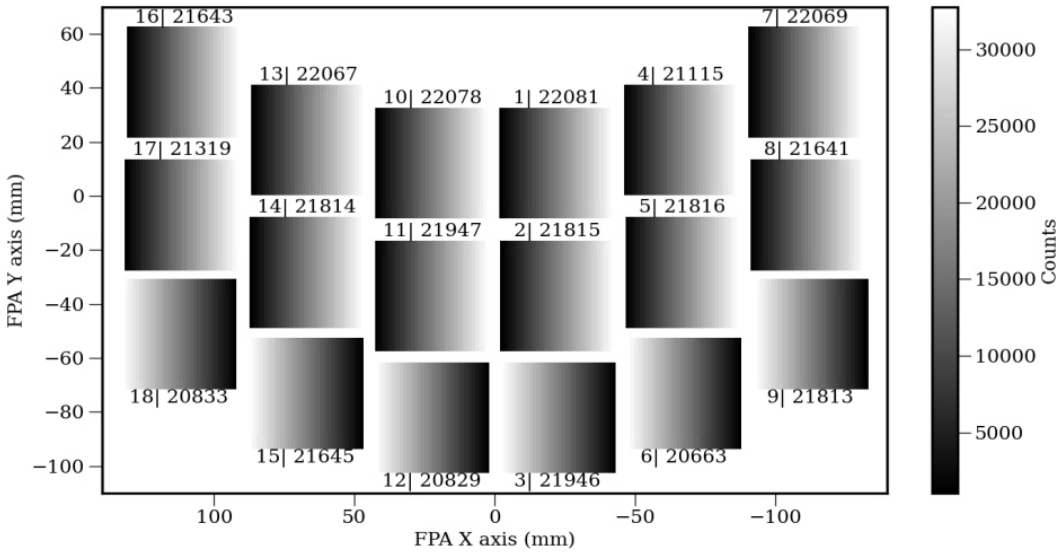

3.4 Guide Window Science

The guide window science test collects a set of exposures with guide window sizes set to 100x100, 64x64, and 16x16. Each guide window is placed over a known feature in the detector, and the locations of each guide window are unique. Coordinates of the guide window locations are listed in Appendix A. This test checks that the size, location, and quantity of the guide windows matches expectations, and that the guide window data are valid as determined by the presence of the known features. Additional information about the guide windows is covered in Section 16.

3.5 Max Rate Data

The max rate test collects compressed and uncompressed detector data, with and without guide windows. The analysis for these tests checks that all the detector data for the science frames and guide windows exists and that guide windows did not change size or position during the exposure.

3.6 Disconnected Pixels

The disconnected pixel test was conducted with the FPA at ambient temperature, as part of the ambient functional test at the beginning and end of each TVAC test campaign. For this test the Dsub voltage is varied from 0.35-0.55V in increments of 0.05V while Vreset is held stable. High dark current at ambient temperature causes the pixels to saturate to a value that depends on the difference between Dsub and Vreset, and a linear fit per pixel is calculated. An arbitrary threshold of 5σ is chosen as the pass/fail criteria, and pixels with slopes outside of 5σ of the median are considered failing or disconnected. While there is no formal requirement for the number of disconnected pixels in an SCA, disconnected pixels can be expected to fail the operability requirement which stipulates that at least 95% of the pixels across the SCA be operable. A summary of the disconnected pixel behavior in the flight SCAs is shown in the figure below.

Figure 4: Disconnected Pixels Summary

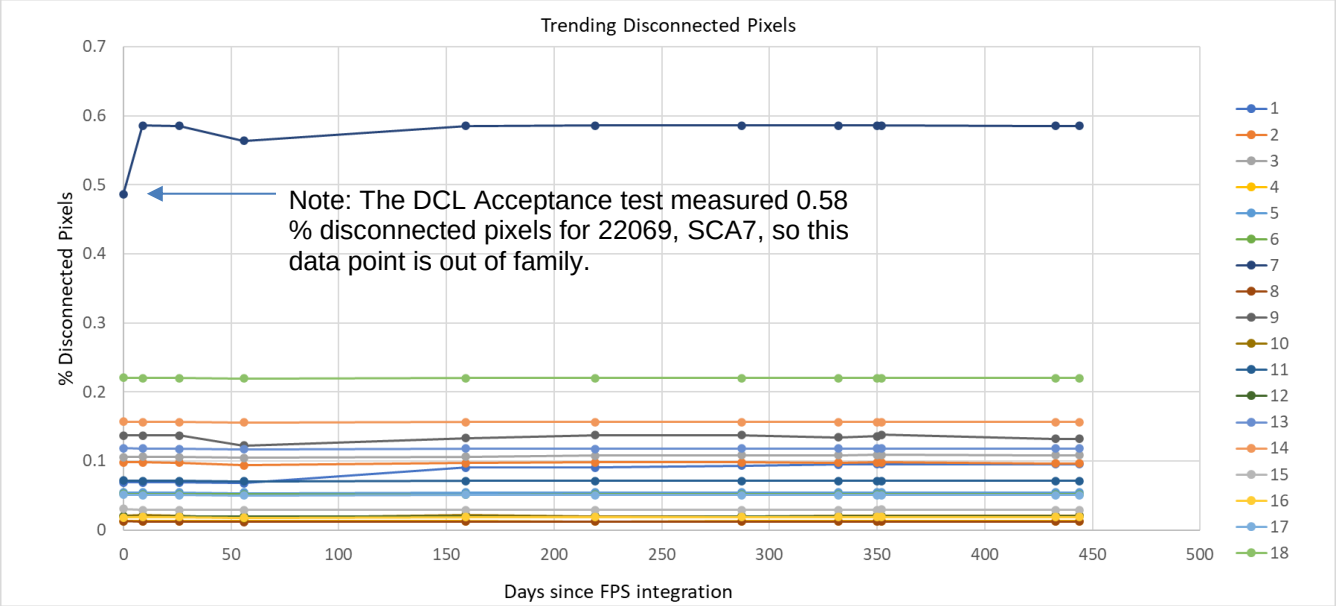

Some of the tests have produced out of family results. These include the Day 0 test when the flight FPA and FPE were connected for the first time, and the Day 56 post-ship to BAE test which was conducted with Markury electronics instead of the FPE.
The number of disconnected pixels has been stable in all SCAs except for SCA 1, 22081, where the number of disconnected pixels has increased over time.

3.7 Disconnected Pixels: SCA 1, 22081

The increasing trend of disconnected pixels in SCA 1 can be traced back to its first tests at the DCL, but the two largest increases happened after integration into the FPA/FPS and after integration into the WFI, before TVAC1.

Figure 5: Increasing disconnected pixels in SCA 1

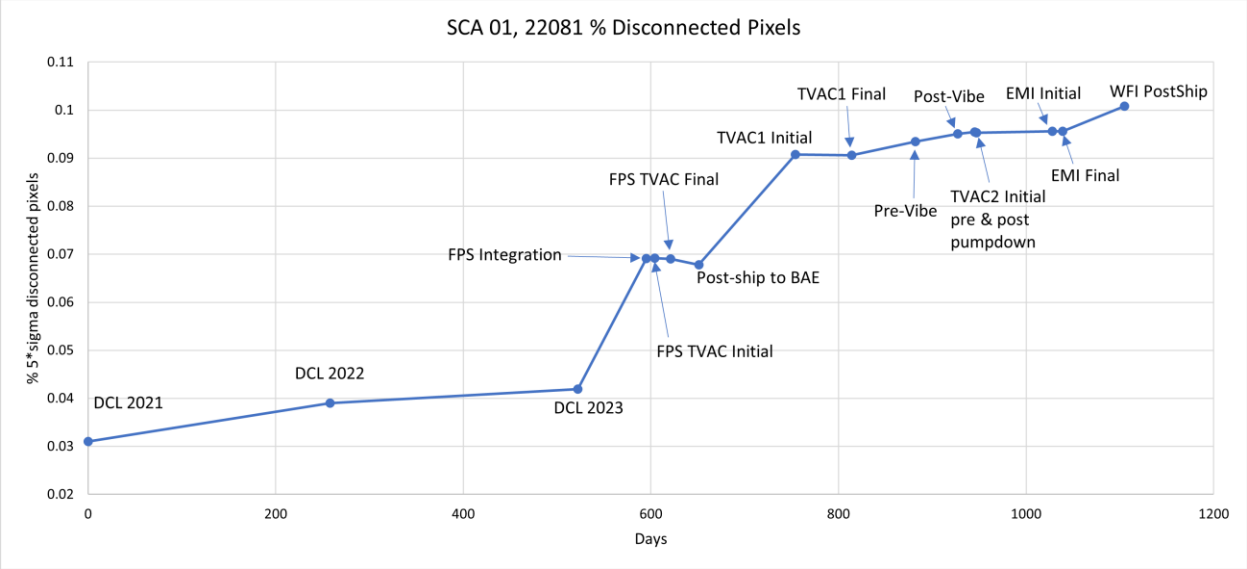

The locations of the disconnected pixels are shown in the figures below, where green pixels are passing/connected and black pixels are failing/disconnected. The new disconnected pixels, meaning the pixels that have become disconnected since flight FPS TVAC, are concentrated to areas of existing defects along the right and bottom edges of the detector.

Figure 6: Total disconnected pixels in SCA 1

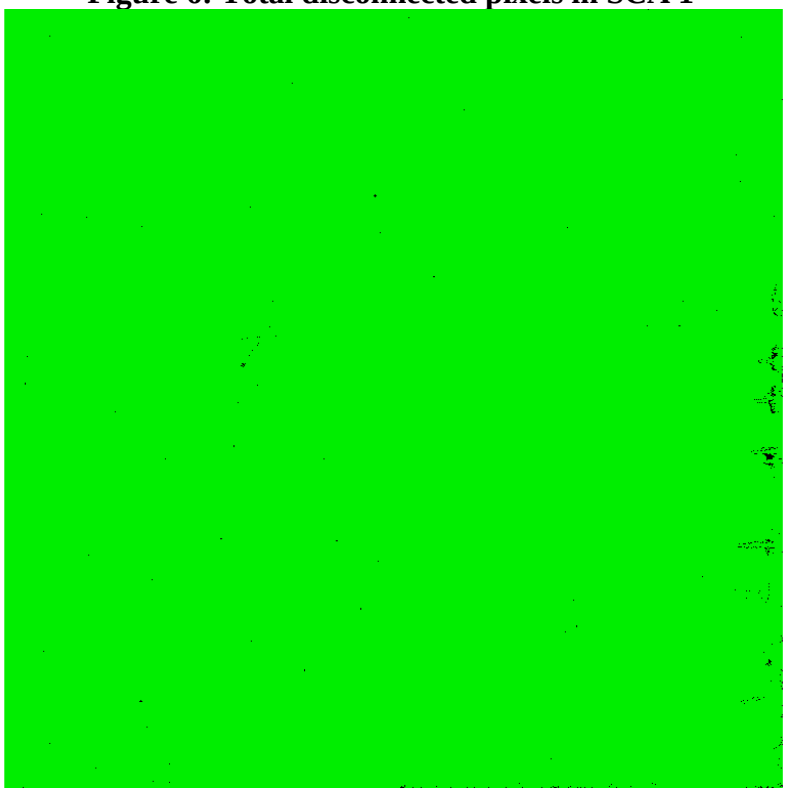

Figure 7: New disconnected pixels in SCA 1

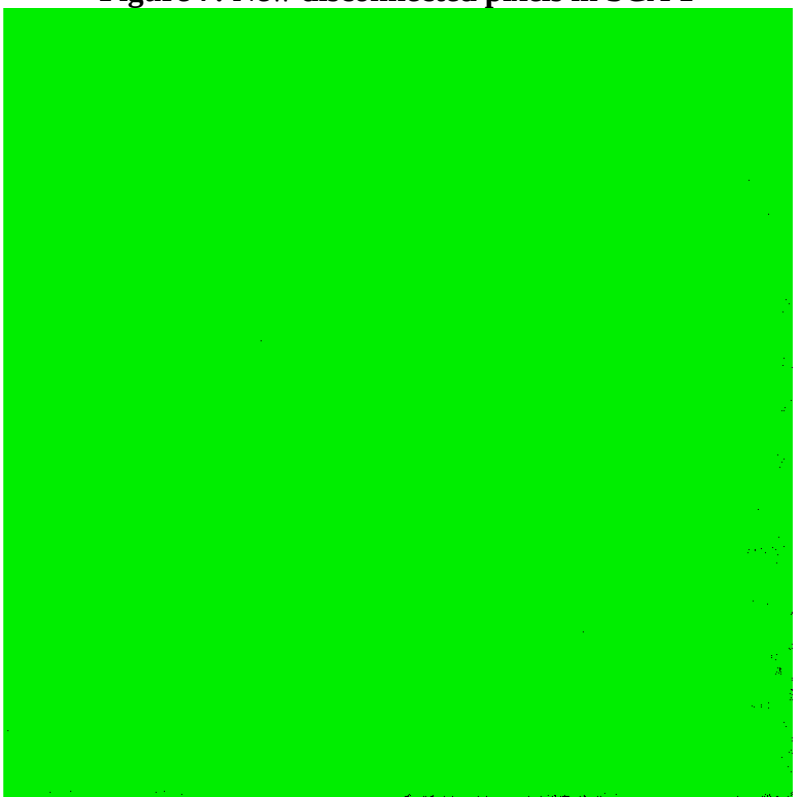

While the exact cause of the increasing disconnected pixels in this detector has not been determined, there are theories that it could be related to mechanical stress, or the degradation mechanism identified by the DD-ARB. The findings of the DD-ARB were that areas with existing defects are likely to get worse over time, and that exposure to temperatures exceeding 23C should be limited. The temperature in the clean room where the FPA integration work was done was not very well controlled, at times exceeding 23C. In contrast, the disconnected pixel increase was negligible during the WFI TVAC tests when the detectors were cold. In addition, the act of torquing the SCA to the Mosaic Plate, and the Mosaic Plate to the WFI, could have induced stress along the edges of the detector causing the increase in disconnected pixels along the edges during those time frames.
There is no evidence of dark current or QE degradation in the recently disconnected pixels prior to being flagged as disconnected. The figure below shows a histogram of disconnected pixels in WFI TVAC2 where the pixel value is from the last frame in a science monitor exposure when the rest of the detector was saturated, with dark current subtracted out. The median value of the histogram is approximately 2300 ADU and the distribution spans most of the A/D range, which suggests that most of the pixels that are being flagged as disconnected are still light sensitive when cold.

Figure 8: Response of recently disconnected pixels to illumination

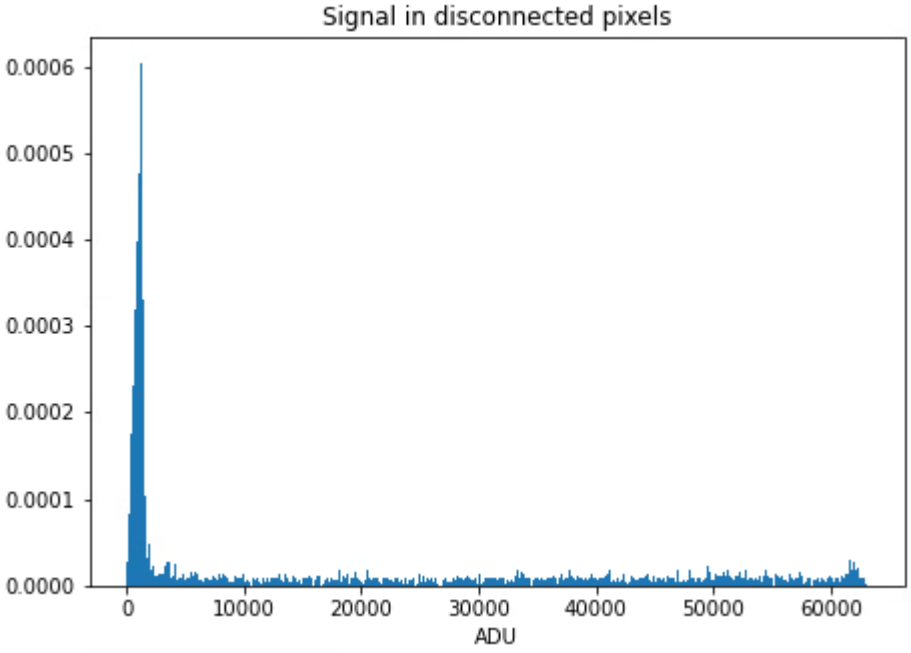

Although the number of disconnected pixels for this detector will likely continue to increase until launch, it should be a slow rate of increase if a well-controlled thermal environment is maintained and mechanical strain on the detectors/MPA is minimized. The rate of increase between the WFI TVAC1 and TVAC2 tests was approximately 600 new pixels failing/100 days, which should result in an overall increase of less than 5000 new disconnected pixels (0.03%) in two years if the trend continues. As of January 2025, the disconnected pixel test has been removed from the ambient functional test procedure out of an abundance of caution against applying bias voltage to the detectors while at ambient temperature.

4 REFERENCE PIXEL CORRECTION

The active area of each detector is bordered by 4 rows and 4 columns of pixels that are not photosensitive but otherwise identical to pixels in the active area. These are reference pixels used for correcting for drifts in the bias voltage. The method for reference pixel correction used during FPS and WFI testing is as follows:

1) Take the average of the top 4 rows of reference pixels in each 128-column wide output channel of the detector.
2) Subtract the average value of the reference pixels from all pixels in the channel.
3) Calculate the average of the left and right reference pixel columns (8 total), omitting the reference pixels at the top and bottom.
4) Apply a Savitzky-Golay (SavGol) smoothing filter to the averaged reference pixel column.
5) Subtract the filtered reference column values from each column in the detector.

This method uses the reference pixels at the top and sides of the detector. It is applied to all detectors in the FPA, with an exception for SCA 3, 21946. The reference pixels on the right side of this detector (columns 4092:4096) are unstable and including them in the calculation introduces errors in the form of horizontal banding. So for SCA 3 only the left reference pixels (columns 0:4) are input into the SavGol filter.

Figure 9 shows an example of the pattern removed from SCA01 with reference pixel correction. The slope per pixel (ADU/second) was calculated for a dark exposure, with and without reference pixel correction. Then the corrected slope image was subtracted from the uncorrected slope image to show the structure of the pattern.

Figure 9: Pattern Removed During Reference Pixel Correction

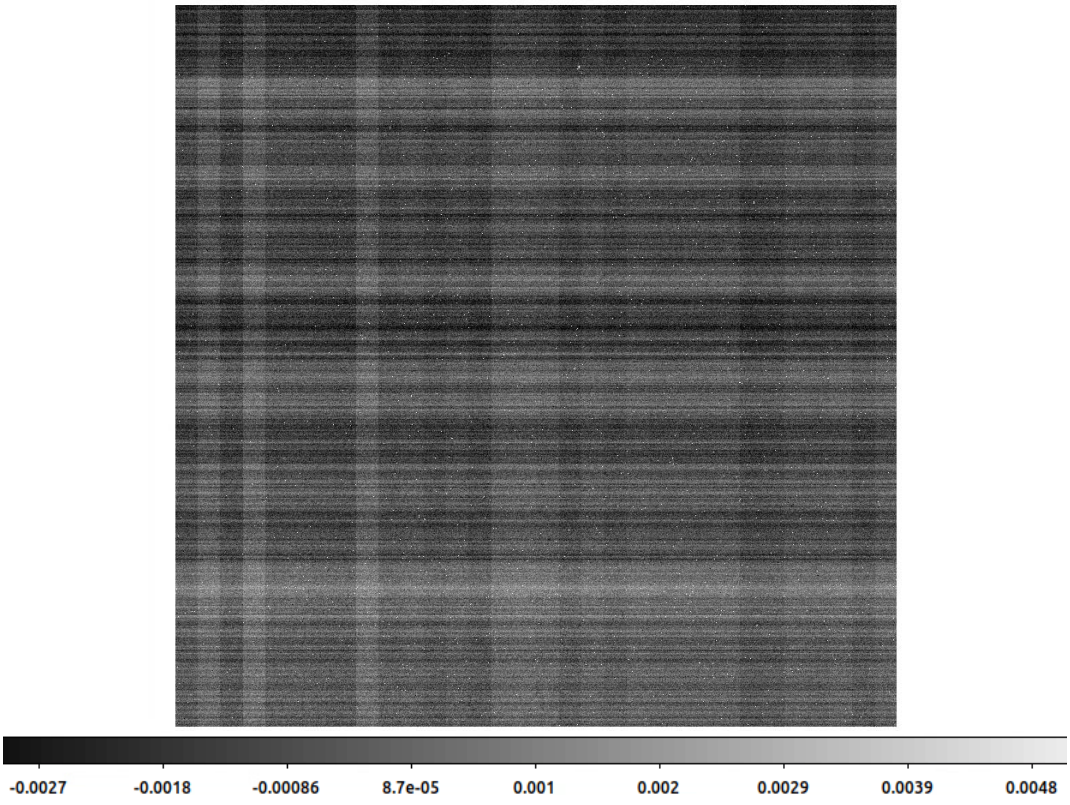

5 PHOTON TRANSFER GAIN

Photon transfer gain is applied to the detector data to convert from ADU to electrons, typically after reference pixel correction. Gain is calculated from the photon transfer curve using the mean-variance method on up-the-ramp flat field exposures. The data was collected during flight FPS TVAC and consisted of 10 exposures with 11 frames each (not including the reset-read frame) with a total signal accumulation of approximately 8000 ADU. The data analysis method is as follows:

1) Read in and apply reference pixel correction to an exposure.
2) Calculate the variance and average signal (in ADU) for each frame.
3) Calculate a linear fit using the average signal and variance.
4) The photon transfer gain in ADU/electrons is the slope of the linear fit.
5) Apply correction factor to account for IPC effects on the variance.

The IPC correction factor is based on a method described in *The Fe X-ray Energy Response of Mercury Cadmium Telluride Near-Infrared Detector Arrays* by Ori Fox:

$$\sigma_{\tilde{s}_4}^2 \approx \left(1 + 8\alpha + 52\alpha^2 + \dots\right) \sigma_{s_4}^2,$$

Where α is the fraction of signal crosstalk in nearest pixel neighbors (see Crosstalk section for more detail). Analysis of RST detector data used a first order approximation of the above equation. Photon transfer gain analysis of FPS and WFI data was performed on a per-channel basis, and the average of the 32 SCA output channels was used as a global gain value for most analyses.

Table 2: Photon Transfer Gain of the flight RST SCAs

SCA #	SN #	Gain (ADU/electrons)	Gain (electrons/ADU)
1	22081	0.505108	1.979774
2	21815	0.566483	1.765279
3	21946	0.570275	1.75354
4	21115	0.552151	1.811099
5	21816	0.571668	1.749267
6	20663	0.610992	1.636684
7	22069	0.518615	1.928214
8	21641	0.595606	1.678961
9	21813	0.599835	1.667124
10	22078	0.529413	1.888883
11	21947	0.549549	1.819675
12	20829	0.594061	1.68333
13	22067	0.542579	1.843048
14	21814	0.5636	1.774308
15	21645	0.552204	1.810925
16	21643	0.565962	1.766904
17	21319	0.664331	1.505273
18	20833	0.654402	1.528112

6 DARK CURRENT

6.1 Summary

Dark signal was measured at the DCL during acceptance/triplet testing, during FPS testing, and during both WFI TVAC campaigns. Results from the semiflight FPS test showed that several detectors had degraded dark current performance compared to their previous DCL tests, and the DD-ARB was convened to investigate the problem. Three detectors were replaced on the FPA per direction from the DD-ARB in locations 1, 4 and 12 on the MPA. The operating temperature of the detectors was also decreased from 95K to <90K following the recommendation of the DD-ARB, which has the effect of lowering the overall dark current in the detectors.

While all test campaigns have included a dark signal measurement, only the DCL results from acceptance testing are indicative of the true dark current of the detectors. This is because the background levels in subsequent test campaigns at the FPS and instrument level were well above the dark current floor of the SCAs. The Flight Acceptance Test dark current results are shown in a mosaic format below for comparison with the FPS and instrument-level tests, though these detectors were all tested separately at the DCL.

Figure 10: Dark Current during SCA Acceptance Testing

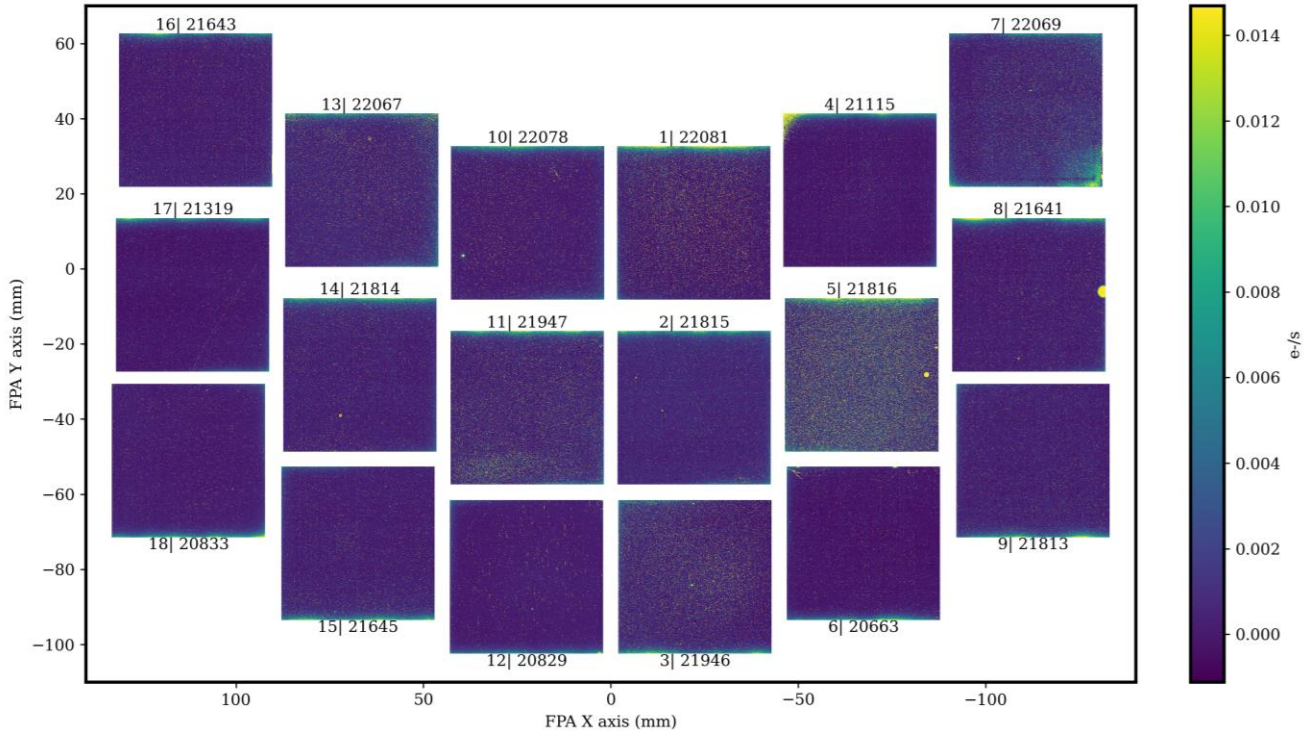

The following figures show mosaics of the dark signal measured during WFI TVAC2, TVAC1, and FPS TVAC. Cloudy areas with elevated signal can be attributed to instrument/test setup background due to pixel level variations in the long wavelength QE response across the SCAs. Sharper, linear features with elevated signal in SCAs like 20663, 21814, and 21319 are due to increased dark current in those areas.

Figure 11: Background during flight FPS TVAC (95 K)

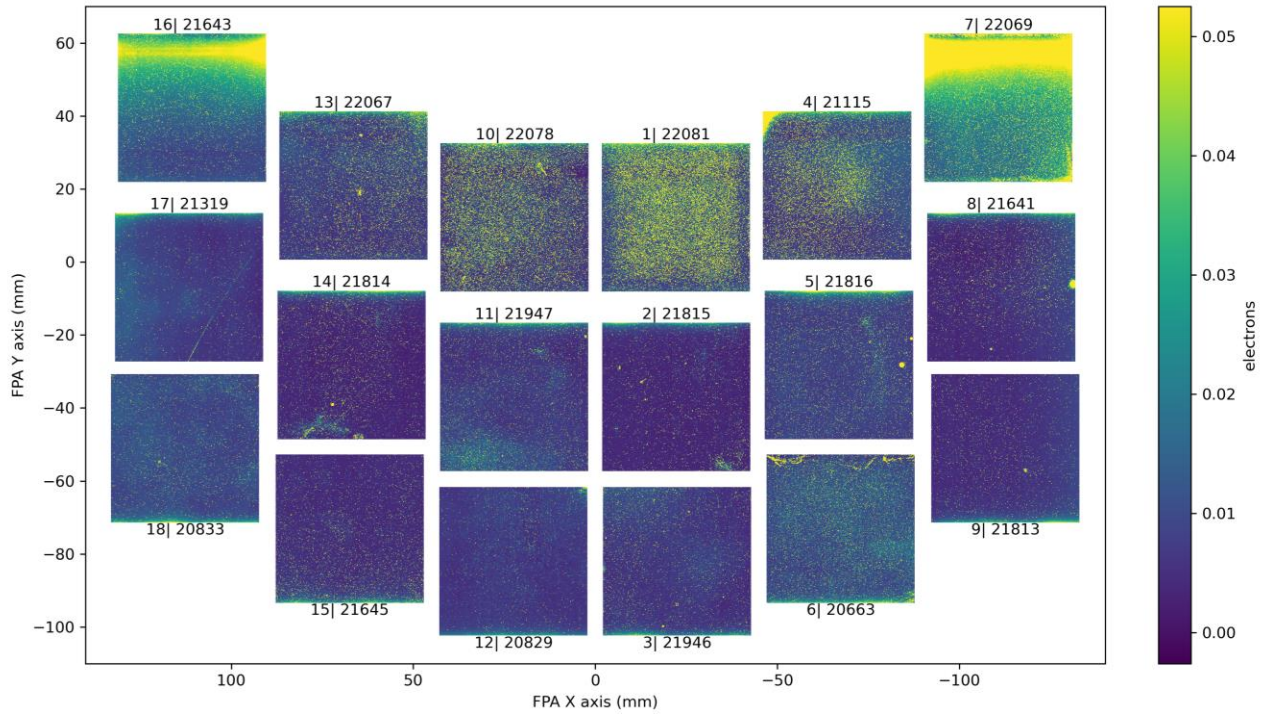

Figure 12: Background during WFI TVAC1 (89.8 K)

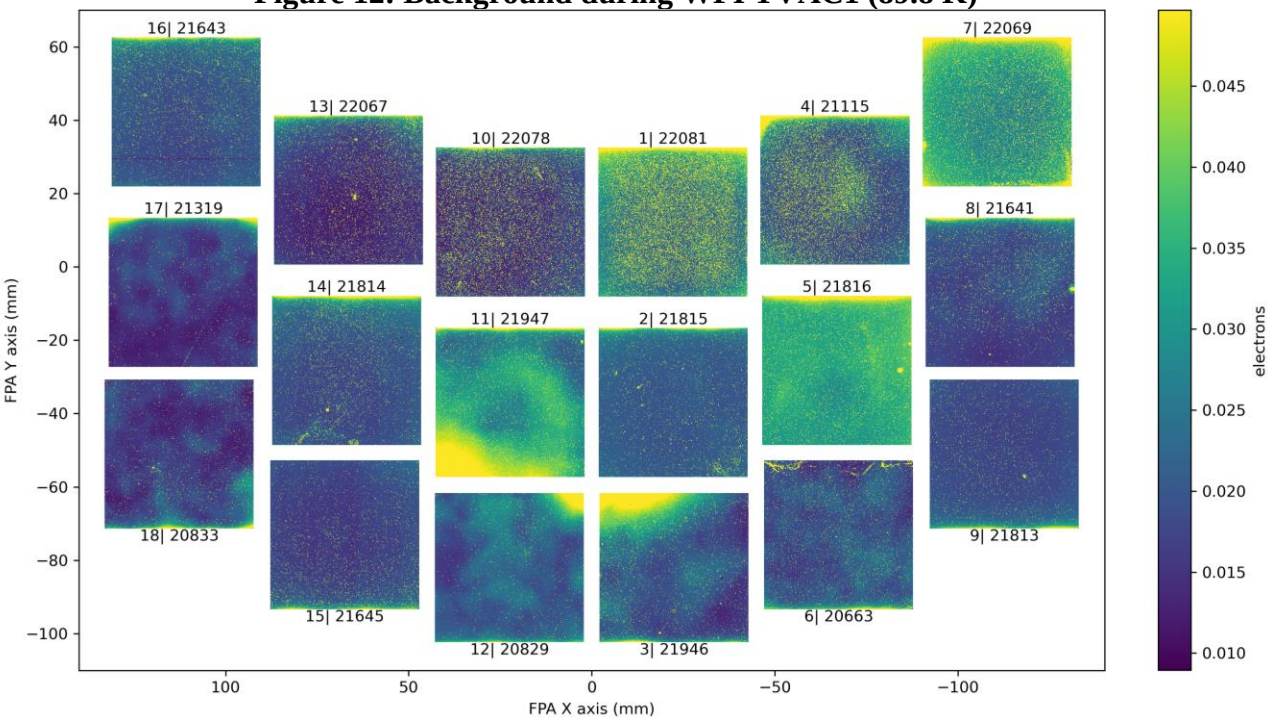

Figure 13: Background during WFI TVAC2 (89.5 K)

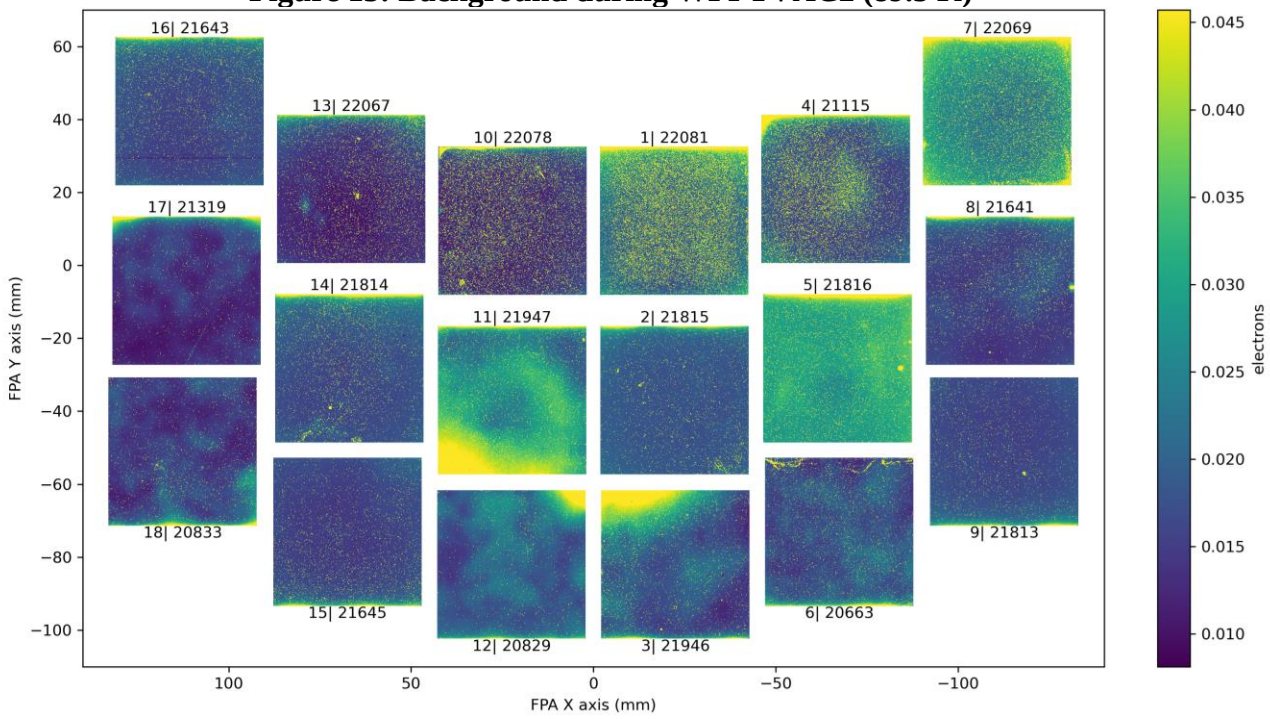

6.2 Dark Current Trending

The following plots show the trending mean and median dark current over the whole array of each SCA, as well as the percentage of pixels passing the requirement of dark current <0.05 e-/s. More information on dark current trending is on TDMS under RST-WFI-TN-0621.

Figure 14: Median SCA Dark Current Trending

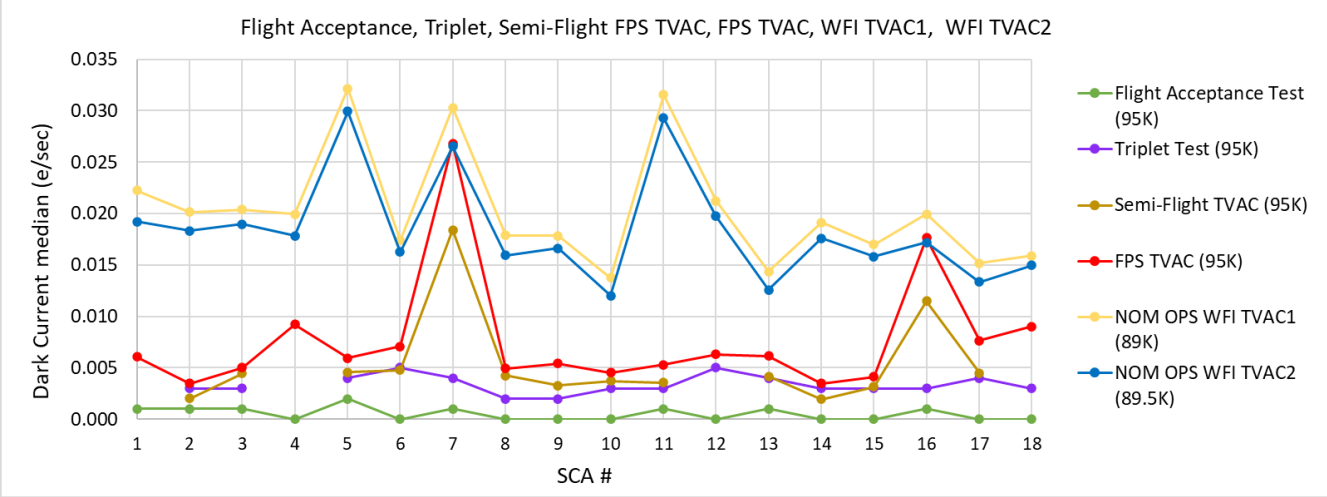

Figure 15: Mean SCA Dark Current Trending

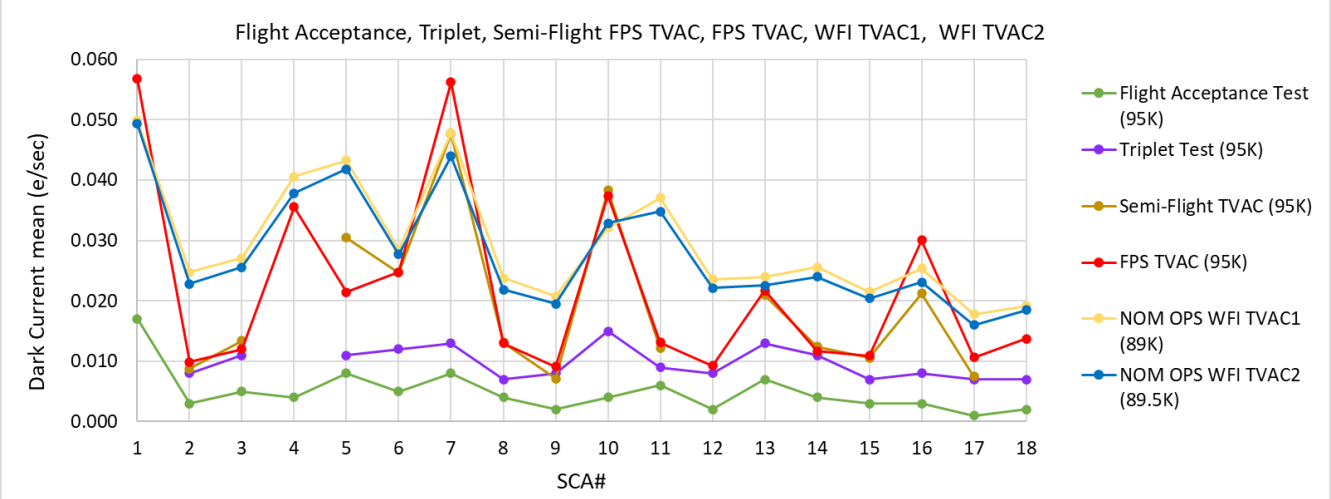

Figure 16: Percent Pixels Passing Dark Current Trending

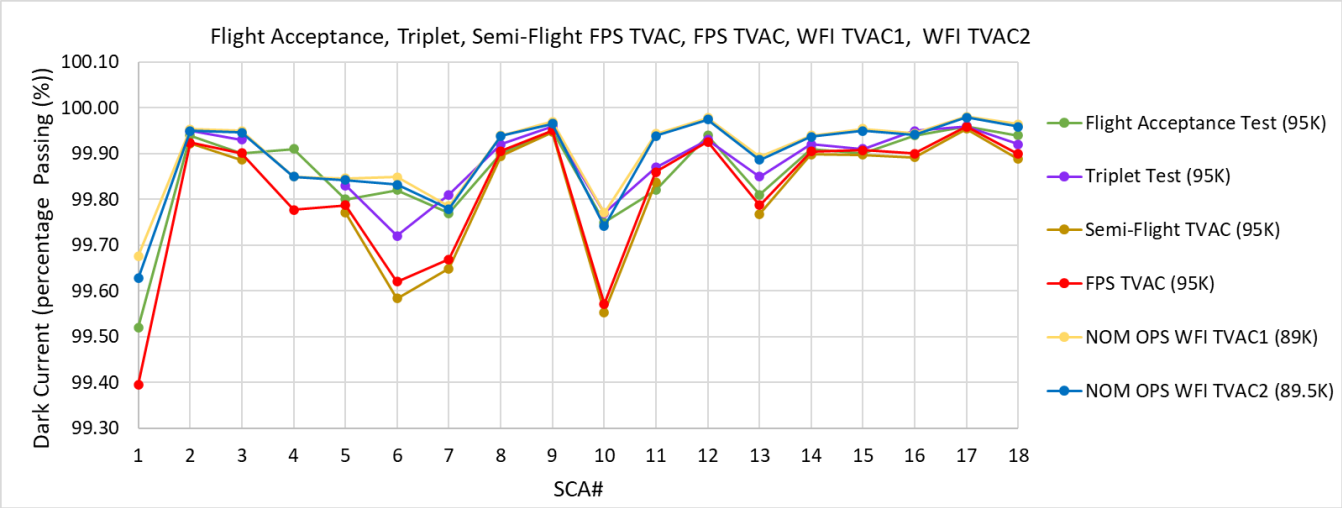

6.3 Crosshatching

Crosshatched patterns that correspond to small scale (subpixel) QE fluctuations have been observed in HgCdTe detectors (e.g *Euclid H2RG Detectors: Impact of crosshatch patterns on photometric and centroid errors*, Crouzet et al. 2018). Crosshatching has also been observed in some of the H4RG detectors manufactured for RST. Crosshatching is thought to originate in morphological variations of the HgCdTe surface along the 3 crystal axes, and the appearance of these features is also thought to be related to growth conditions (see *Characterization of cross-hatch morphology of MBE (211) HgCdTe*, Martinka et al. 2001). The presence of these small-scale QE changes can pose a photometric and shape measurement challenge as described in *Intra-pixel Response Characterization of a HgCdTe Near Infrared Detector with a Pronounced Crosshatch Pattern*, Shapiro et al. 2018.

Crosshatching is visible in some form in all flight detectors. It appears differently in illuminated images vs. dark images. In dark current images it looks like crosshatched lines of high signal, typically in small patches around the active area of the SCA. For illuminated images it looks like

parallel lines of low signal, or X-shaped lines centered about a small group of low signal pixels. Crosshatching in illuminated images covers large areas of the SCA.

Figure 17: Example of dark current crosshatching in SCA06.
Location: [5:282, 70:232]

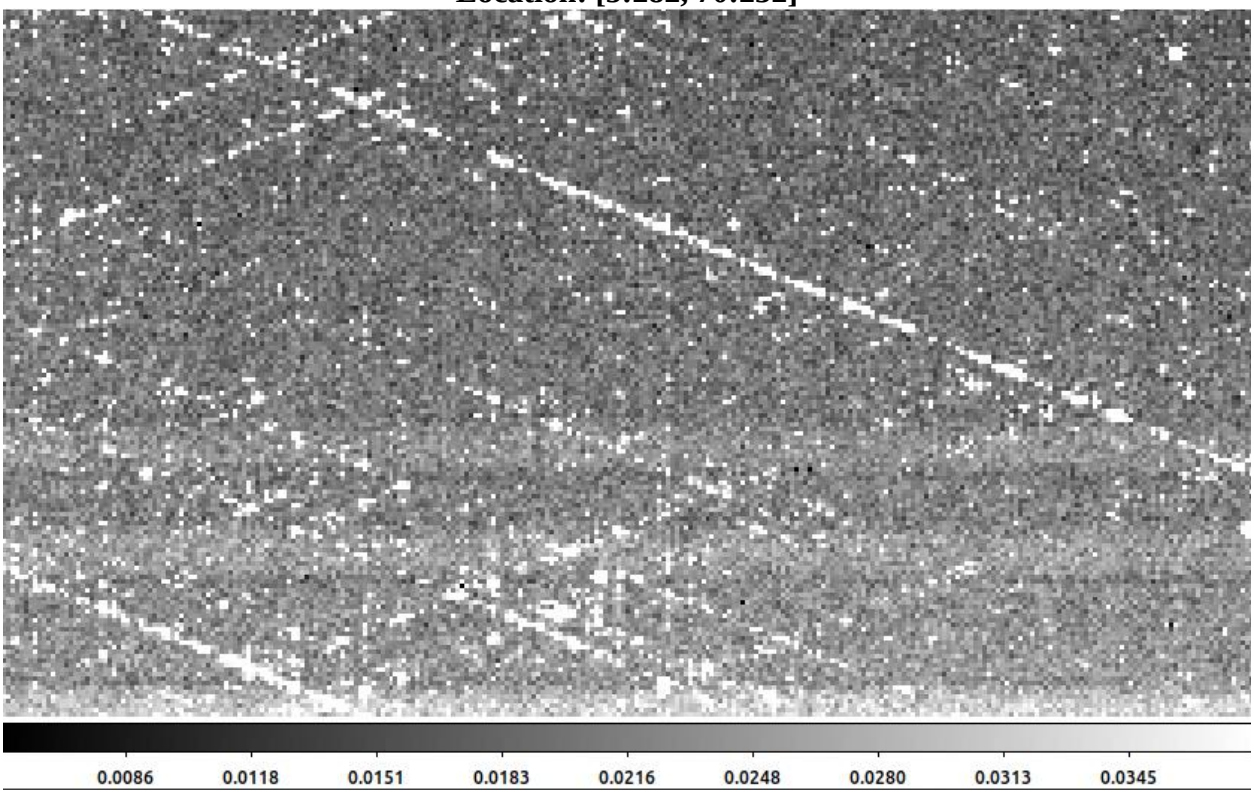

Figure 18: Example of illuminated parallel and X shaped crosshatching in SCA01. Location: [2669:3406, 3108:3524]

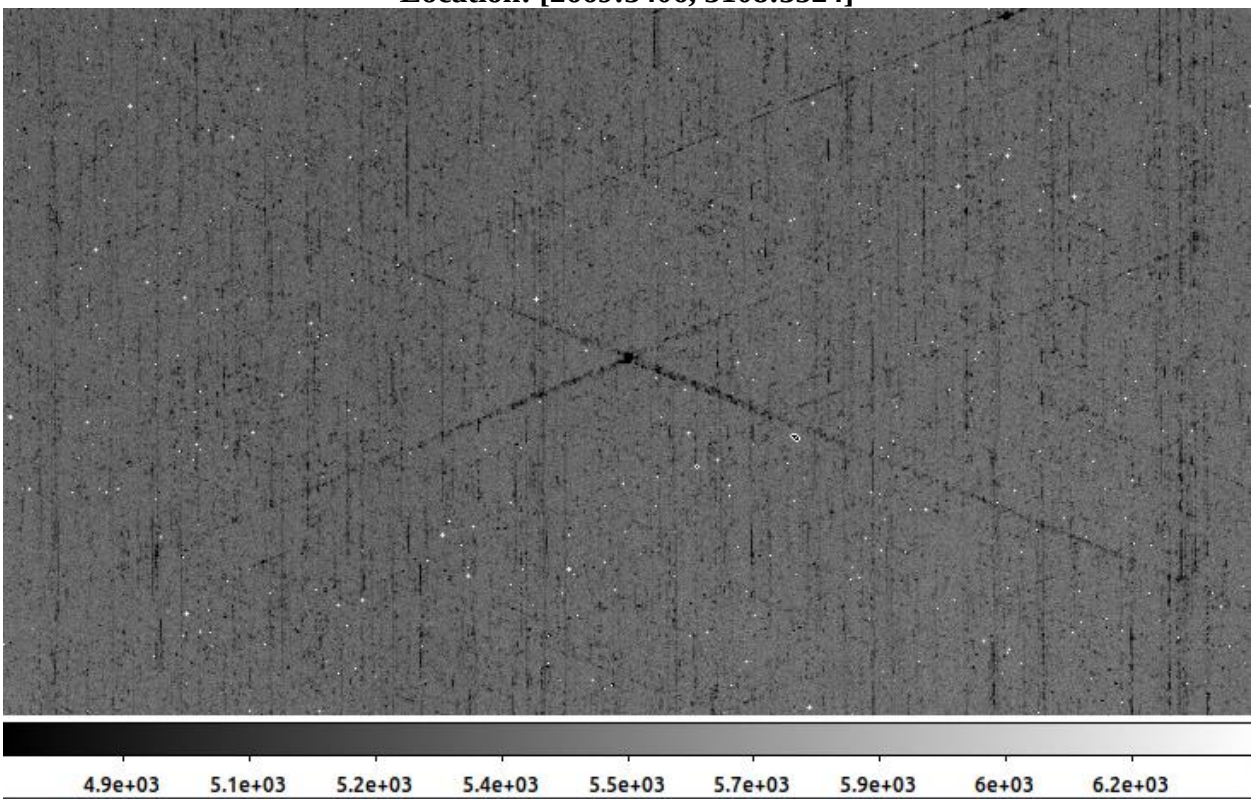

Areas with crosshatching in the dark current are usually not visible in illuminated images. The figure below shows examples of crosshatching in 800pxs x 600pxs subregions of dark images (left column) and flat field images (right column) acquired during the WFI-TVAC2 test for detectors in locations 4, 6, 12, and 14. For those regions, the crosshatching is more evident in dark images.

Figure 19: Left column: Dark Current images. Right column: Flat Field images. Crosshatching in the subsector indicated on the image's subtitles for SCU4, SCU6, SCU12, SCU14.

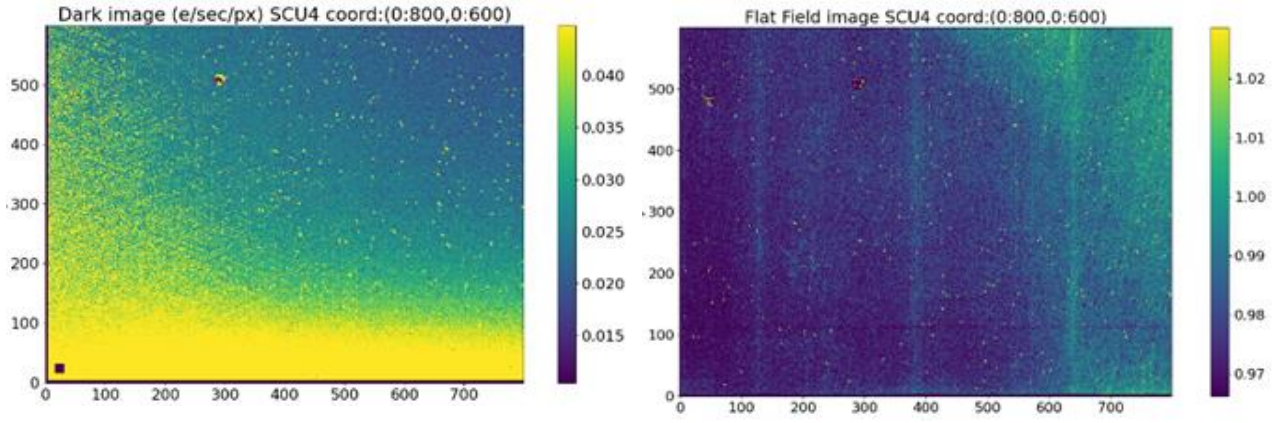

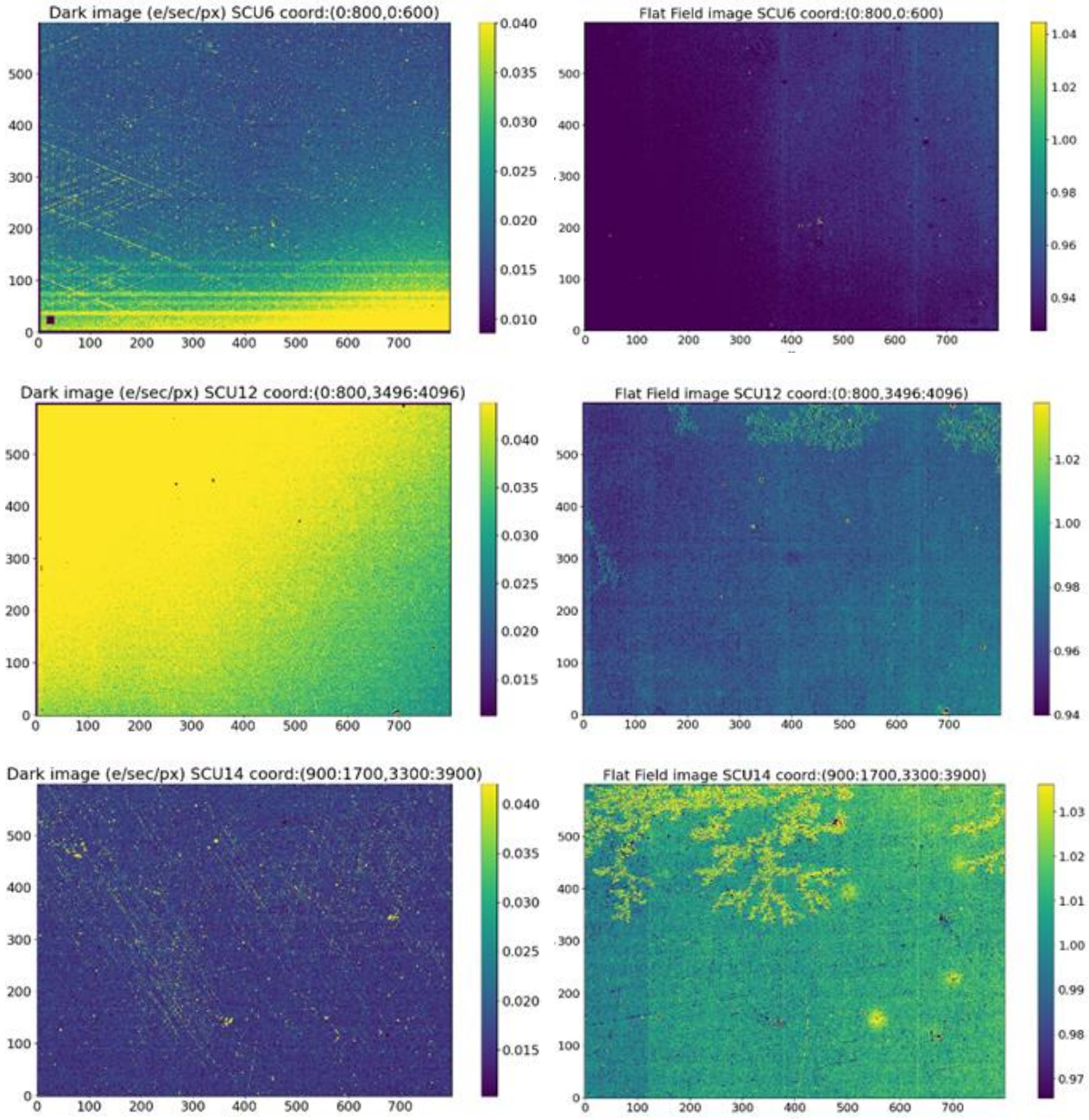

The table below shows dark current statistics for WFI-TVAC2 data in the subregions presented in Figure 19 compared to the statistics of the entire array for the same detectors.

Table 4: Dark current statistics for WFI-TVAC2 data for the entire array and for subregions

SCU #	Median entire array	Mean entire array	% Pass Req entire	Median sector	Mean sector	% Pass Req sector
4	0.018	0.038	99.85	0.029	0.064	99.25
6	0.016	0.028	99.83	0.020	0.027	99.60

12	0.020	0.022	99.97	0.044	0.047	99.63
14	0.018	0.024	99.94	0.016	0.027	99.57

Figure 20 Figure 20 below presents examples in SCU8, SCU9, and SCU11 detectors where the crosshatching is evident in the illuminated images (right) but not in the dark images (left).

Figure 20: Left column: Dark Current images. Right column: Flat Field images. Crosshatching in the subsector indicated in the image's subtitles for SCU8, SCU9, SCU11. The dark current data was acquired during WFI-TVAC2.

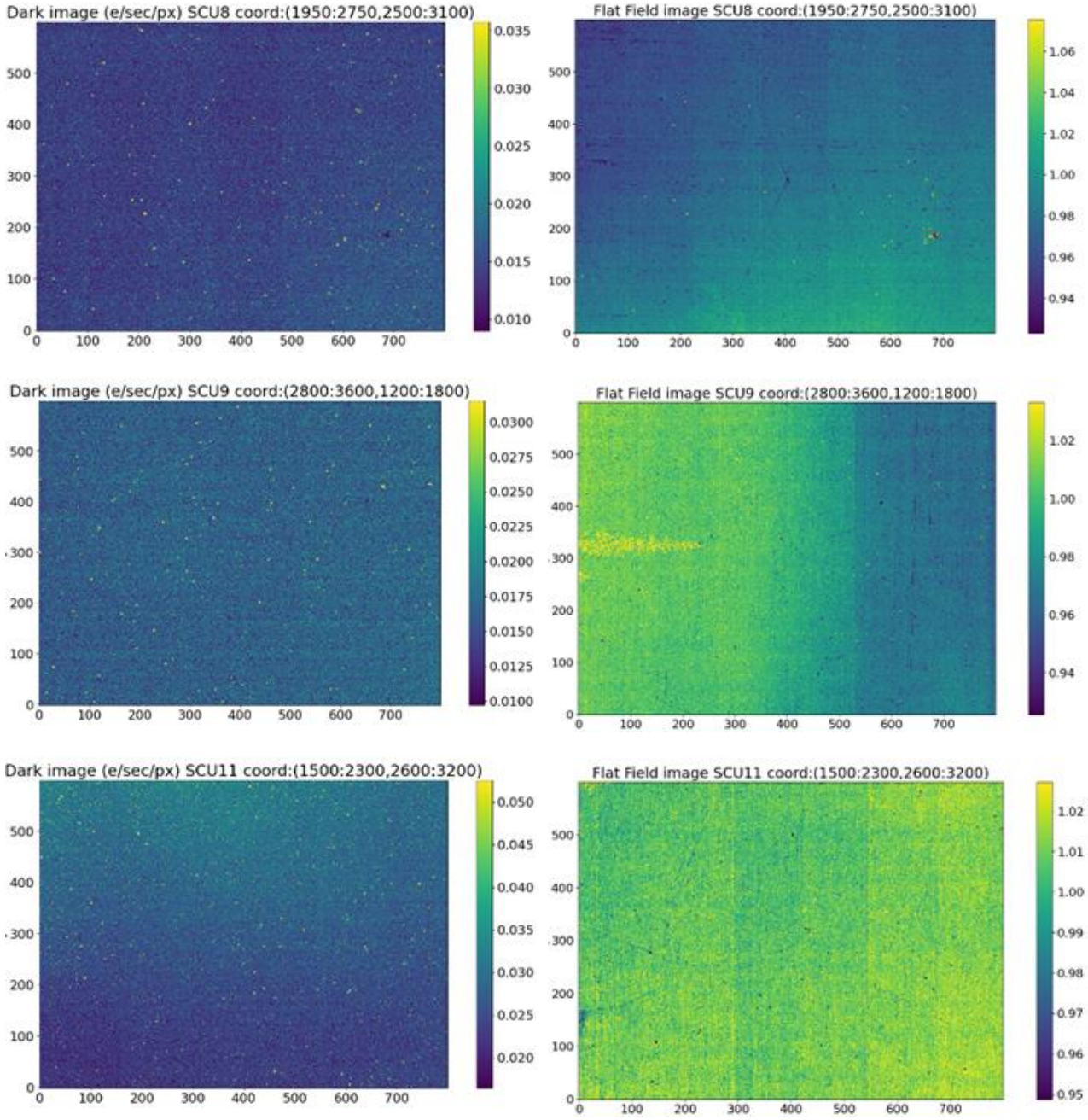

Table 5 shows dark current statistics for WFI-TVAC2 data in the subregions presented in Figure 20 compared to the statistics of the entire array for the same detectors.

Table 5: Dark current statistics for WFI-TVAC2 data for the entire array and for subregions

SCU #	Median entire array	Mean entire array	% Pass Req entire	Median sector	Mean sector	% Pass Req sector
8	0.016	0.022	99.94	0.015	0.019	99.67
9	0.017	0.019	99.97	0.017	0.019	99.68
11	0.029	0.035	99.94	0.027	0.030	99.67

The effects of crosshatching are more visible at higher operating temperature and bias voltage. During the Flight Acceptance Test some detectors were tested at different temperatures and bias voltages. Figure 21 and Figure 22 show the dark current for SCA 6 and SCA 12, respectively, at 90K and 95K and at bias voltages of 0.5V and 1.0V. For each detector the same region is plotted with different temperatures and voltages, showing that the crosshatching is more evident at higher temperatures and voltages.

Figure 21: Dark Current images acquired during the Flight Acceptance Test for SCA 6 at temperature and bias voltages indicated on the subtitles of each figure.

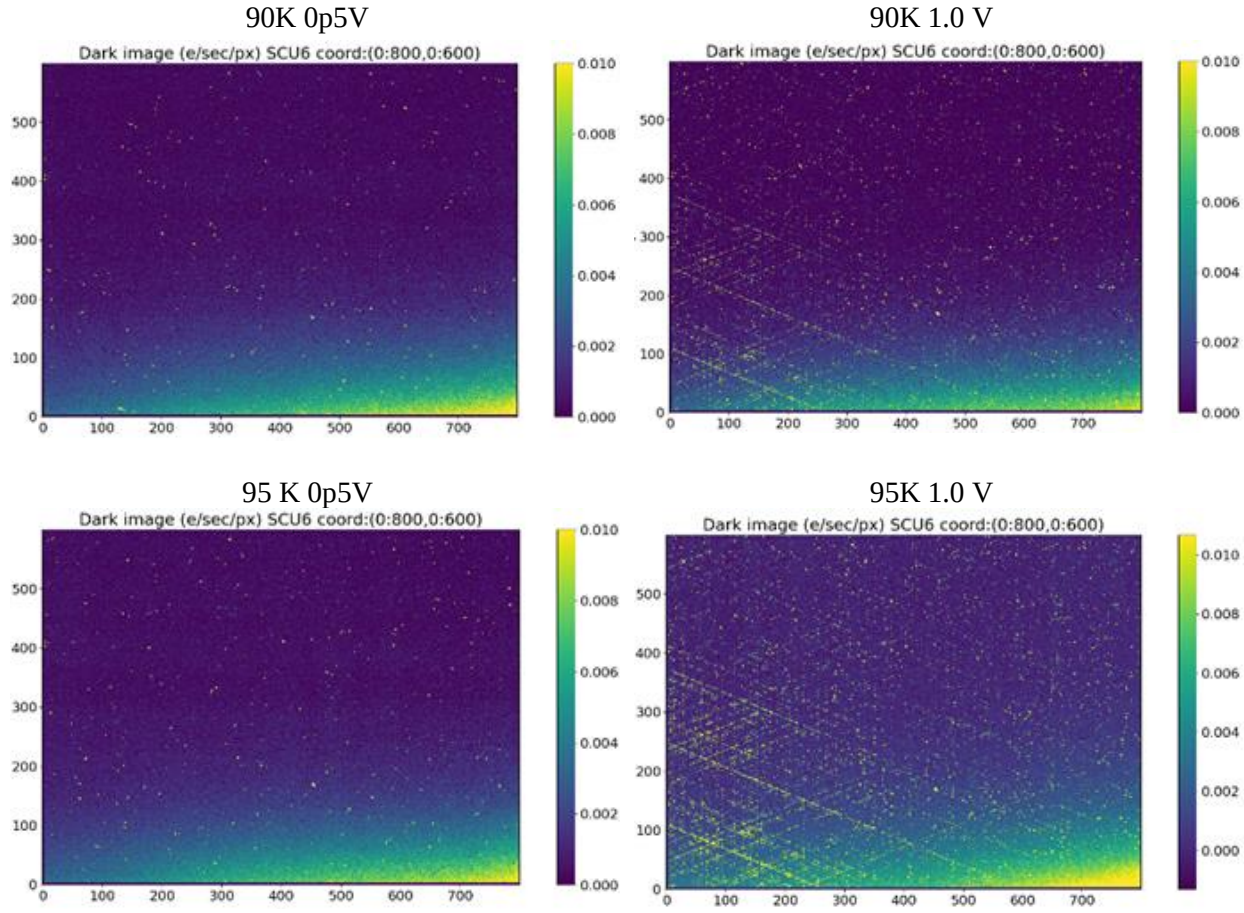

Figure 22: Dark Current images acquired during the Flight Acceptance Test for SCA 12 at temperature and bias voltages indicated on the subtitles of each figure.

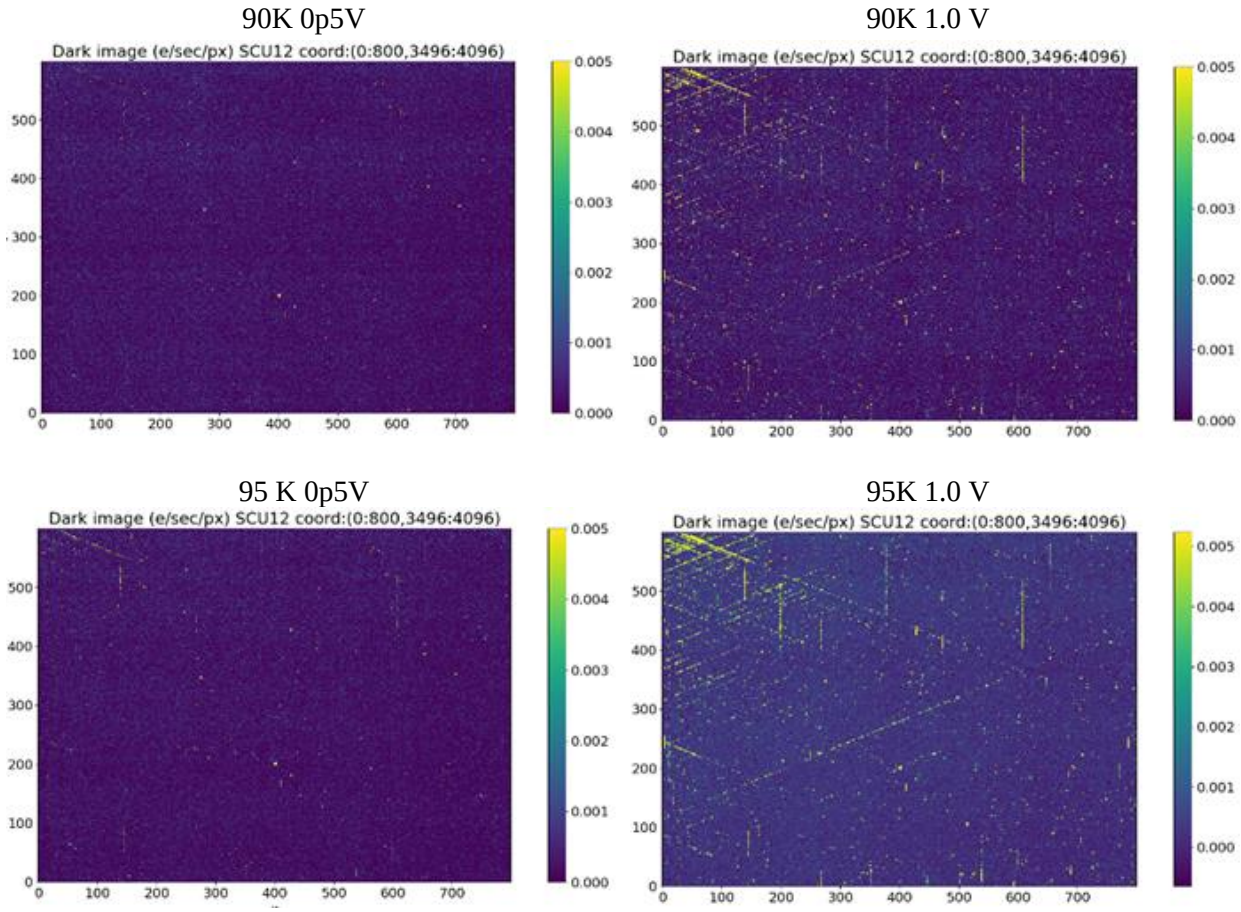

The regions where crosshatching appears in dark images are associated with faster dark current degradation. Figure 23 shows the relative normalized difference between WFI-TVAC2 and WFI-TVAC1 (dark current WFI TVAC2 / median (dark current WFI TVAC2) - dark current TVAC1/ median (dark current WFI TVAC1)) in the same detectors and subregions shown above. The crosshatching lines were more notable during WFI-TVAC2 (89.5K) compared to WFI-TVAC1 (89K); the SCA temperature was almost the same in both tests.

Figure 23: Normalized difference of dark current images for SCU4, SCU6, SCU12, SCU14 between WFI-TVAC2 and WFI-TVAC1

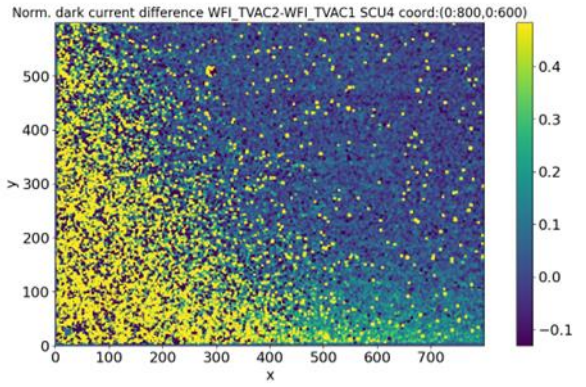

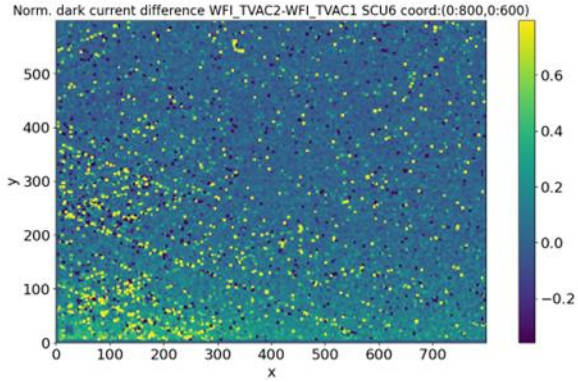

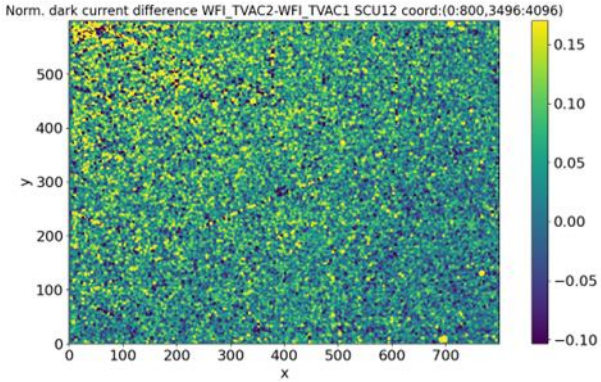

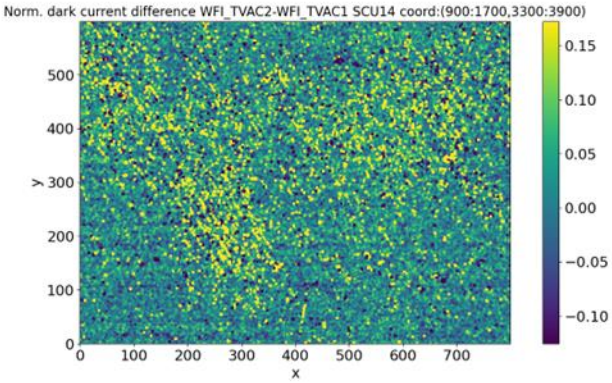

Table 6 shows the dark current statistics during FPS TVAC, WFI TVAC1, and WFITVAC2 for the entire array (top panel) and for the same crosshatching subregions shown in Figure 23 (bottom panel) for SCU4, SCU6, SCU12, and SCU14. During those last three tests, the SCA temperature was between 88K and 89.5 K. There may have been some degradation in these areas indicated by higher dark current in WFI TVAC1 and WFI TVAC2 even though the SCA temperatures were similar throughout each test campaign. One caveat is that instrument background levels were high in WFI TVAC1 and WFI TVAC2 compared to Flight FPS TVAC, which would also influence the dark current statistics.

Table 6: Dark current statistics for the entire array (top) and subregions (bottom) of detectors SCU4, SCU6, SCU12, and SCU14. Data acquired during FPS-TVAC, WFI-TVAC1, and WFI-TVAC2.

Entire array

SCU#	Median FPS	Mean FPS	% Passing FPS	Median WFI-TVAC1	Mean WFI-TVAC1	% Passing WFI-TVAC1	Median WFI-TVAC2	Mean WFI-TVAC2	% Passing WFI-TVAC2
4	0.003	0.023	99.85	0.020	0.041	99.85	0.018	0.038	99.85
6	0.001	0.011	99.87	0.017	0.028	99.85	0.016	0.028	99.83
12	0.003	0.004	99.98	0.021	0.024	99.98	0.020	0.022	99.97
14	0.001	0.007	99.94	0.019	0.026	99.94	0.018	0.024	99.94

Subregions

SCU#	Median FPS	Mean FPS	% Passing FPS	Median WFI-TVAC1	Mean WFI-TVAC1	% Passing WFI-TVAC1	Median WFI-TVAC2	Mean WFI-TVAC2	% Passing WFI-TVAC2
4	0.007	0.040	99.39	0.032	0.065	99.32	0.029	0.064	99.25
6	0.004	0.009	99.64	0.021	0.027	99.63	0.020	0.027	99.60
12	0.003	0.005	99.66	0.046	0.049	99.64	0.044	0.047	99.63
14	0.001	0.011	99.60	0.017	0.028	99.59	0.016	0.027	99.57

The spatial structure of crosshatching along with its different behavior and locations in illuminated and dark images make it difficult to isolate pixels that are affected by it, and so crosshatched pixels are currently not included in the binary operability masks (see Section 17). Crosshatching in illuminated images covers most of the surface of the SCAs, but the crosshatching in dark images is more isolated and discrete regions can be identified. The following table and mosaic image shows approximate coordinates [columns, rows] of crosshatched pixels in dark images.

Table 7: Coordinates of crosshatched regions for dark images

SCA#	16	13	10	1	4	7
Coordinates	-	-	-	-	[0:330, 0:870]	-
SCA#	17	14	11	2	5	8
Coordinates	-	[425:2025, 3341:4092] [2517:3504, 176:1239] [3095:3396, 3205:3790]	[2505:2900, 682:884]	[2046:3555, 500:1720] [3041:3696, 3738:4057]	[2582:2937, 713:973]	-
SCA#	18	15	12	3	6	9
Coordinates	-	-	[0:700, 3500:4092]	-	[0:630, 0:776]	-

Figure 24: Dark current crosshatching locations.

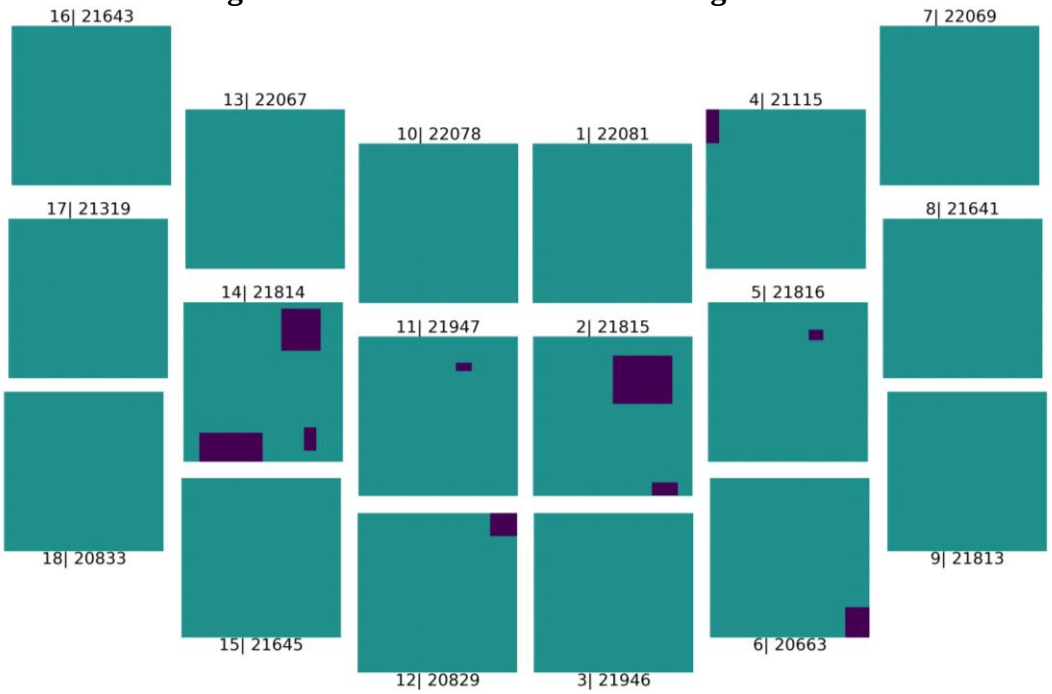

6.4 Blinkers

Blinkers are pixels that appear to change their dark current, between discrete levels, from one set of exposures to the next. This may cause these pixels to be flagged as failing the Roman total noise requirements and complicate standard pipeline analysis, as it is typically assumed dark current is constant. The precise physical origin of blinkers is not understood, but it may involve the presence of multiple defect states in blinking pixels and/or the presence of impurities to selectively activate or deactivate a defect state in the blinking pixel. Blinkers have been observed in other HgCdTe detectors, so they are not unique to Roman.

Figure 25 shows an archetypical blinker pixel in SCA 22077. This is one of 3 SCAs that were replaced due to degradation. The left panel plots the pixel's dark current as a function of exposure number in a standard sequence of FPS dark exposures. Dark current toggles between 1.5 e^-/s (failing requirements) and $\lesssim$ 0.5 e^-/s (barely meeting requirements). The right panel shows that the up-the-ramp samples are still well-modeled by straight lines. This is a particularly simple example. Most blinker pixels have more than two stable states. Blinkers can "blink" at any time, which creates kinks in the right-hand plot.

Figure 25: Blinker behavior for a single pixel in SCA 22077

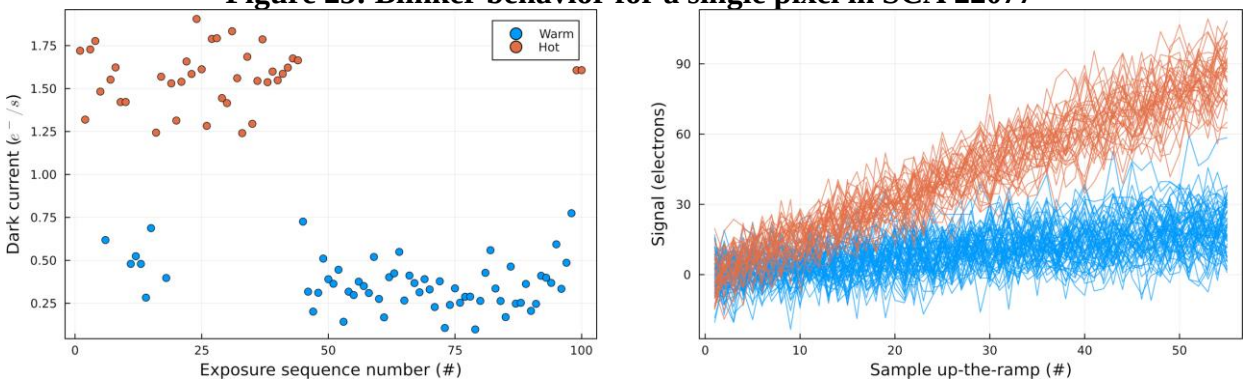

Table 8. Blinkers in Flight FPS

	Blinker percentage[1]	
SCU	T = 95 K	T = 85 K
1	0.50%	0.25%
2	0.16%	0.09%
3	0.24%	0.12%
4	0.22%	0.09%
5	0.22%	0.10%
6	0.19%	0.10%
7	0.24%	0.15%
8	0.14%	0.10%
9	0.13%	0.08%
10	0.40%	0.25%
11	0.20%	0.10%
12	0.15%	0.07%
13	0.36%	0.19%
14	0.18%	0.09%
15	0.17%	0.10%
16	0.19%	0.11%
17	0.17%	0.09%
18	0.15%	0.07%

[1]Many would already fail the WFI's $\sigma_{total} < 12\ e^-$ requirement.

Blinkers were observed in the Dark Degradation Anomaly Review Board investigation to also concentrate in regions where the dark current performance had degraded (i.e., near crosshatch and hot pixels). DD-ARB investigations found that blinkers could account for an additional 0.1-0.2% of dark current operability degradation. The percentage of blinkers in the focal plane is small and was found to decrease with operating temperature.

7 NOISE

7.1 Total Noise

Total noise was measured and tracked throughout the DCL, FPS, and WFI level tests. It is measured by collecting a large data set of 100 exposures with 55 read frames each. At the WFI level this dataset is split into two activities to accommodate for the guide window which is reset multiple times per exposure. For 50 exposures the guide window is placed in the bottom left corner, and for the other 50 exposures it is in the top right corner. These data are analyzed by calculating a linear fit per pixel for each exposure, and the standard deviation of the slopes multiplied by the exposure time is reported as the total noise.

Figure 26: Total noise in WFI TVAC1 (89 K)

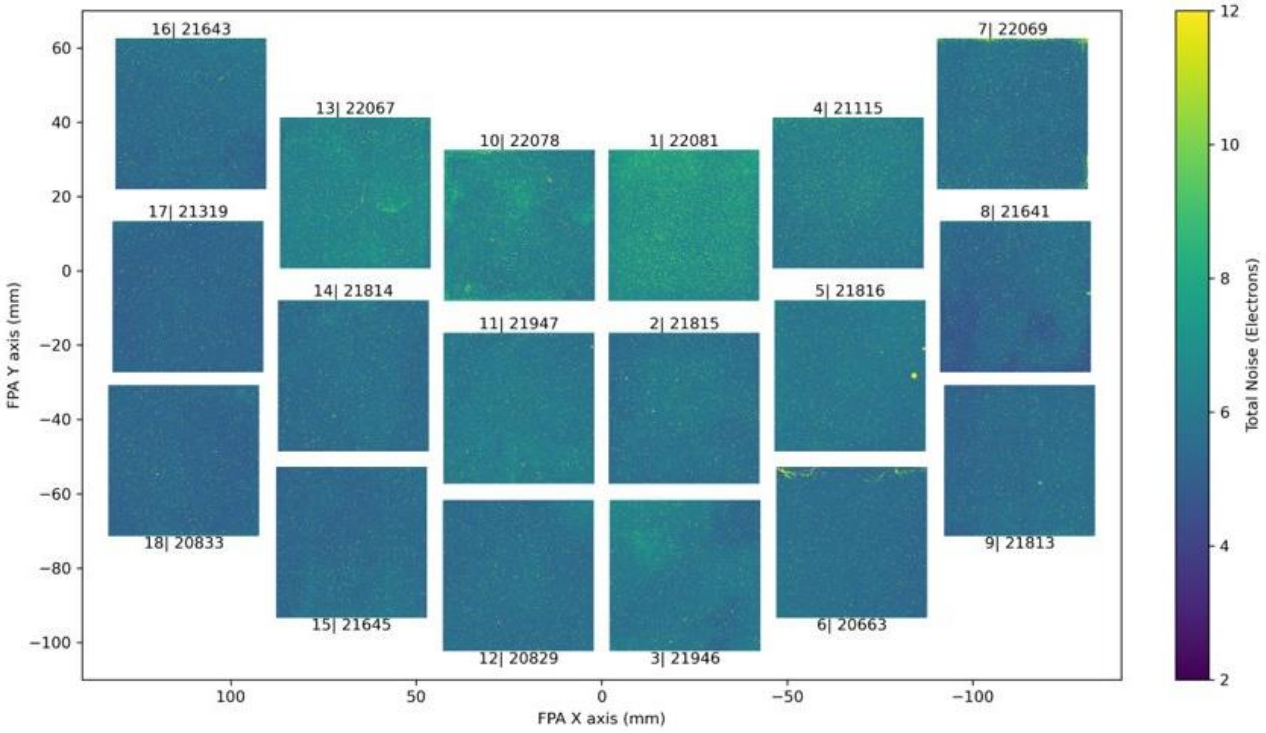

Figure 27: Total noise in WFI TVAC2 (89.5 K)

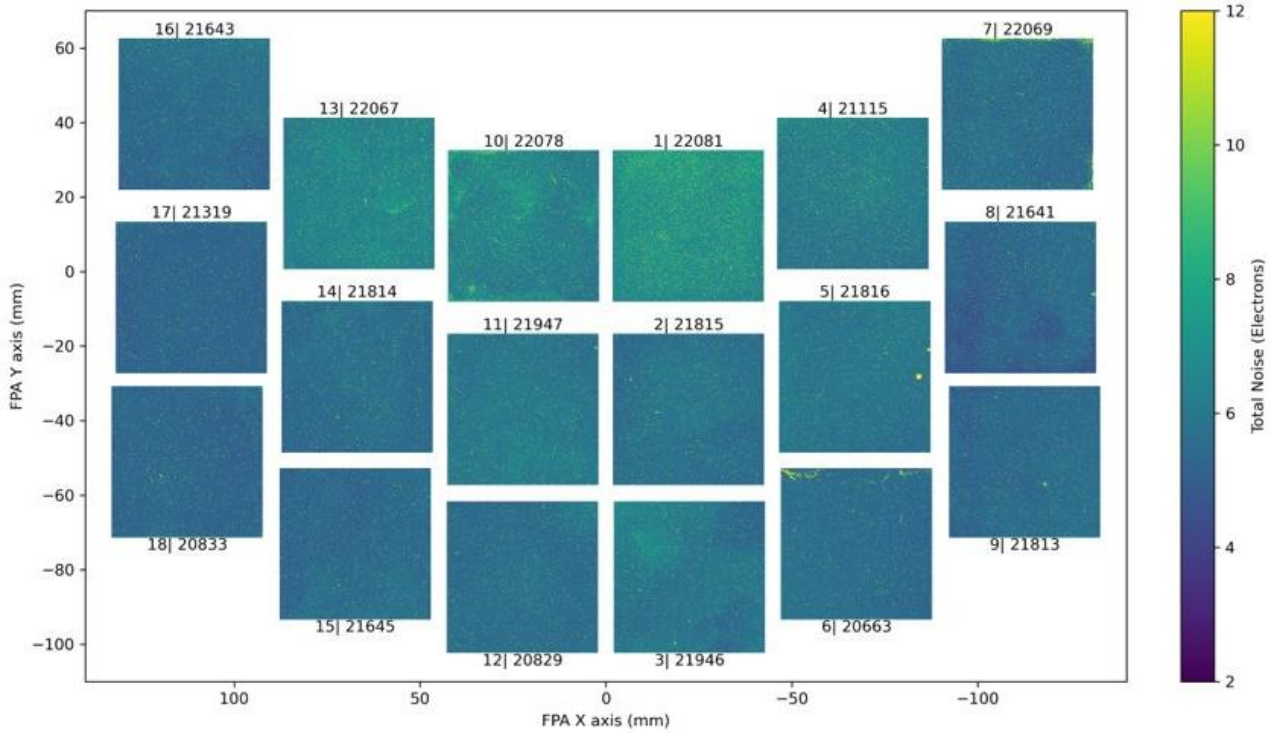

The following plots show the trending mean and median total noise over the whole array of each SCA, as well as the percentage of pixels passing the requirement of total noise <6.5 e-/exposure. More information on total noise trending is on TDMS under RST-WFI-TN-0619.

Figure 28: Median SCA Total Noise Trending

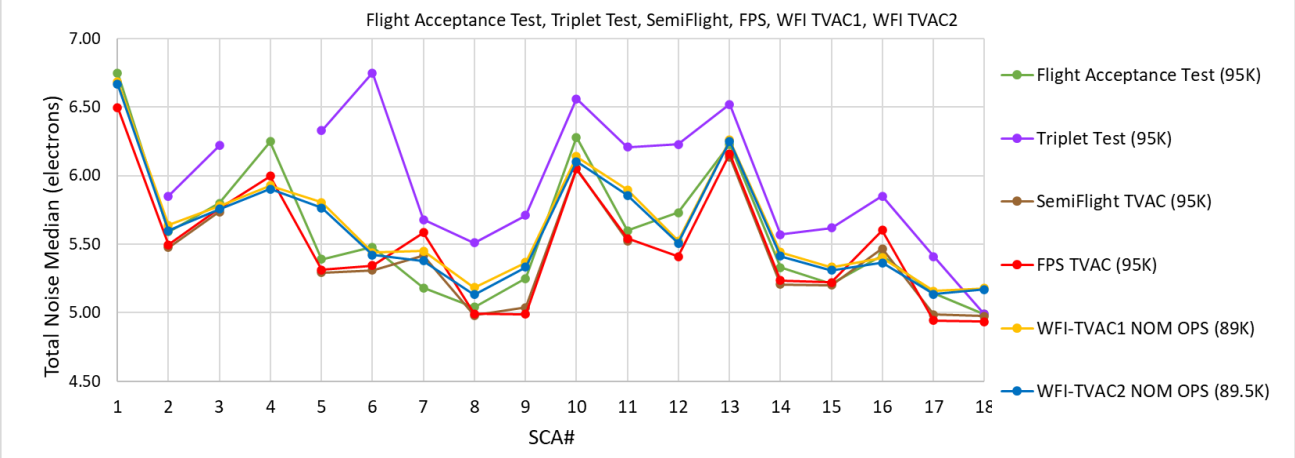

Figure 29: Mean SCA Total Noise Trending

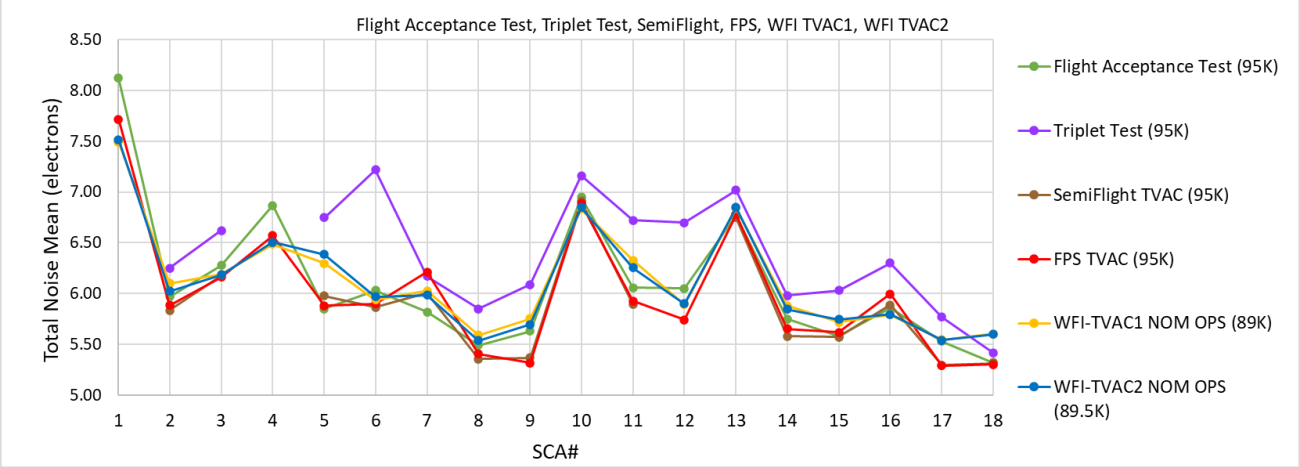

Figure 30: Percent Pixels Passing Total Noise Trending

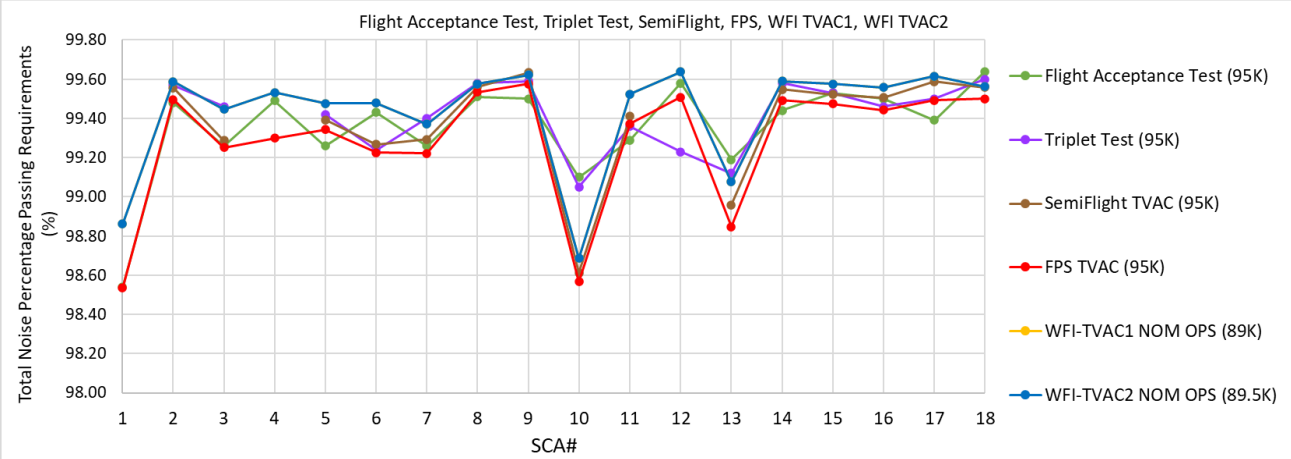

7.2 Transient noise in SCA channels

During the WFI TVAC tests there were several occurrences of transient high noise behavior within certain SCA output channels. This noise manifested as a pattern of alternating high and low value columns in the slope per pixel for an exposure; and it would happen intermittently for random exposures. The reference pixels within the affected columns do not behave abnormally when the noise appears, and the pixel values in individual frames for affected exposures do not show any outliers. This behavior was first seen in output channel 6 of SCA 8 and output channels 1 and 26 of SCA 17 during the NomOps plateau in TVAC1. It appeared again in output channel 10 of SCA 17 and output channel 10 of SCA 8 during ColdQual in TVAC2, and in output channel 29 of SCA 14 in NomOps in TVAC2. It was documented in PR-RST-WFI-4159-146 during WFI TVAC1 and remains unexplained. The PR was closed and added to the known issues list for WFI TVAC2.

Figure 31: Example of transient output channel noise in SCA 17 (left) and detail (right

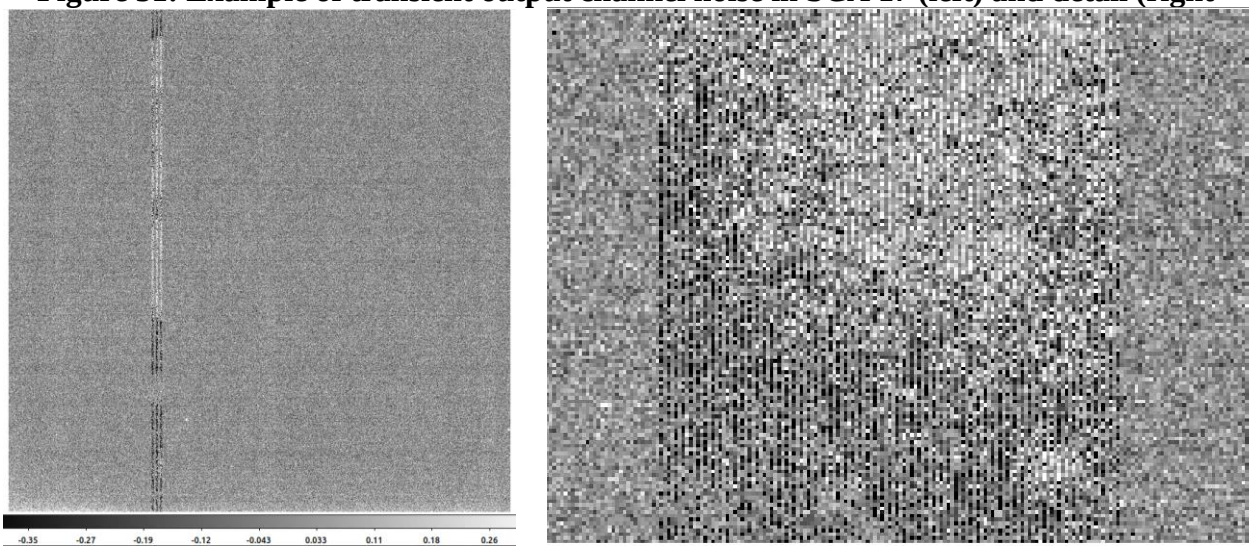

Figure 32: Transient noise in consecutive exposures for SCA 8 Channel 10

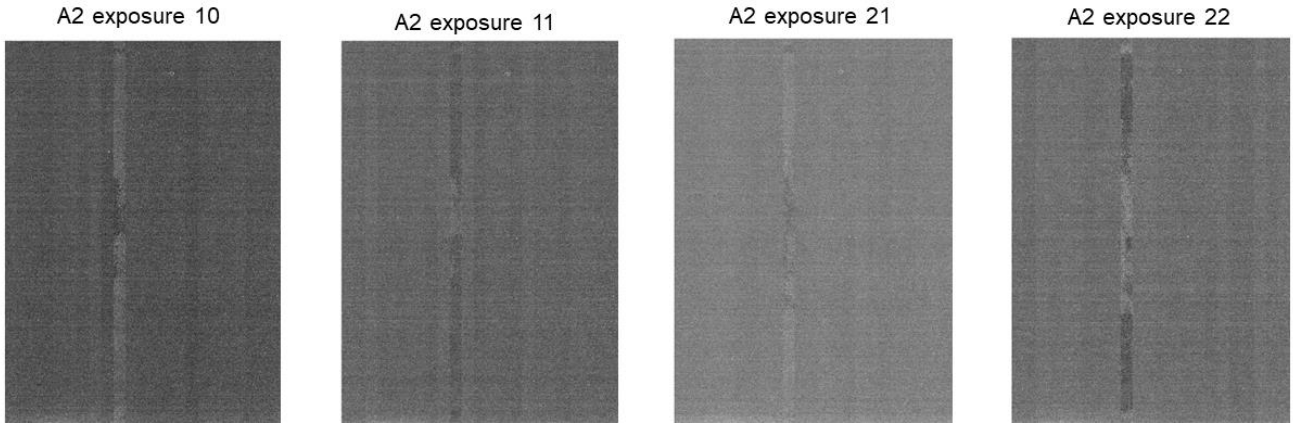

7.3 CDS Noise

While there is no formal requirement for Correlated Double Sampling (CDS) noise, it was measured and tracked throughout DCL acceptance testing, FPS, and WFI level tests. At the DCL CDS noise was a dedicated dataset of five exposures with 100 frames each, but for the FPS and WFI tests the Total Noise dataset was used. Analysis is performed by taking the difference between non-overlapping pairs of consecutive reference pixel corrected frames and calculating the standard deviation per pixel, then applying the gain conversion from ADU to electrons.

Figure 33: CDS Noise in WFI TVAC1

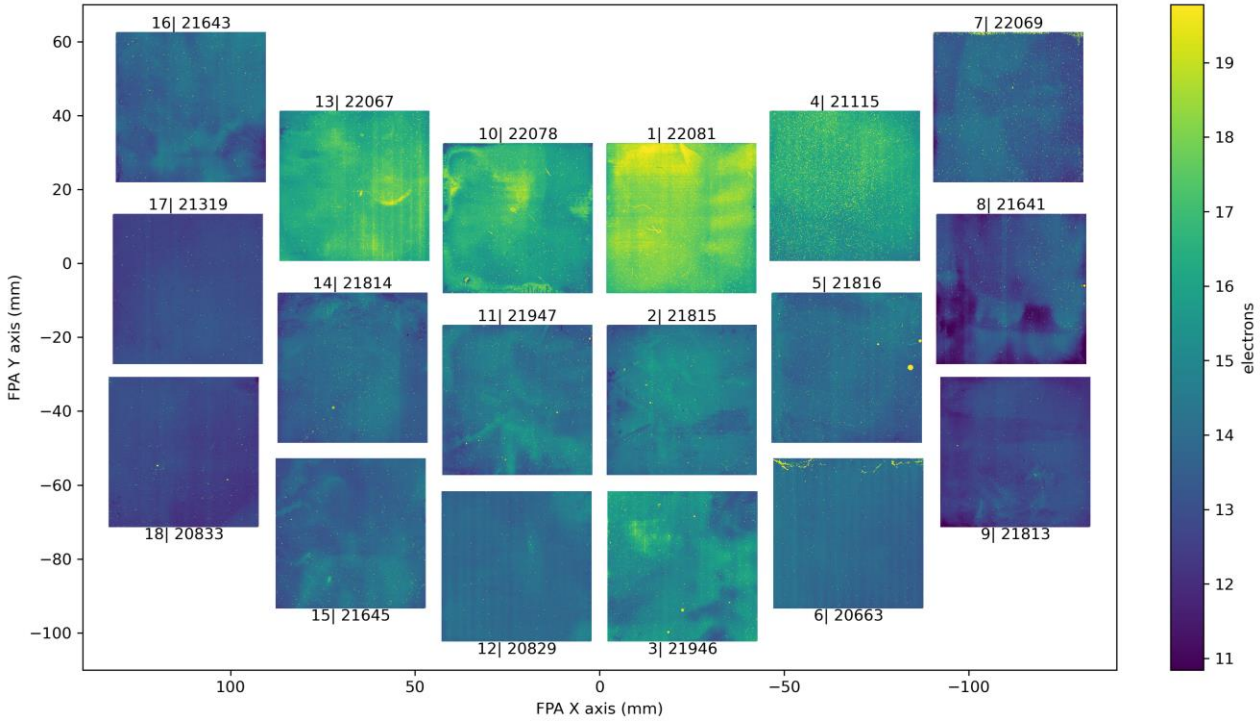

Figure 34: CDS Noise in WFI TVAC2

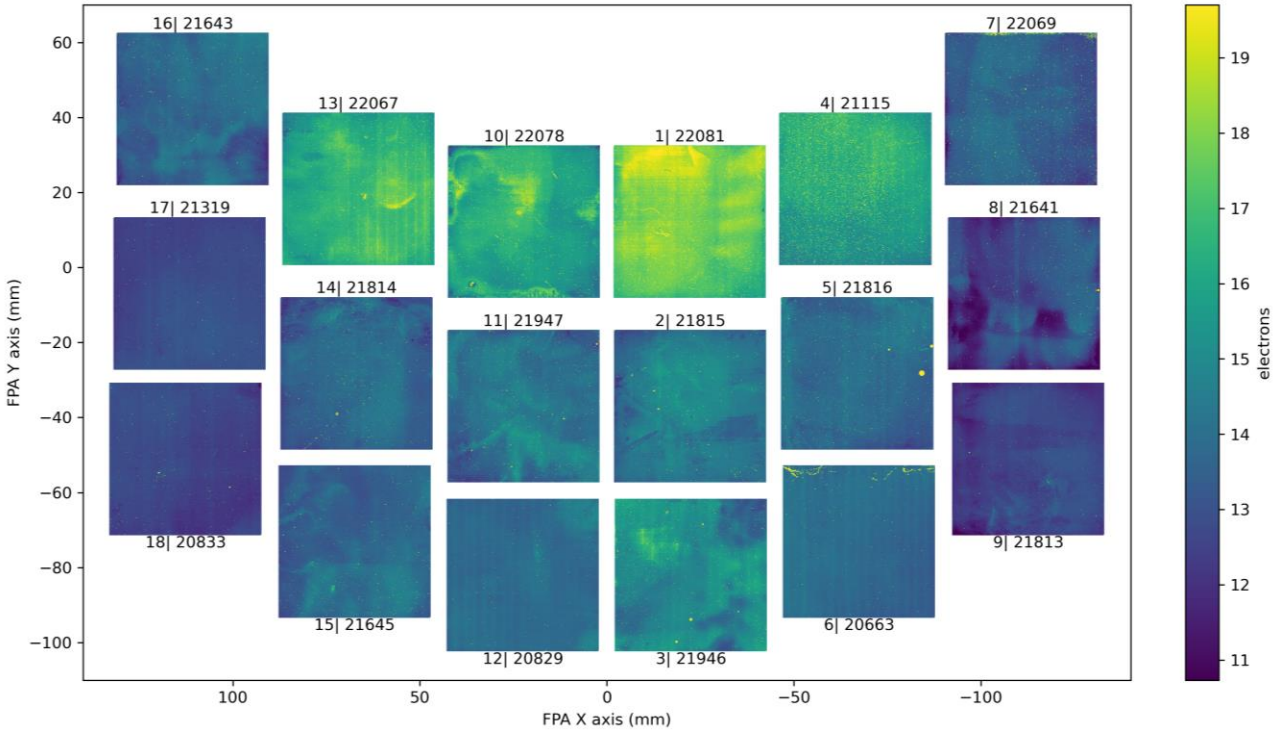

The following plots show the trending mean and median CDS noise over the whole array of each SCA. More information on CDS noise trending is on TDMS under RST-WFI-TN-0620.

Figure 35: Mean SCA CDS Noise Trending

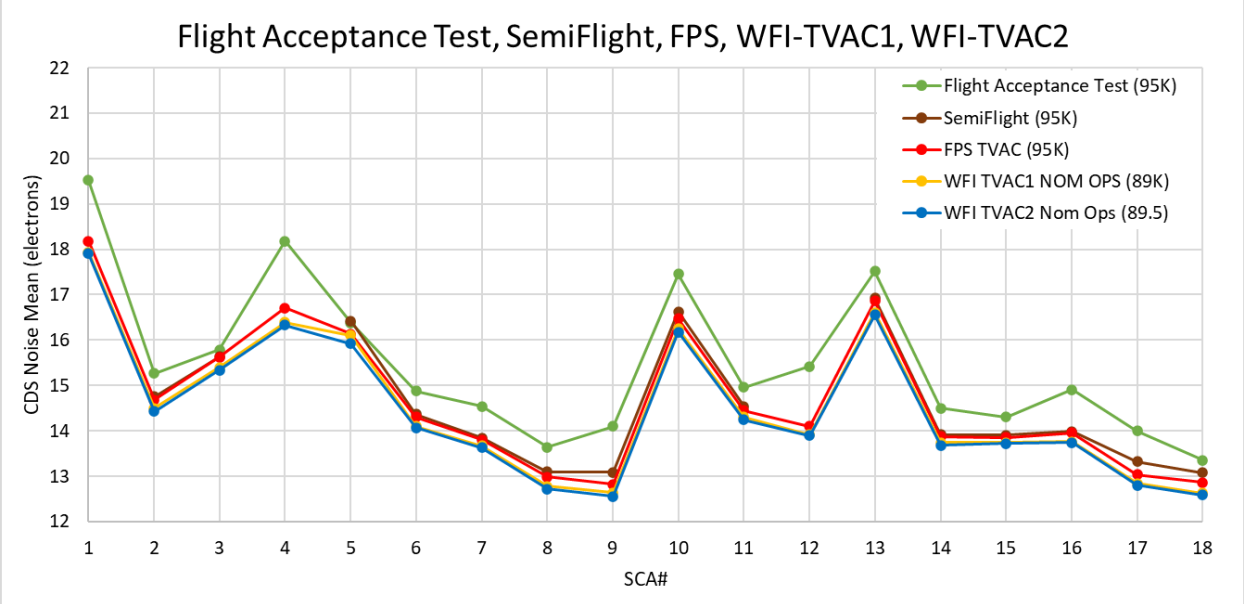

Figure 36: Median SCA CDS Noise Trending

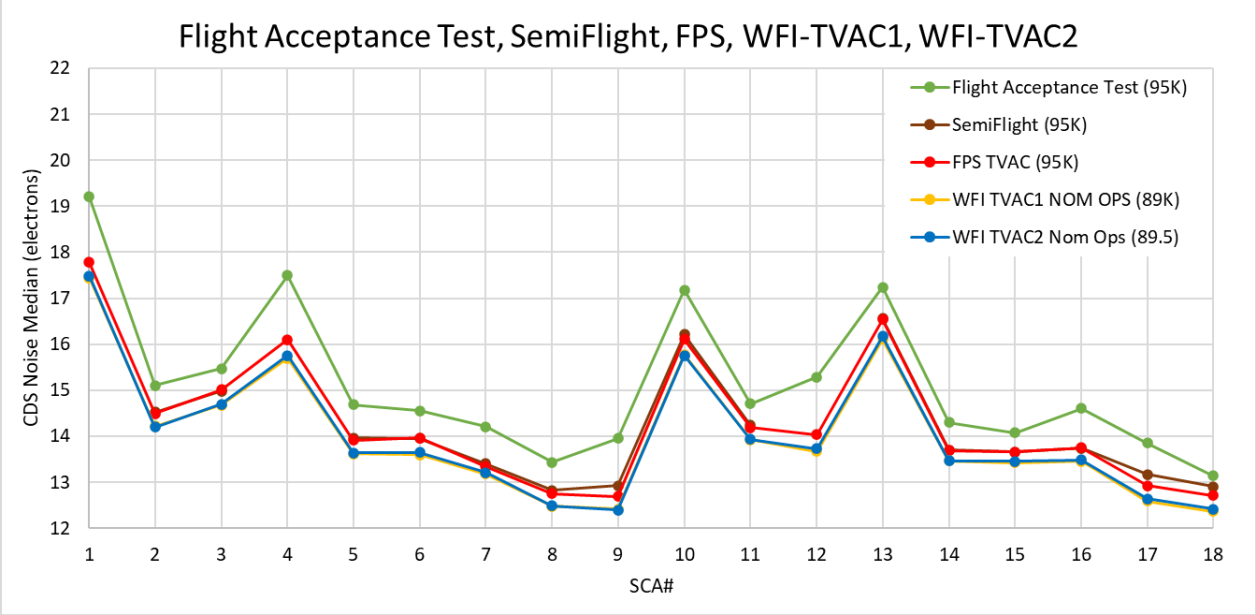

7.4 Low CDS, High Total Noise

There are regions of the detectors that are characterized by low CDS noise, with high total noise. *The Effect of Contact Resistance on Short Wavelength Infrared Focal Plane Array Noise* by E. C. Piquette (2024) offers an analysis of the contact resistance between the pixel MCT and an indium bump and suggests that high contact resistance is the cause of low CDS, high total noise behavior. The flight cohort of detectors was chosen to have minimal regions of low CDS/high total noise, but after the Semi-flight FPS TVAC test new regions appeared in some detectors. It is believed that this was caused by similar degradation mechanisms identified by the DD-ARB, including the contributing factor that SCA temperatures were driven to approximately 40C during decontamination bake-out in Semi-flight FPS TVAC. In between cryo-vacuum test campaigns the detectors are stored at ambient temperature, but the temperature of the FPA/WFI has been continually monitored and shall not exceed 23C.

New regions of low CDS noise / high total noise appeared in detector 22078 (SCU10) during the Semi-Flight FPS TVAC test. These regions were not present in previous tests. Figure 37 shows the CDS noise and total noise for detector 22078 during the Flight Acceptance Test and Triplet Test conducted at the DCL, and Semi-flight FPS TVAC. New regions of low CDS/high total noise are visible around the edges of the detector. Figure 38 and Figure 39 zoom in on two locations of this detector.

Figure 37: CDS noise and total noise in detector 22078 (SCU10) during Flight Acceptance Test, Triplet Test and Semi-Flight TVAC (units: electrons).

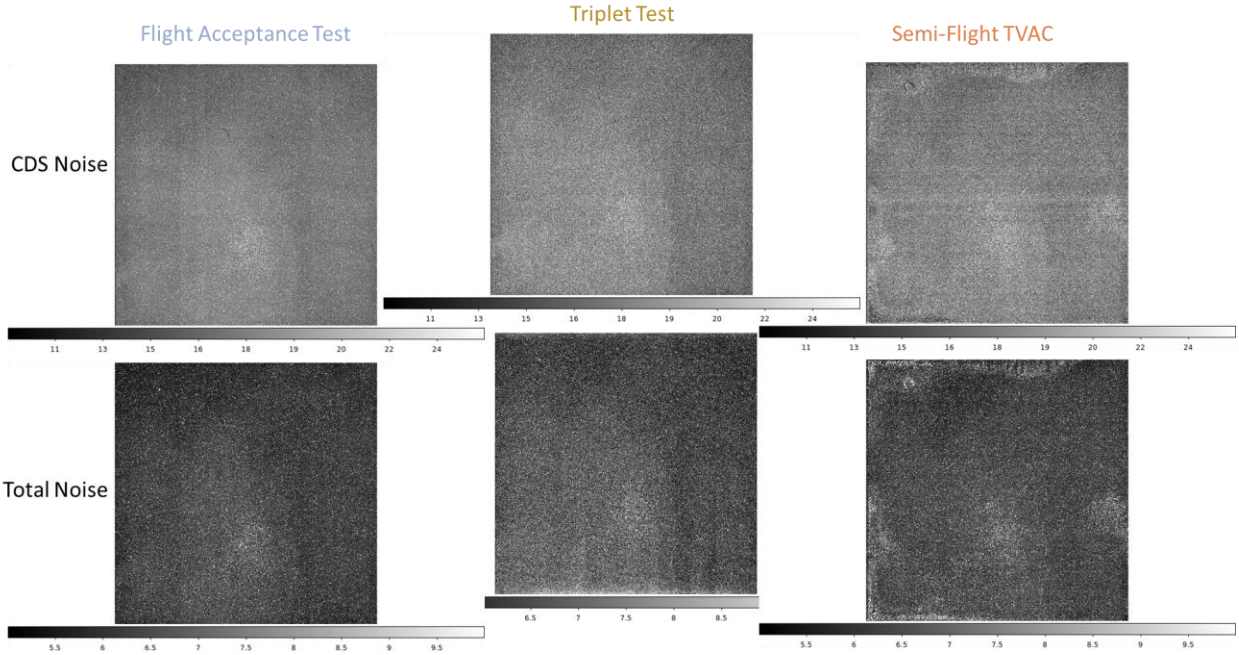

Figure 38: Region with coordinates (350:1100, 3500:4095) showing the evolution of a low CDS noise / high total noise region in detector 22078 (SCU10) (units: electrons).

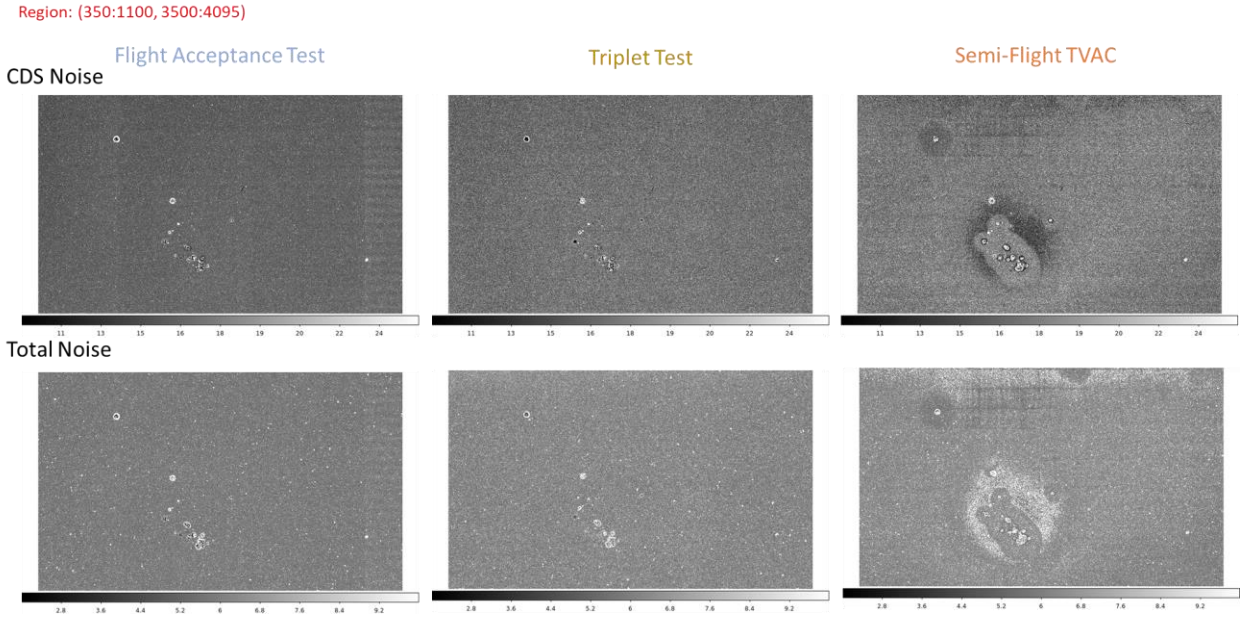

Figure 39: Region with coordinates (0:1500, 0:2100) showing the evolution of a low CDS noise / high total noise region in detector 22078 (SCU10) (units: electrons).

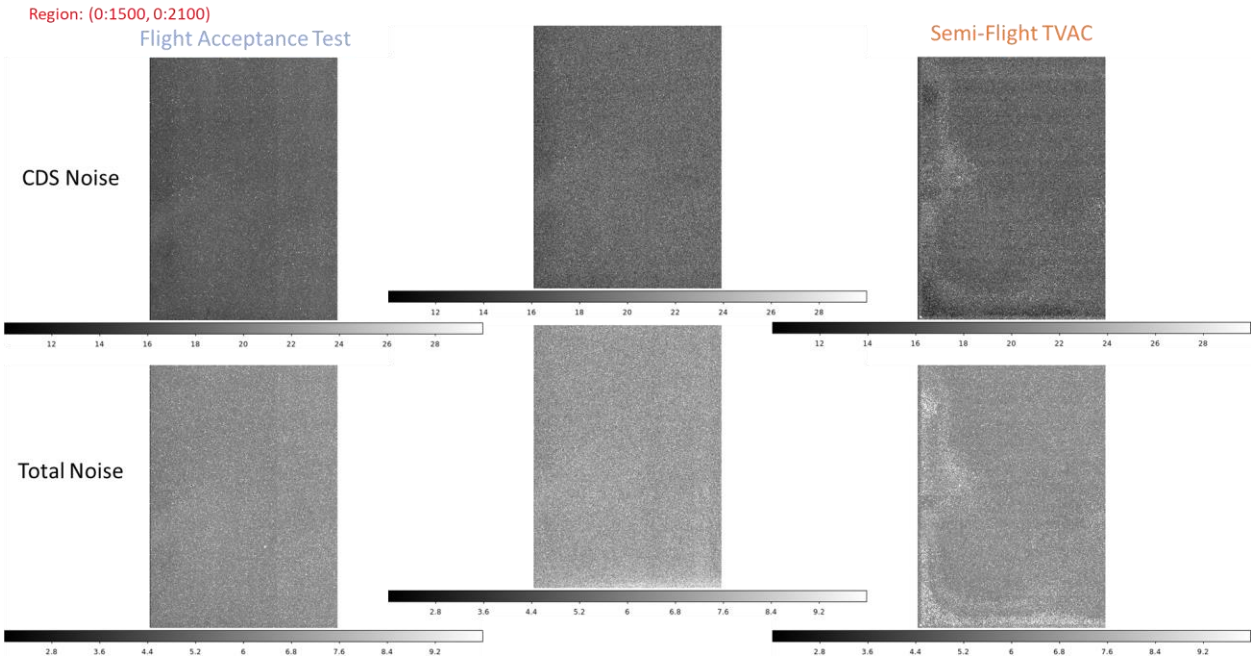

The size and shape of regions with low CDS noise and high total noise did not change significantly during subsequent tests for 22078. The CDS noise and total noise in this detector during WFI TVAC1 and WFI TVAC2 is shown in Figure 40 and Figure 41. However, the level of noise in these regions did increase as shown in Figure 42.

Figure 40: Total Noise for detector 22078 (SCU10) during WFI-TVAC1 and WFI-TVAC2.

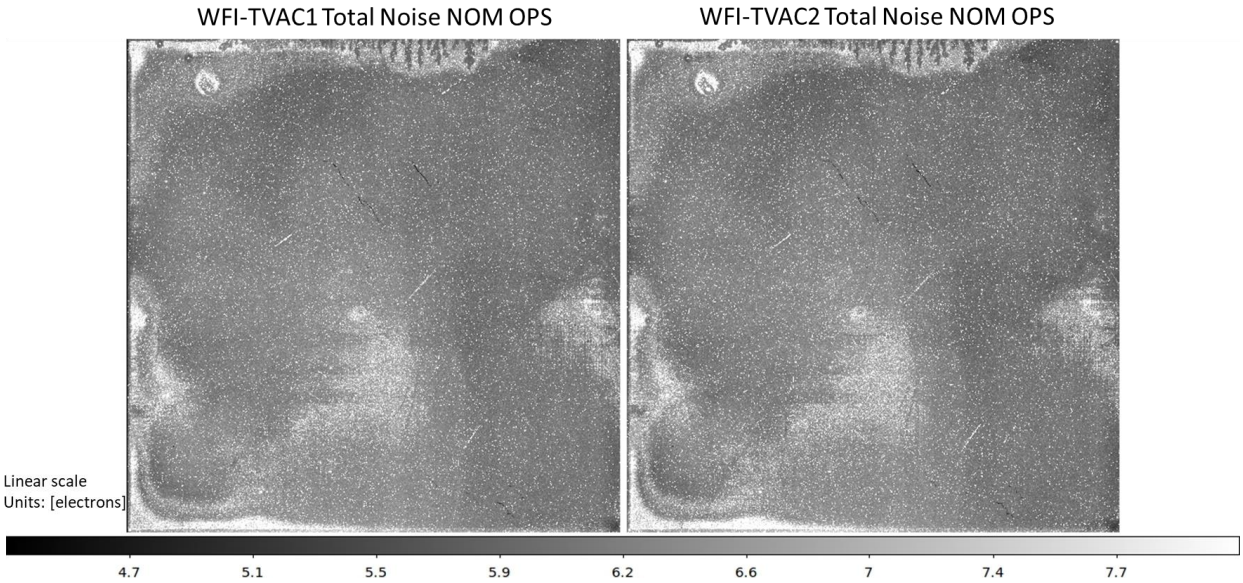

Figure 41: CDS Noise for detector 22078 (SCU10) during WFI-TVAC1 and WFI-TVAC2.

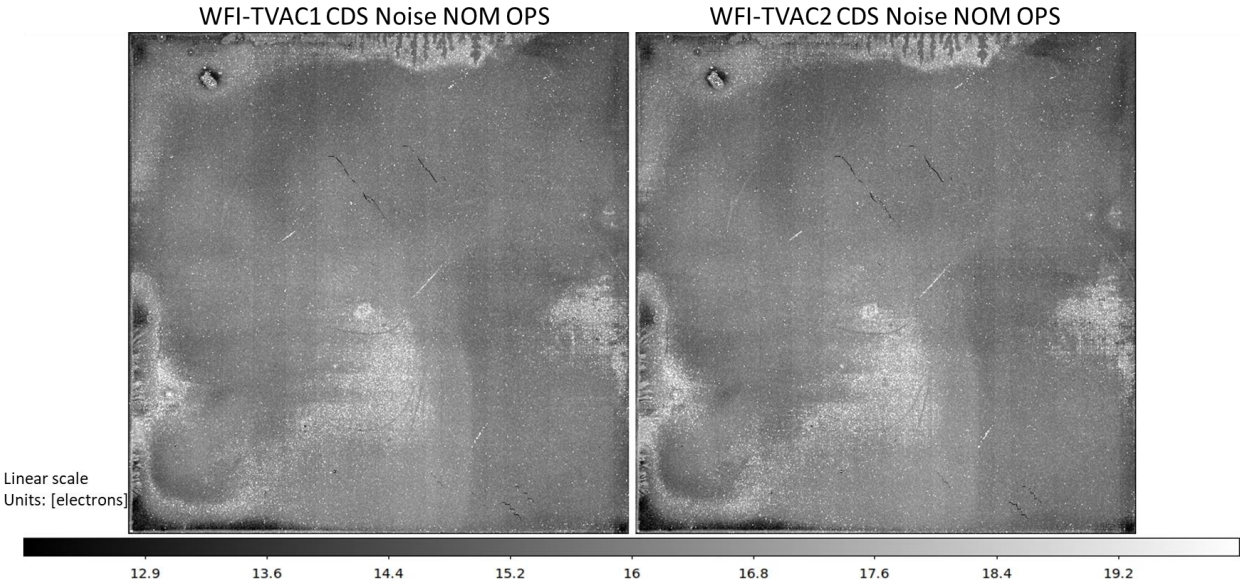

Figure 42: Normalized difference between WFI-TVAC2 and WFI-TVAC1 for Total Noise (left) and CDS Noise (right).

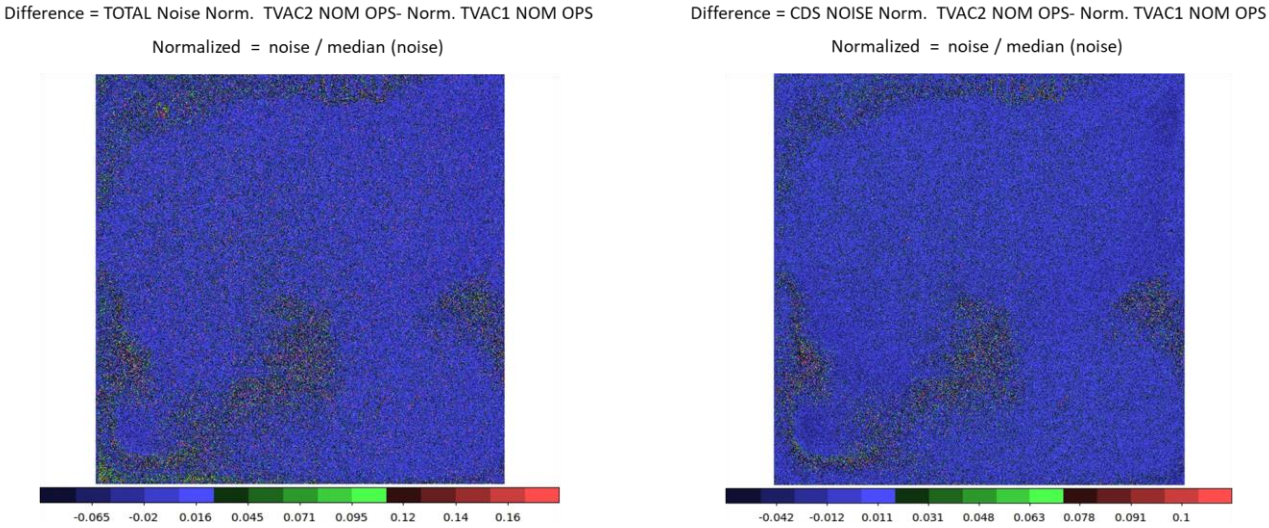

Regions of low CDS noise /high total noise are also associated with areas of higher persistence or slower persistence decay.

Additional detectors in the Focal Plane (20833, 21319, 21641, and 22081) also exhibit small regions of low CDS noise and high total noise. Unlike in detector 22078 these affected regions have not changed in size over time. However, all areas with low CDS and high total noise become more pronounced at lower operating temperatures so they were more noticeable during Nominal Operations in WFI TVAC1 and WFI TVAC2 testing environments (~89 K) compared to previous testing conducted in 95K environments.

Several tests were performed to investigate the low CDS noise/ high total noise behavior in flight spare detectors at the DCL. Some flight spare detectors (21224 and 21226) showed an increase in size and intensity of their low CDS noise/high total noise regions. Figure 43 shows the CDS noise of detector 21226 during the Flight Acceptance Test, and subsequent Triplet Flight Run (FR) tests FR7, FR10, and FR11. The tests showed an increase in the low CDS noise region. Figure 44 shows the ratio between the CDS noise (left) and total noise (right) during FR10 and the Flight Acceptance Test. These ratios show that areas where CDS noise decreased also saw an increase in total noise.

Figure 43: CDS Noise in detector 21226 during Flight Acceptance Test, FR7, FR10, and FR11.

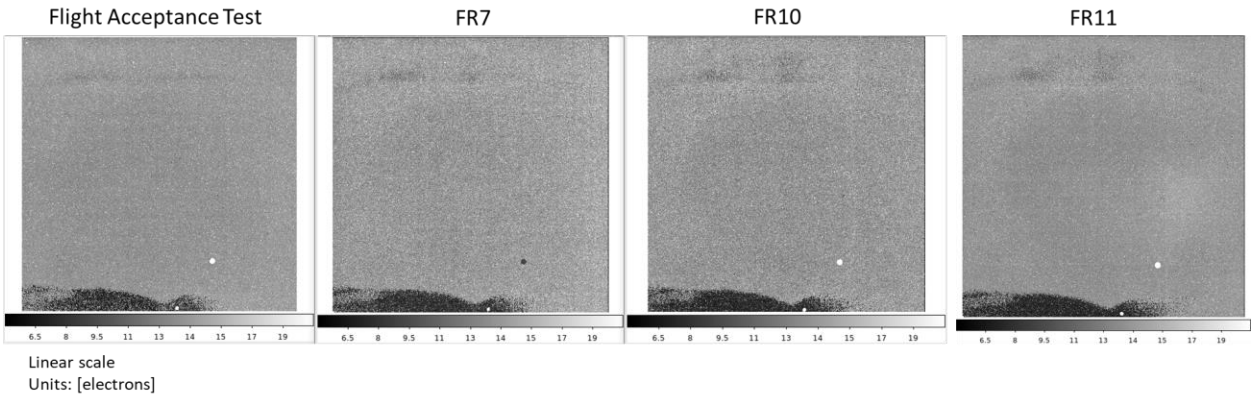

Figure 44: Ratio of CDS noise (left) and total noise (right) between FR10 and Flight Acceptance Test for 21226.

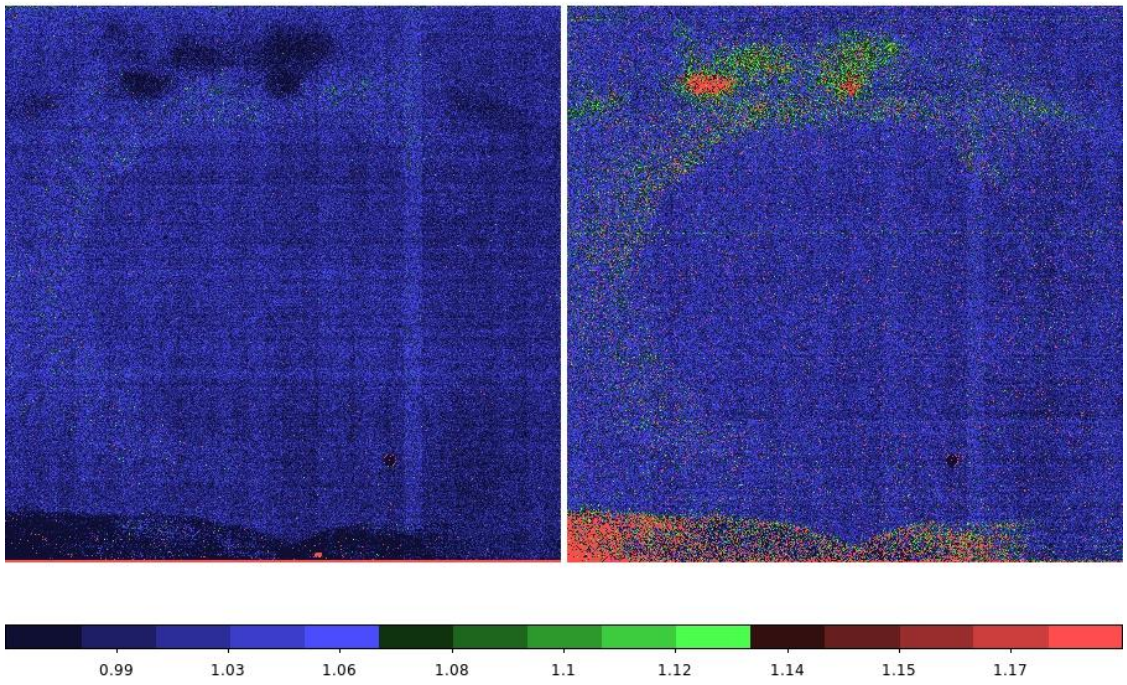

7.5 Low Noise – High Nonlinearity

About 0.1% of pixels across all detectors show abnormally low total noise and CDS noise and fail per pixel gain calculation. They are not obviously anomalous in a dark or illuminated image, but they are completely unrecoverable. One theory is that these pixels are electrically connected to their neighbors when they should not be. This class of bad pixels is now included in the operational masks. Some examples are shown in the Figure below and appear as linear features of darker-colored pixels.

Figure 45: Regions of SCAs generated with WFI-TVAC2 data for SCU1, SCU10, and SCU18

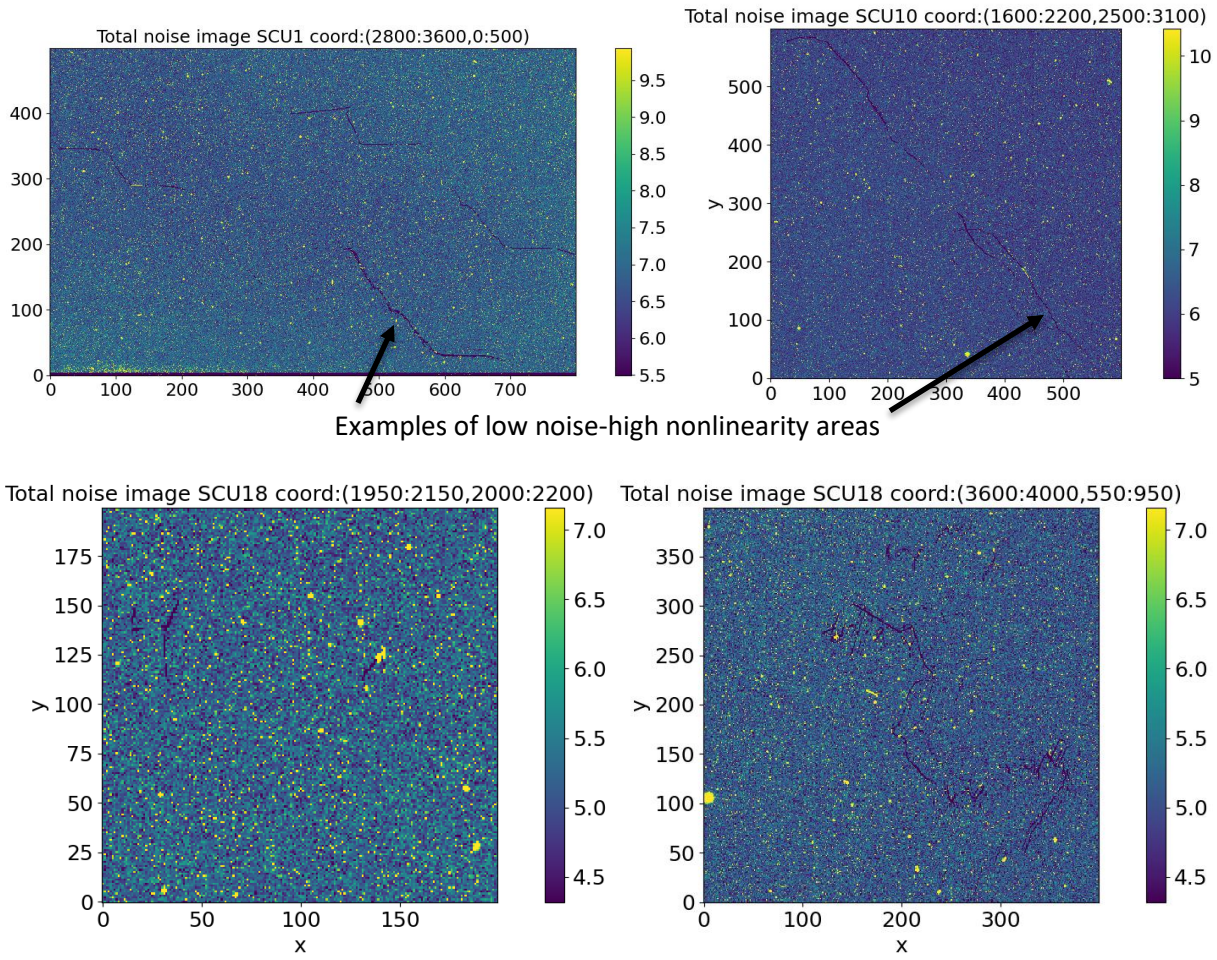

The Table below shows the percentage of pixels that fail per pixel gain calculation for each flight detector.

Table 9: Percentage of pixels failing per pixel gain calculation.

SCU#	SCA	% Fail Per Px Gain Calculation
1	**22081**	0.12
2	**21815**	0.07
3	**21946**	0.08
4	**21115**	0.12
5	**21816**	0.07
6	**20663**	0.13
7	**22069**	0.15
8	**21641**	0.07
9	**21813**	0.07
10	**22078**	0.12
11	**21947**	0.08
12	**20829**	0.07
13	**22067**	0.08
14	**21814**	0.08
15	**21645**	0.06
16	**21643**	0.07
17	**21319**	0.10
18	**20833**	0.25

8 LINEARITY

8.1 Classical Nonlinearity

Linearity is the measure of how well a pixel can be corrected to fit a linear ideal signal. For the RST WFI FPS we perform linearity analysis using the linearization method described in *A New Non-Linearity Correction Method for NIRCam* by A. Canipe, M. Robberto, and B. Hilbert. The flow chart and equations below describe the steps for the classical non-linearity analysis.

Figure 46: Linearity Analysis Flow Chart

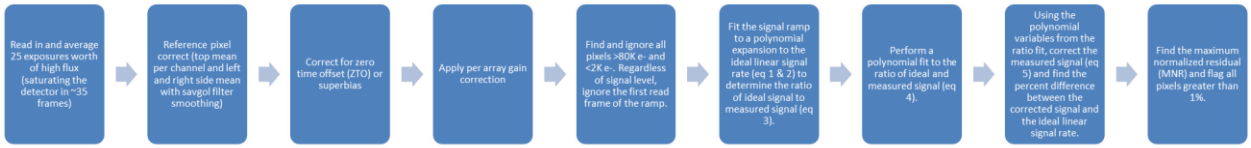

Figure 47: Linearity Equations from Canipe

$$s_{meas,i} = B + At_i + C \cdot (At_i)^2 + D \cdot (At_i)^3 + E \cdot (At_i)^4 + F \cdot (At_i)^5 + \cdots \quad (1)$$

$$s_{ideal,i} = B + At_i \quad (2)$$

$$R_{meas,i} = \frac{s_{ideal,i}}{s_{meas,i}} \quad (3)$$

$$R_{fit,i} = \alpha + \beta s_{meas,i} + \gamma \cdot (s_{meas,i})^2 + \delta \cdot (s_{meas,i})^3 + \zeta \cdot (s_{meas,i})^4 + \cdots \quad (4)$$

$$s_{corr,i} = s_{meas,i} \cdot [\alpha + \beta s_{meas,i} + \gamma \cdot (s_{meas,i})^2 + \delta \cdot (s_{meas,i})^3 + \cdots] \quad (5)$$

The linearity correction polynomial is calculated using flat-field illuminated exposures and frames with signal between 2000 and 80,000 electrons and thus is only valid for signal levels within this range. The Maximum Normalized Residual (MNR) is a measure of the goodness of this fit and is calculated as the maximum value of 100% * (Corrected signal – Ideal signal) / Ideal signal for all frames between 2,000 and 80,000 electrons.

8.1.1 Including or excluding the first read frame

For the initial FPS level analysis of linearity data, we found that the first read frame of a ramp was slightly out of line with the rest of the frames. This was most evident when comparing the accuracy plot for fits with and without the first read frame.

Figure 48: MNR values for SCU08 pixels either excluding or including the first read frame

$$\frac{(Corrected\ Signal\ -\ Ideal\ Linear)}{Ideal\ Linear} \times 100\%$$

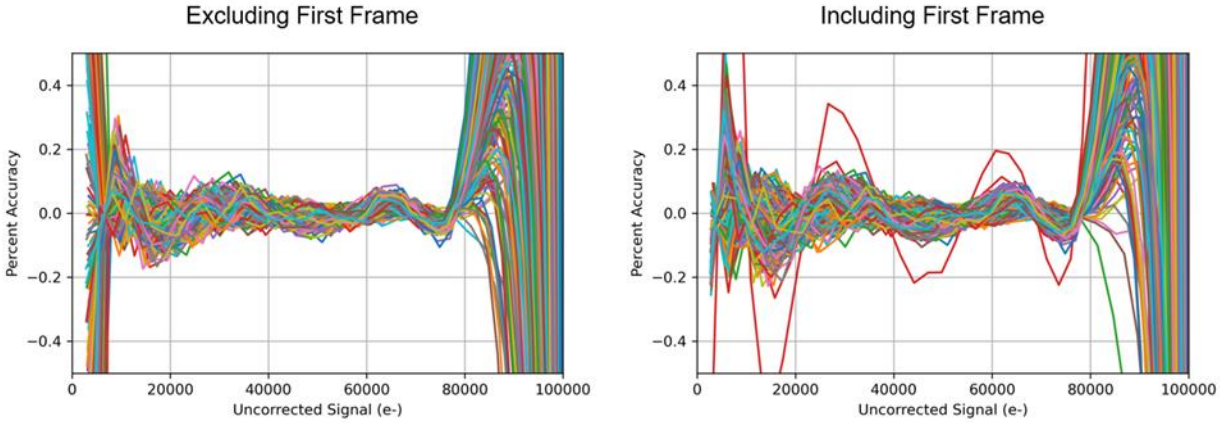

Analysis was run with including and excluding the first read frame. Linearity correction for both methods yielded good accuracy if the first frame accuracy is ignored and not included in the fit. Due to the discrepancy of the first frame the decision was made to continue through linearity analysis excluding the first read frame from the fit of the measured signal. Figure 49 and Figure 50 show the linearity correction accuracy plots for 400 pixels spread in a grid throughout SCA01.

Figure 49: Flight FPS TVAC Linearity Correction Accuracy Plot (ZTO Method, SCA01 400x pixel subset)

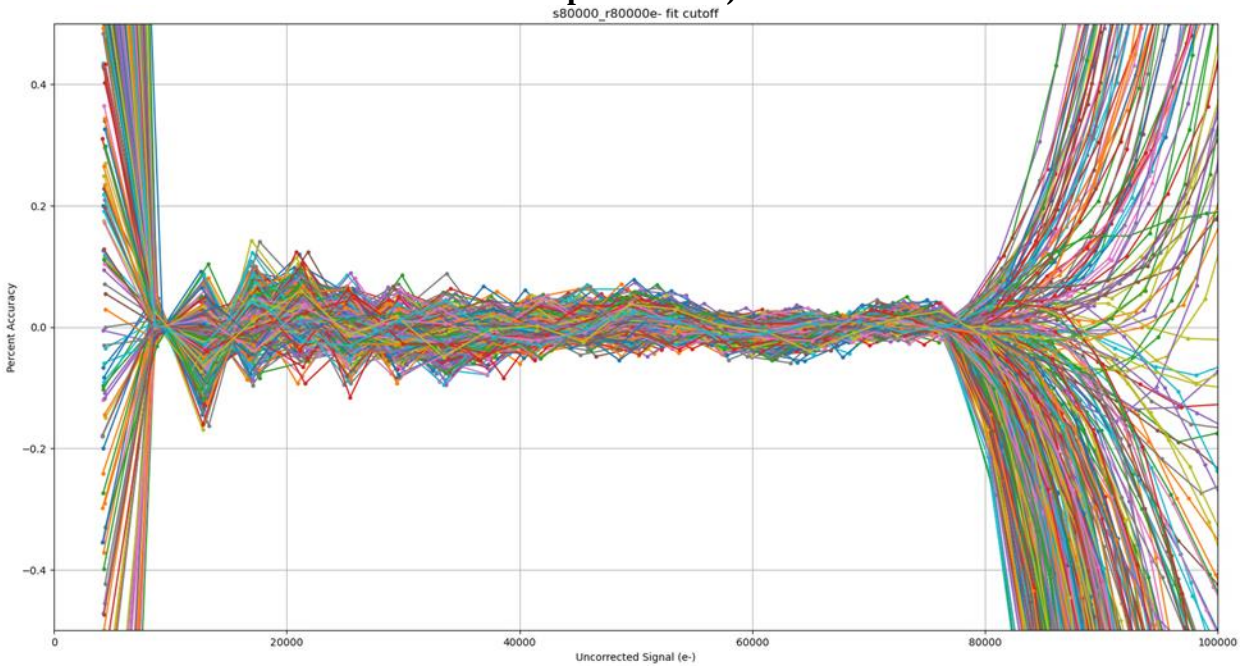

Figure 50: Flight FPS TVAC Linearity Correction Accuracy Plot (SB Method, SCA01 400x pixel subset)

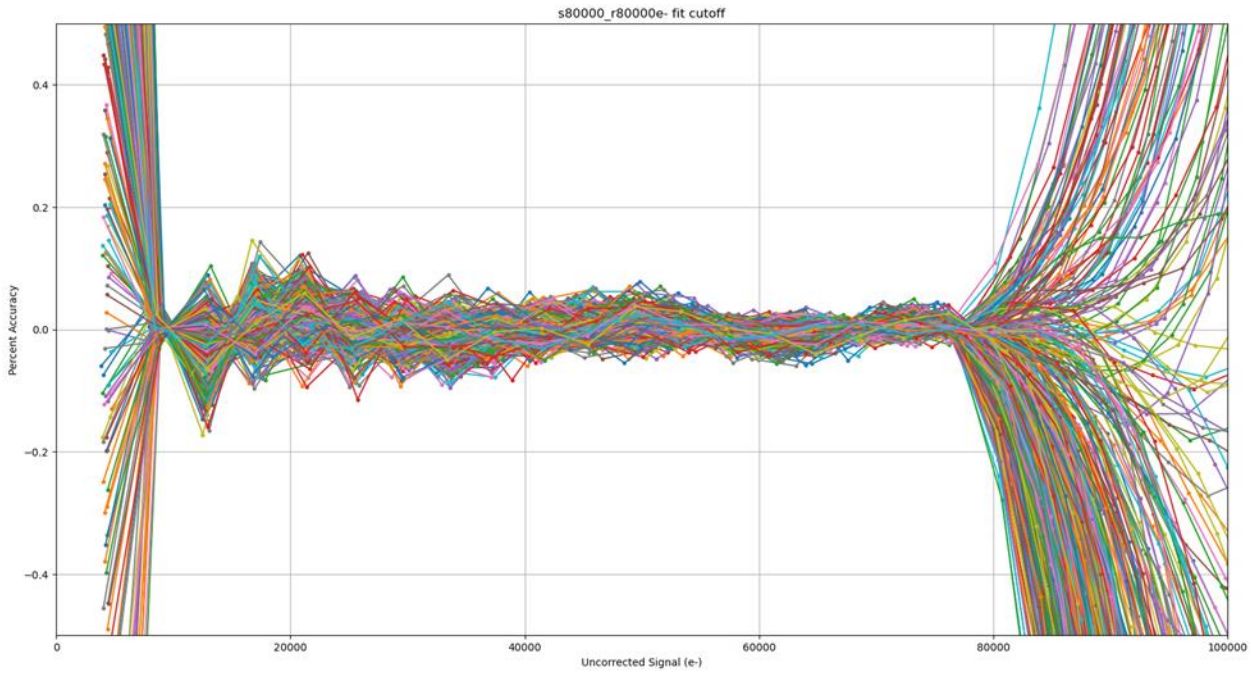

8.1.2 ZTO vs Superbias

The two main methods used for zero frame correction of FPS data are zero time offset (ZTO) and superbias (SB). The ZTO method fits a second order polynomial for each pixel to read frames 2-7 (note we are skipping the first read frame due to its out of family behavior explained in 8.1.1) and extrapolating back to “zero time” or just after a pixel has been reset. The constant of the second order polymonial is subtracted from all frames. The superbias method creates a correction frame from the per pixel median of the second frame of 100 noise exposures. This correction frame is subtracted from all frames in the ramp.Figure 51 Figure 51 shows the reference pixel correction and either ZTO or SB correction to raw linearity data for a single pixel.

Figure 51: Reference pixel and either ZTO or SB correction to raw data

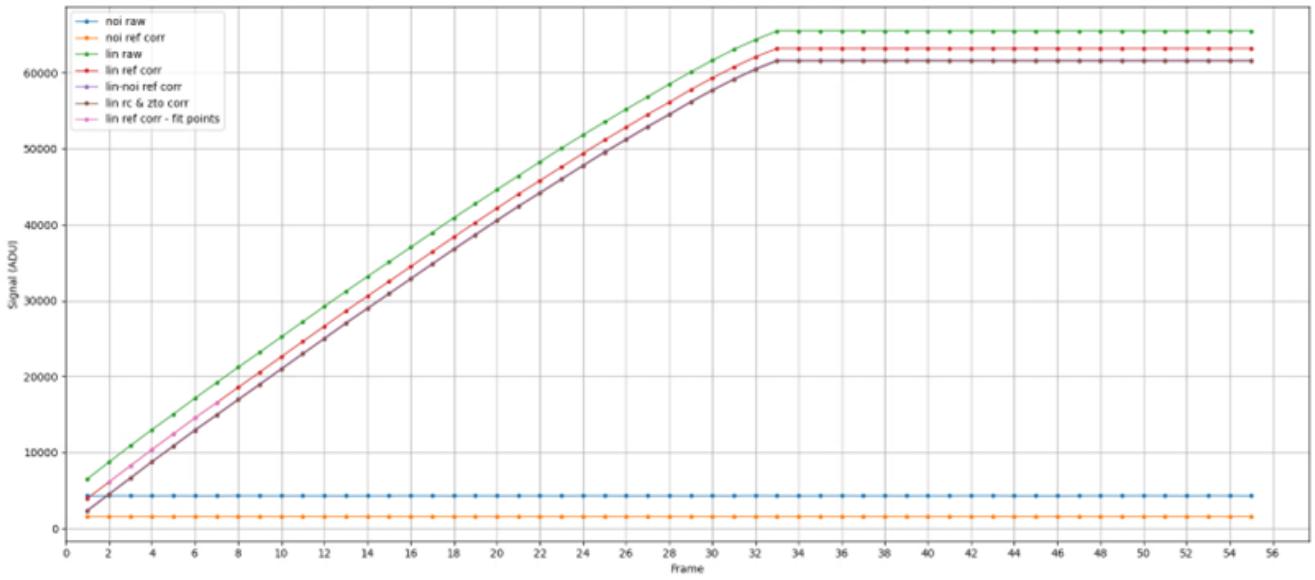

Both corrections for a single plot look very similar but there is a spatial pattern that can be seen across each of the 32 SCA output channels. Figure 52 shows the ratio of a reference corrected, superbias corrected data frame and a reference corrected, ZTO corrected data frame. Further analysis of the ZTO pattern is presented in Section 9.

Figure 52: Superbias/ZTO corrected Data Frame

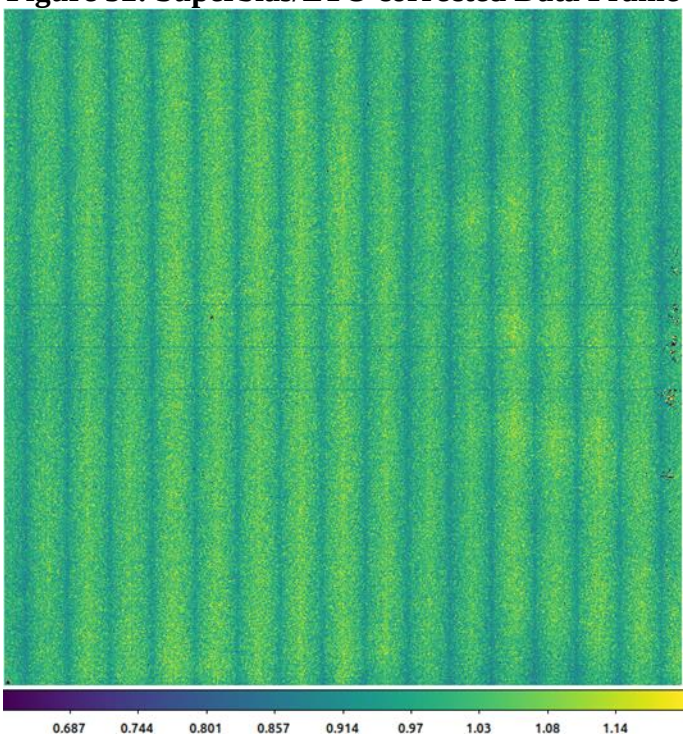

To determine if this effect causes a significant difference on the linearity results, the data was run through the linearity routine using data that was corrected with both (SB and ZTO) methods. The MNR results also showed a similar spatial pattern. The full MNR mosaic can be seen in Figure 53

Figure 53: Superbias/ZTO MNR Mosaic

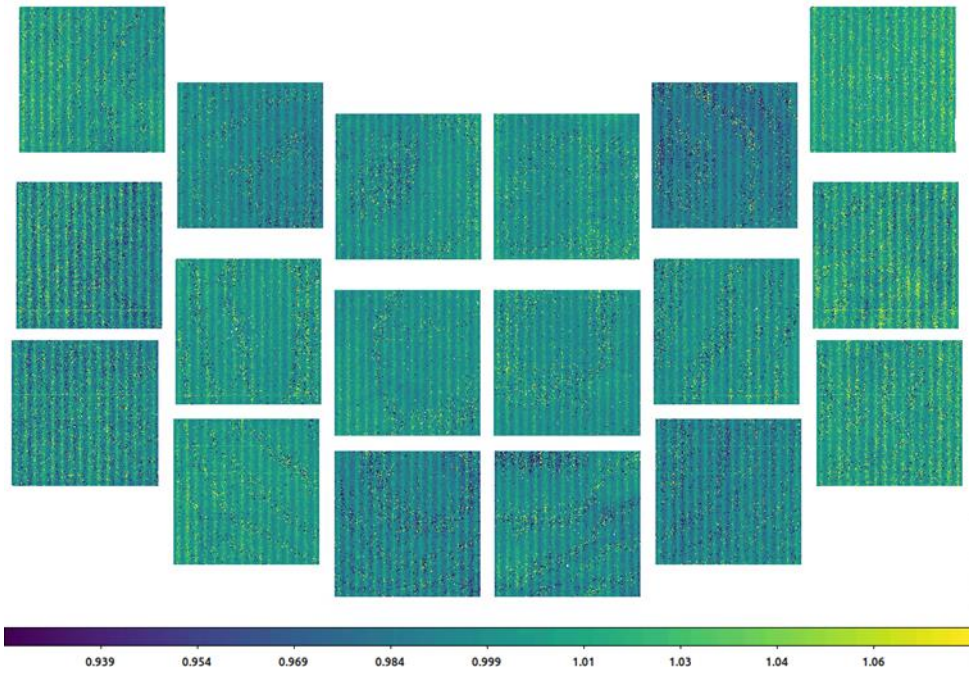

Even with the spatial pattern there is very little difference between the linearity results using either the ZTO or SB methods for zero frame correcting. This left to right pattern is found in all data sets, but the ZTO method seems to correct it. So, for the vast majority of the linearity analysis during ground testing the plan is to use the ZTO method for classical nonlinearity correction.

8.1.3 Results

Final analysis of flight FPS TVAC data showed that all SCAs have more than 99.3% of pixels passing the 1% linearity specification and all but SCA07 (22069) have more than 99.75% of pixels passing. Figure 54 shows the MNR mosaic. Figure 55 shows the broad MNR histograms [0-6% MNR] as well as a histogram focused on the main distribution of pixels [0-0.5% MNR] for each SCA. Figure 56 shows the mosaic of passing vs failing pixels.

Figure 54: Zero Time Offset Correction, FLT FPS TVAC, Maximum Normalized Residual Mosaic (MNR units in %)

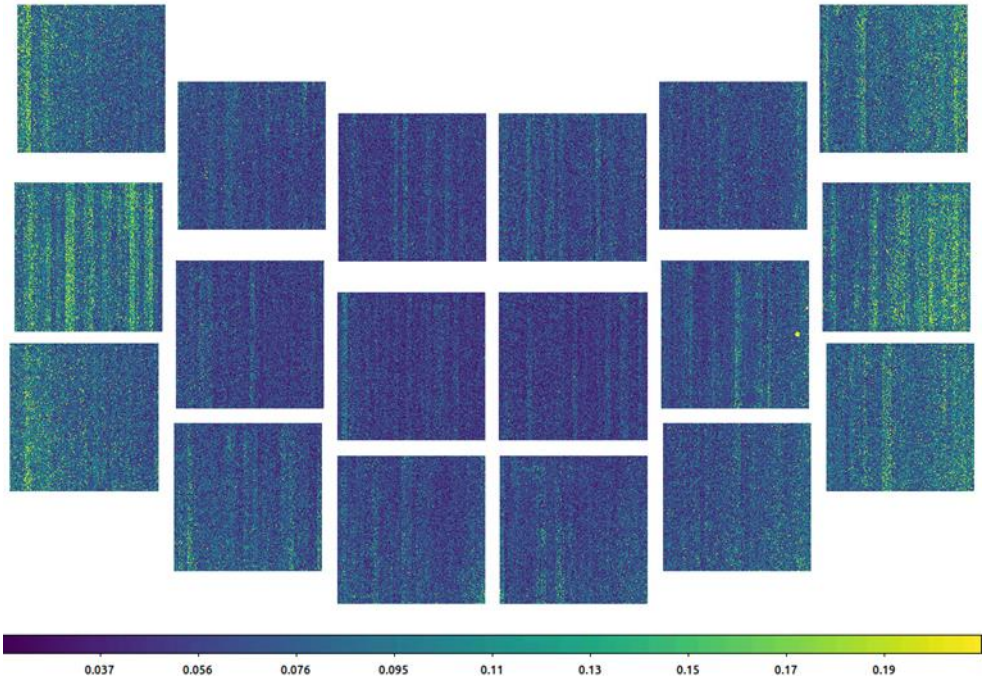

Figure 55: MNR Histograms for the flight SCAs

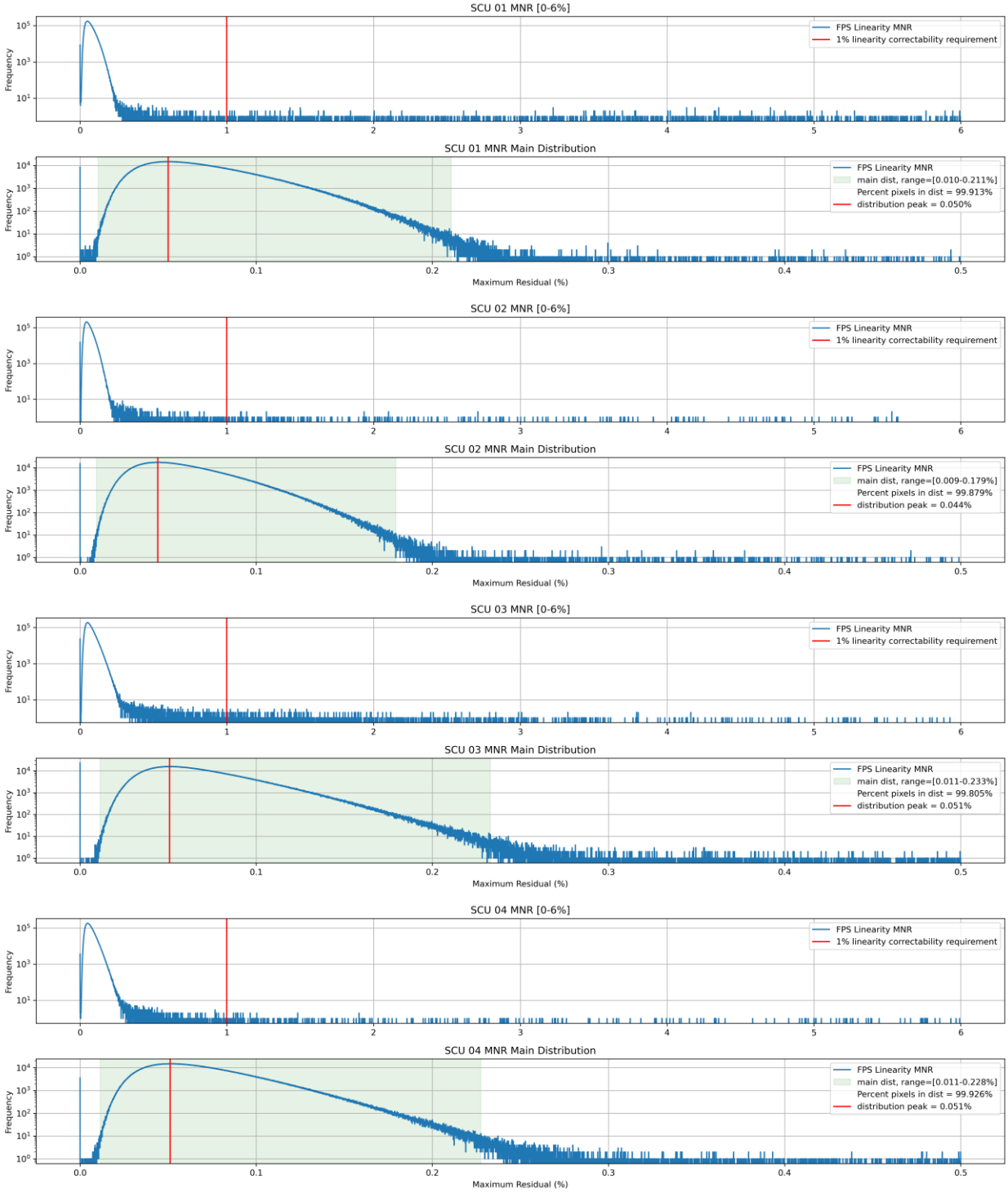

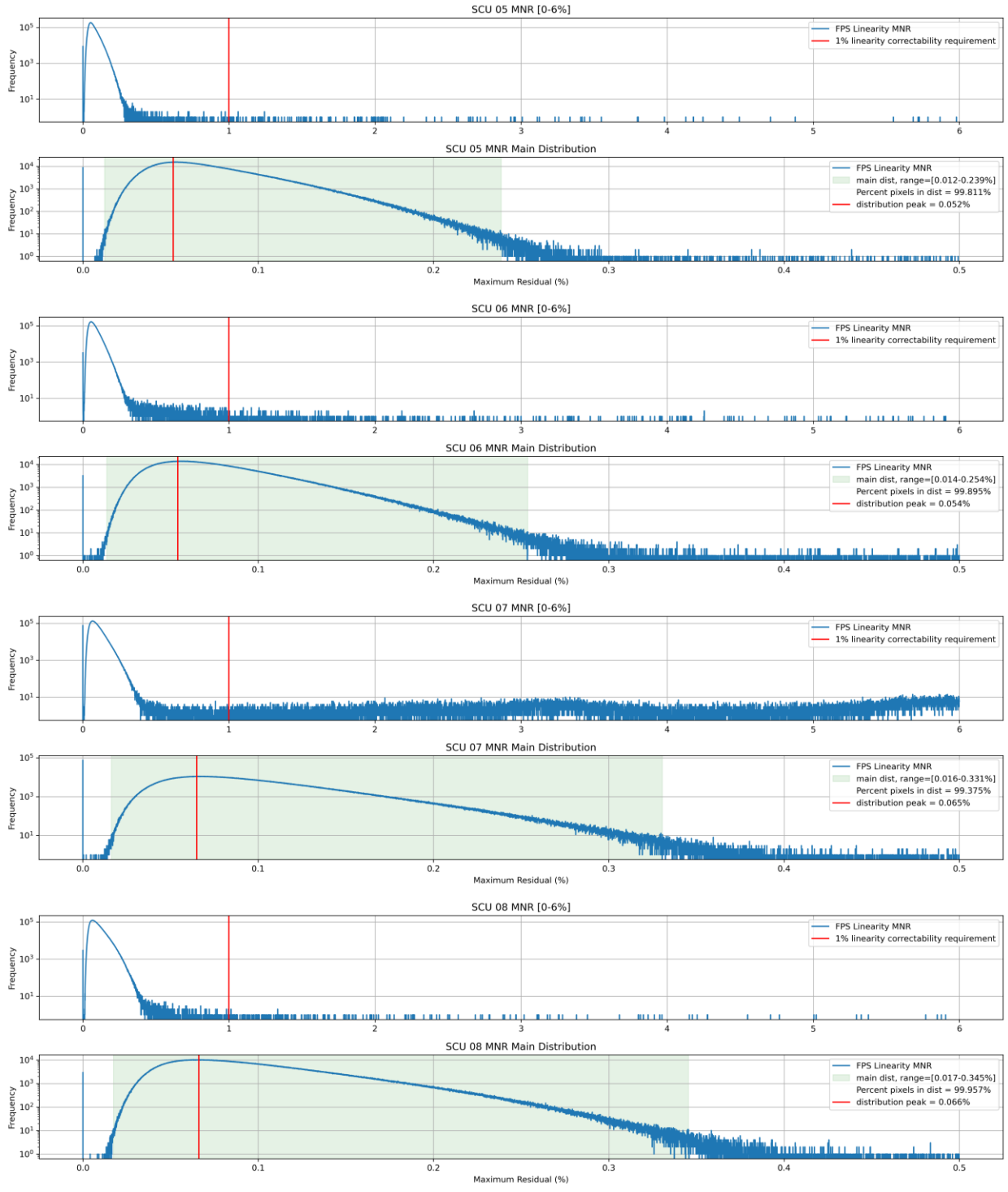

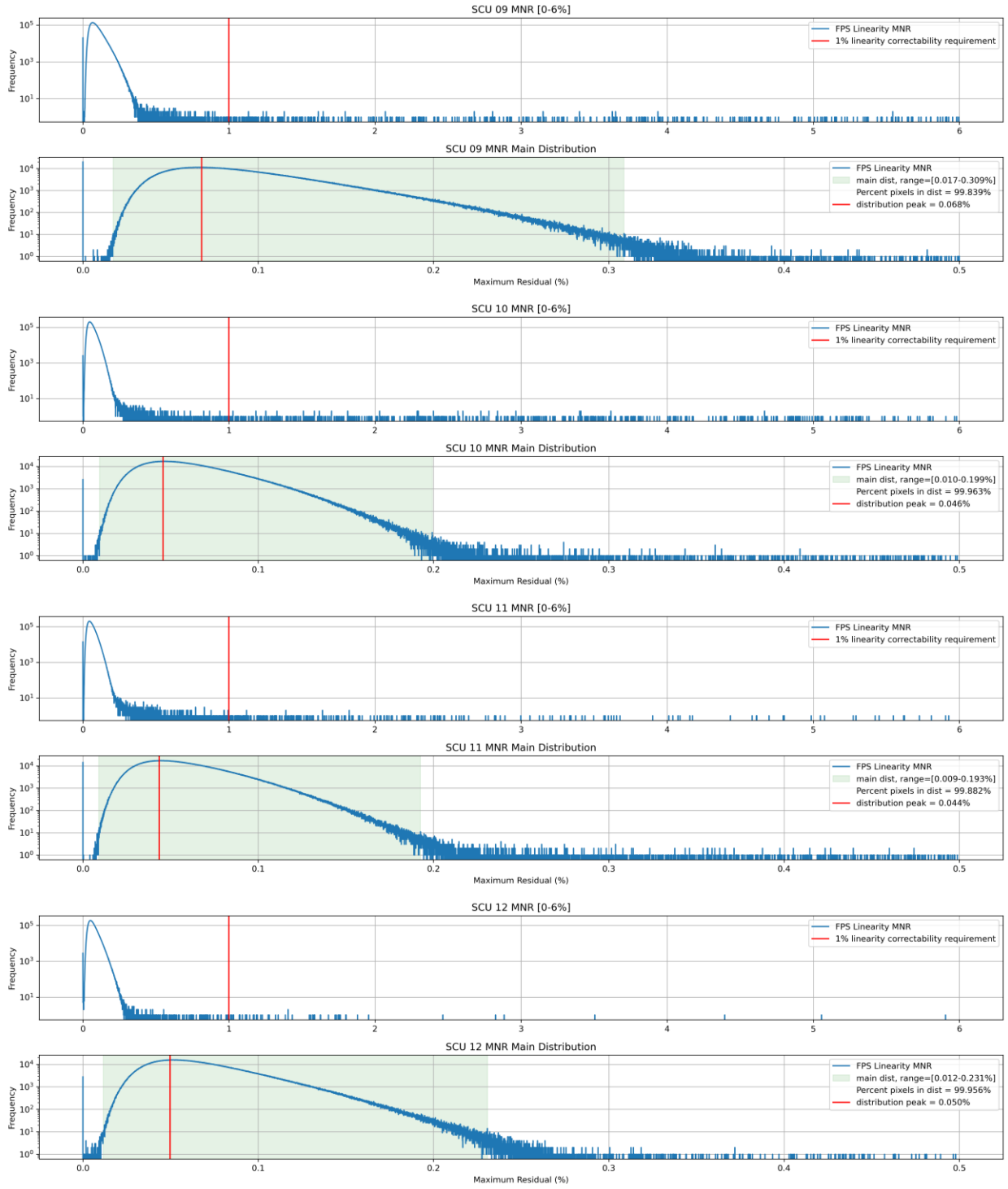

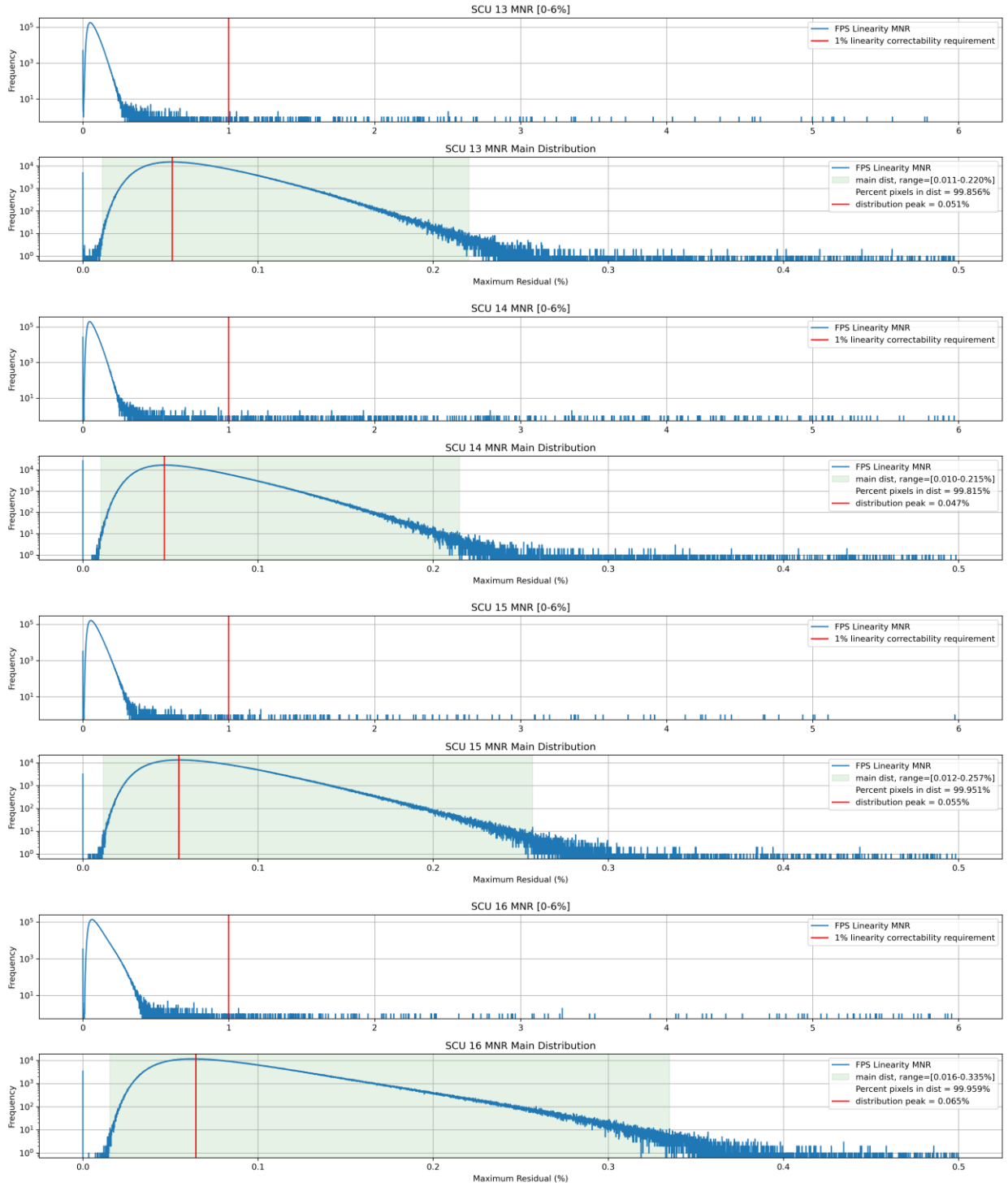

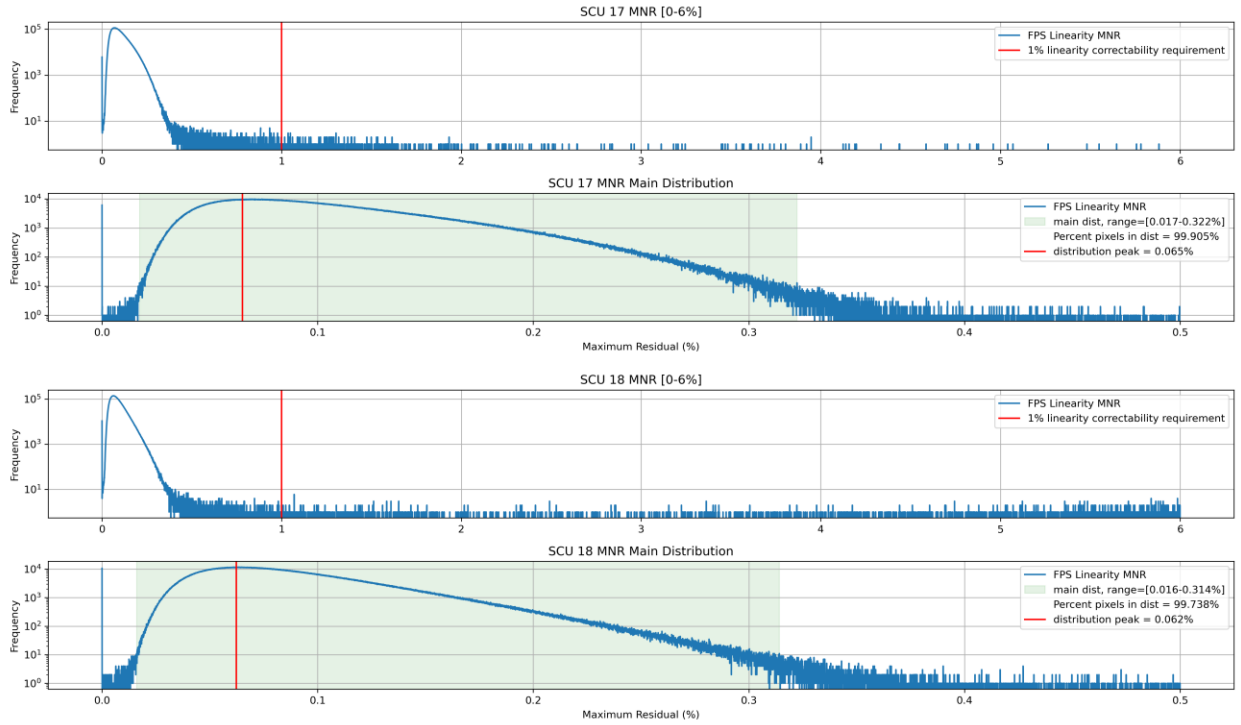

Figure 56: Flight FPS TVAC Linearity Pass/Fail Mosaic (ZTO Method)

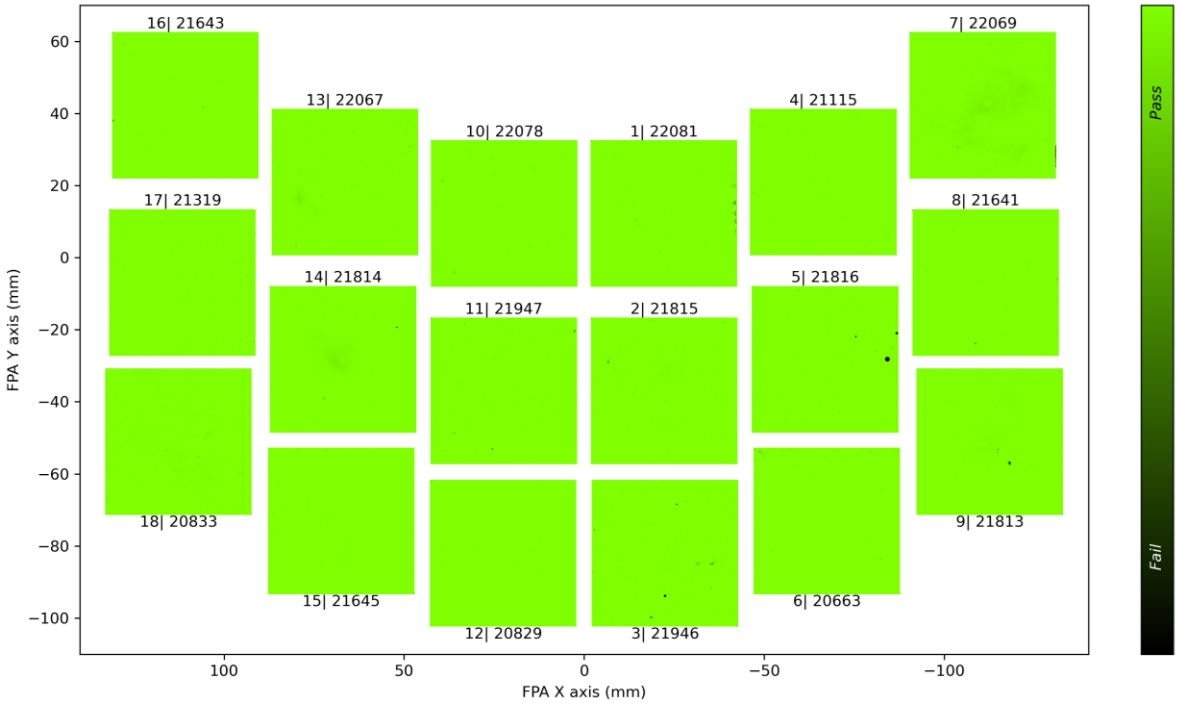

Table 10 shows the percent of pixels passing 1% linearity for both the superbias and the ZTO correction methods.

Table 10: Flight FPS TVAC Linearity Percent Pixels Passing Per SCA

SCA Number	Superbias Percent Pixels Passing (%)	ZTO Percent Pixels Passing (%)
1	99.928	99.928
2	99.892	99.893
3	99.826	99.827
4	99.947	99.947
5	99.824	99.824
6	99.920	99.921
7	99.397	99.397
8	99.975	99.975
9	99.854	99.854
10	99.975	99.975
11	99.898	99.898
12	99.969	99.969
13	99.872	99.872
14	99.829	99.829
15	99.964	99.964
16	99.975	99.975
17	99.928	99.928
18	99.762	99.763

To test out the linearity polynomials that were found, the linearization correction method was applied to five different flux tests across the FPS and WFI testing campaign. The resulting plots for the 400 pixel grid of SCA01 is shown in Figure 57. These five flux levels range from ~5,000 to ~50,000 linearized electrons over 11 frames.

Figure 57: Linearized Data Sets

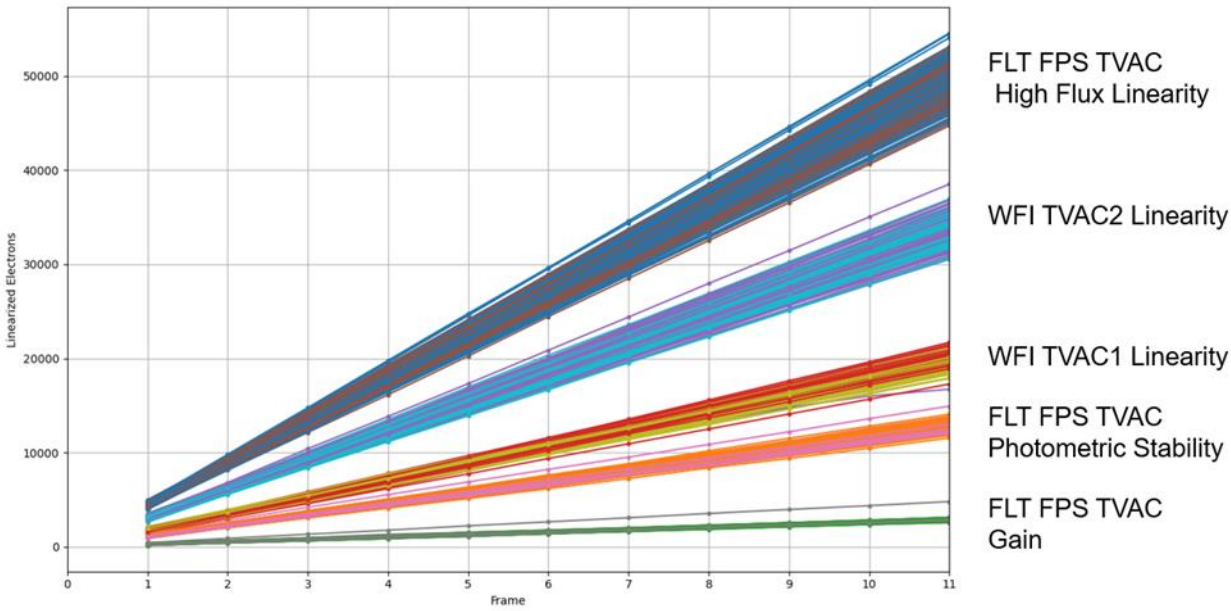

The small caveat to the linearity statistics shown up to this point is that for most of the Flight FPS TVAC test there was a 16x16 guide window in the bottom left side of all 18 SCA active areas. The analysis method causes these guide window pixels to fail even though they may have passed if they were accumulating signal normally like the rest of the pixels. For WFI TVAC2 there were two different linearity test runs. One had the guide window in the same bottom left corner but the second moved the guide window to the top right corner. So, linearity analysis was run on both data sets and the results were combined to fill in the gaps caused by guide windows. As seen in Table 11, this shows a slight increase in pixels passing between Flight FPS TVAC and WFI TVAC2. The final combined (not missing 16x16 GWs) linearity polynomials can be found on the analysis archive at /fpe/analysis/quicklook/reference/Linearity/v2/ and on ADAPT at /css/romanst/archive/aux/WFI_TVAC2_operability/linearity_v2/.

Table 11 Linearity Percent Pixels Passing Per SCA

SCA Number	ZTO FLT FPS TVAC Percent Pixels Passing (%)	ZTO WFI TVAC2 Percent Pixels Passing (%)	ZTO WFI TVAC2 Percent Pixels Passing (%)
Missing GW?	Yes (16x16)	Yes (16x16)	No
1	99.928	99.909	99.912
2	99.893	99.893	99.895
3	99.827	99.831	99.834
4	99.947	99.953	99.955
5	99.824	99.826	99.828
6	99.921	99.919	99.922
7	99.397	99.400	99.402
8	99.975	99.974	99.976
9	99.854	99.854	99.856

10	99.975	99.976	99.978
11	99.898	99.899	99.901
12	99.969	99.968	99.972
13	99.872	99.874	99.876
14	99.829	99.830	99.832
15	99.964	99.965	99.966
16	99.975	99.975	99.977
17	99.928	99.927	99.929
18	99.763	99.764	99.767

8.2 Count-rate Nonlinearity (CRNL)

A pixel ramp is ultimately used, preferably post classical nonlinearity correction, to find the rate at which charge integrates at that pixel. Ideally the inferred charge integration rate will be perfectly linear with the flux incident on the pixel. However, a small nonlinearity between flux and charge integration rate is realistic for present-day H4RG detectors. The terms flux dependent nonlinearity (FDNL), count rate nonlinearity (CRNL), and reciprocity failure all refer to that nonlinearity. It has been characterized in most WFI FPA detectors at the DCL and in all FPA detectors with the sRCS in WFI TVACs and will be monitored for changes during flight with the sRCS using the lamp-on lamp-off (LOLO) and Combinatorial Flux Addition (CFA) techniques.

8.2.1 CRNL in WFI TVAC2

CFA tests were run during WFI TVAC2 ColdQual and NomOp plateaus (89.5K) using sRCS bands 1 (F062, 625nm band center), 2 (F087, 855nm band center), 3 (F106, 1040nm band center), 5 (F158, 1485nm band center), and 6 (F184, 1675nm band center). Band 4 was omitted due to flux stability issues. These bands correspond to Light Emitting Diodes (LEDs) of different wavelengths. The sRCS has two identical sets of LEDs, known as Bank 1 and Bank 2 LEDs. Flat field illumination from the two LED banks was used to conduct the CFA test, which covered fluxes between 0.3 e-/pixel/s and 7776 e-/pixel/s. The number of frames per exposure was adjusted to reach targets of 400 e-, 3000 e-, and 40000 e- depending on the flux level. Up-the-ramp frames from each exposure were divided into superpixels for reference pixel correction, background correction, and CNL correction. Frame-by-frame differences between CNL corrected ramps was then to used obtain count rates for each flux for each superpixel.

Figure 58: Fit of SCA 8 signal over all flux levels

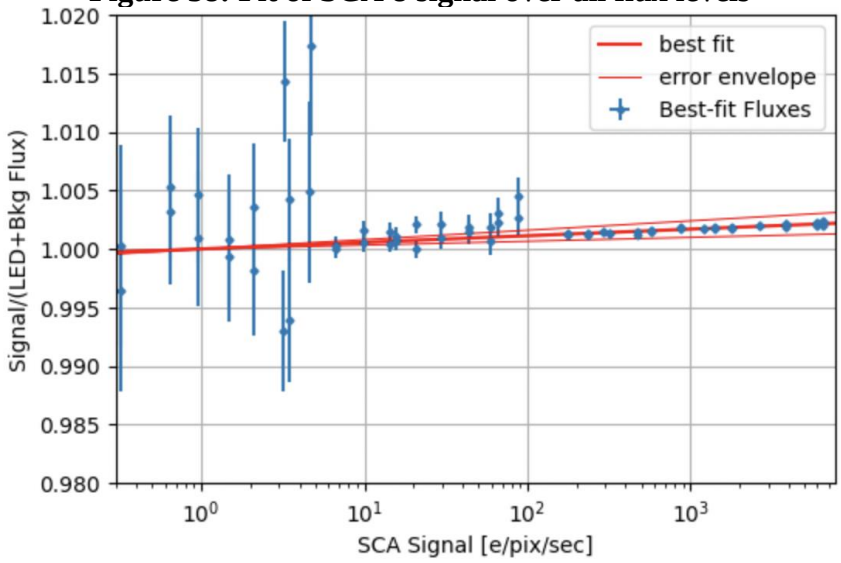

Those average count rates (a.k.a detector signal) are used for fitting a power-law model that describes the CRNL as:

$$F = s^{1-\alpha}$$

Where F is the LED flux, s is the superpixel signal (count rate), and α is due to the deviation caused by CRNL. The α extracted from the fit is then multiplied by $4.5 * \ln(10) \cong 10.3$ to obtain the FDNL over 4.5 decades of flux, shown in the plots below. The spread of the histogram in Figure 59 is dominated by the FDNL structure shown in Figure 60.

Figure 59: Histogram of Alpha for superpixels in SCA 8.

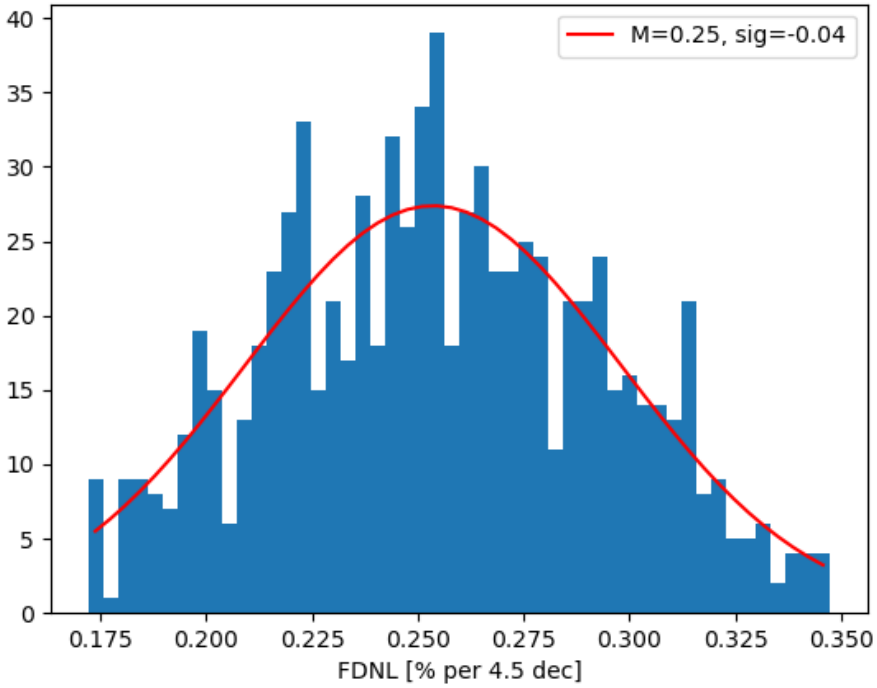

Figure 60: Pixel map of Alpha for superpixels in SCA 8.

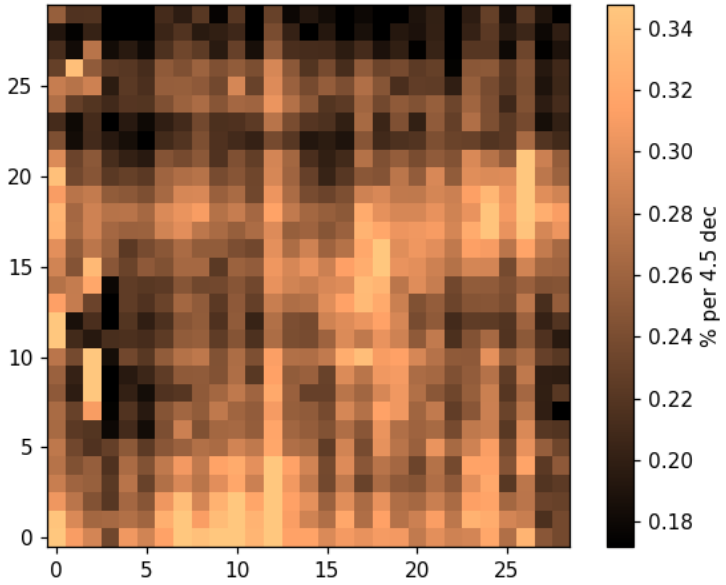

Thus far the FDNLs obtained for FPA detectors are small and usually less than 1% over 4.5 flux decades. The plan is to provide band-by-band FDNL maps on each detector to astronomers by the time the WFI is commissioned. The latest documentation on ground-based sRCS studies of FPA-detector FDNLs can be found in report RST-WFI-RPT-1815.

8.2.2 FDNL at the DCL

CRNL (also known as FDNL) was measured at the DCL at 95K for all detectors in the FPA except for 22081 (SCA 1) and 21115 (SCA 4). Flat field illumination was provided by an 880nm SLD (superluminescent diode) and a 1550nm SLD. The flux during this test ranged from 2000 e-/pixel/second to 60,000 e-/pixel/second. The nominal time per up-the-ramp frame was 2.83 seconds. To avoid saturating the pixels at the highest fluxes the detectors were run in “strip mode” where only the last 128 rows were read out in each frame which resulted in an effective frame time of 0.09 seconds. The following chart shows an example of the normalized ratio between the median detector signal and the respective monitoring photodiode signal at different flux levels.

Figure 61: FDNL measured at the DCL

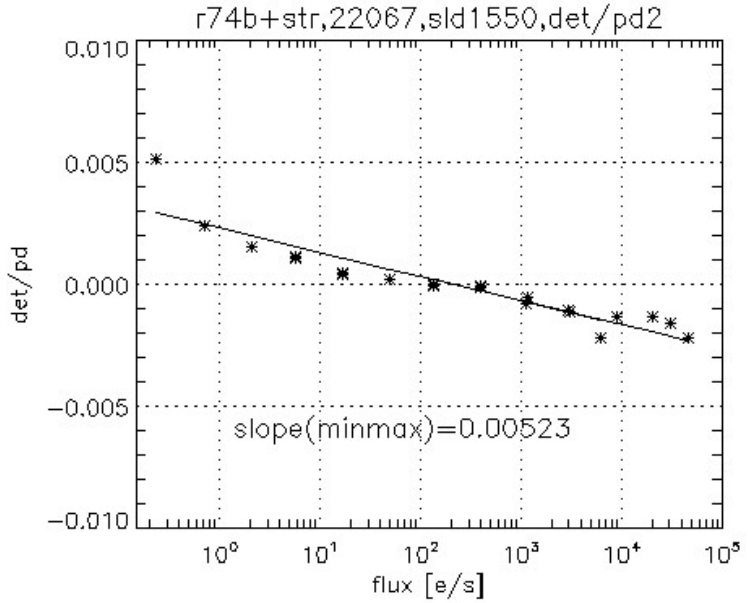

The following table shows the DCL results for the signal ratio vs. flux (percent per 4.5 decades) slopes calculated from 880nm data and 1550nm data. The analysis method used here was developed by Nils Odegard and bins detector image data into 32x32 superpixels, then calculates a Classical Nonlinearity correction using a 5-degree polynomial for all except the highest two flux levels. A linear fit of the CNL-corrected fluxes and photodiode-measured flux levels is then calculated, and the slopes are reported below.

Table 12: FDNL Slopes

		880nm		1550nm	
SCA #	SCA SN	Slope	Error	Slope	Error
1	22081	-	-	-	-
2	21815	0.22	0.07	-0.22	0.04
3	21946	0.14	0.06	-0.19	0.05
4	21115	-	-	-	-
5	21816	-0.01	0.1	-0.31	0.05
6	20663	0.46	0.11	0.05	0.12
7	22069	0.03	0.05	-0.12	0.07
8	21641	0.13	0.05	-0.73	0.03
9	21813	0.1	0.05	-0.18	0.05
10	22078	0.23	0.06	-0.26	0.03
11	21947	0.12	0.05	-0.23	0.03
12	20829	0.33	0.09	-0.03	0.04
13	22067	0.12	0.07	-0.2	0.03
14	21814	-0.22	0.04	0.05	0.05
15	21645	0.16	0.28	-0.49	0.08
16	21643	0.05	0.05	-0.24	0.03
17	21319	0.59	0.15	0.09	0.07
18	20833	0.99	0.23	0.45	0.27

9 ZERO TIME OFFSET

9.1 Intro

Linearity correction is dependent on the measured signal in each pixel accumulated in up-the-ramp exposures. The first frame in an exposure is the reset-read frame, where the pixel is reset at the beginning and accumulates signal until it is read out after the frame time duration. The reset-read frame is not usually included in analysis with the subsequent science frames, but the signal accumulated in the reset-read frame still contributes to the total pixel signal and should be included in linearity correction. The Zero Time Offset (ZTO) is a correction factor that can be used to account for the pixel value offset in the reset-read frame. The following steps outline how the ZTO may be calculated:

1) Read in and apply reference pixel correction to six science frames at the beginning of an illuminated exposure. Omit the reset-read frame and the first science frame, which can be unstable.
2) Fit a 2nd degree polynomial (quadratic function) to each pixel.
3) The ZTO is the extrapolated pixel value at the reset-read frame. Its value is then subtracted from each subsequent science frame.

Figure 62: Example of ZTO calculation.

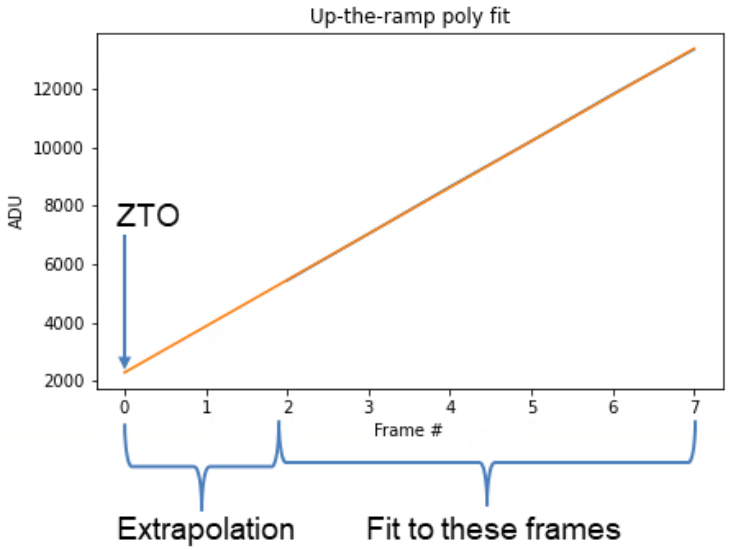

9.2 Illumination Dependent Pattern

A gradient pattern of alternating high-low pixel values in the SCA output channels for illuminated exposures is imprinted on the ZTO calculations and the first frames in an exposure. Subtracting the ZTO from frames within an exposure mitigates the effect of the pattern, which suggests that it is created by detector behavior within the reset-read frame. The amplitude of this pattern is illumination dependent and roughly scales linearly with flux. It is also clearly visible in the difference of reset-read frames for different flux levels. The direction of the gradient follows the output channel read direction, with brighter pixels at the beginning of the channel read and darker ones at the end. The gradient pattern does not appear in the reference pixels or the SCE

reference output channel. Analysis of the ZTO and the reset-read frames for data collected at different flux levels in the Talbot illuminator test setup also shows the gradient pattern.

Figure 63: Example of gradient pattern in ZTO

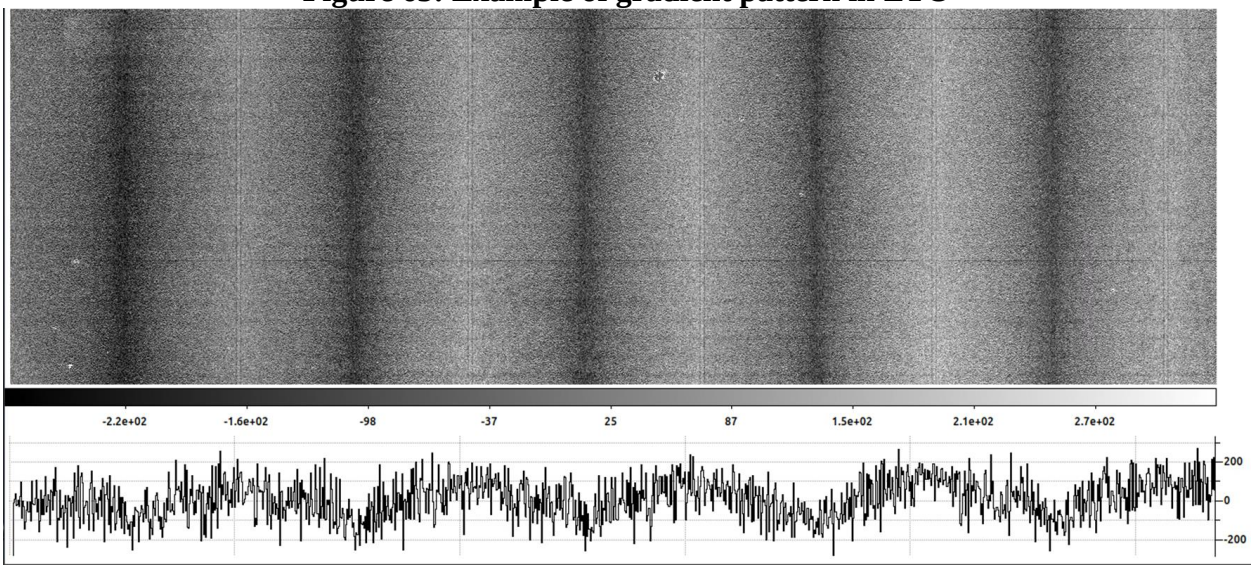

Figure 64: Gradient pattern in the difference of reset-read frames for high and low signal exposures with flat field data (left) and Talbot illuminator data (right)

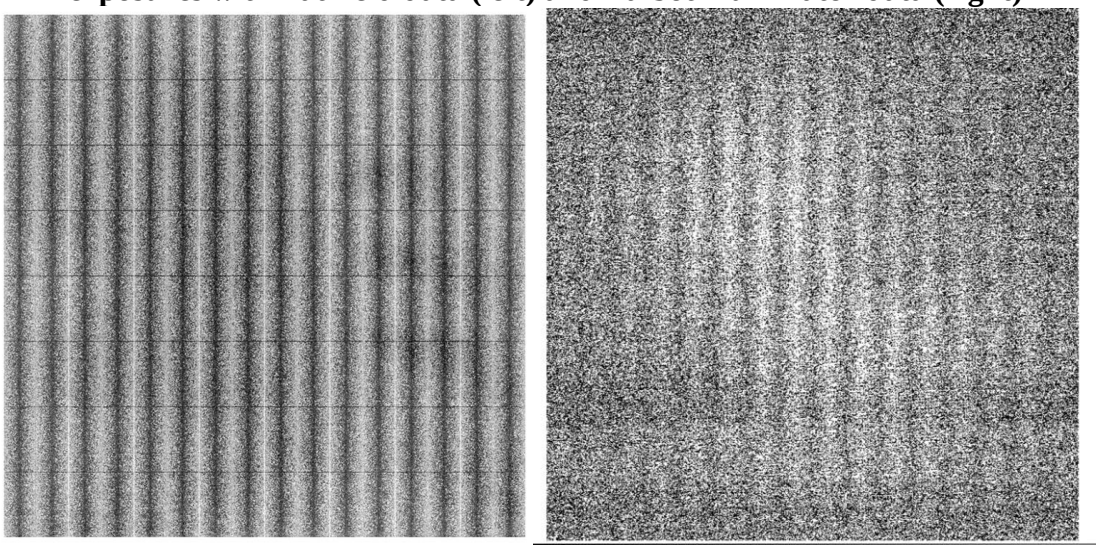

The cause of the ZTO pattern is under investigation. Efforts to mitigate the ZTO effects in the flight FPA are currently being explored.

9.3 Temperature Dependence

Temperature dependent behavior of the ZTO was found by calculating the ZTO using high flux linearity data collected during ColdOp4 (85K) and the Initial Performance Test (95K) of flight FPS TVAC. The pattern is visible in all detectors, though SCA 18 is dominated by temperature dependent horizontal structure in the ZTO.

These results were verified by comparing the ZTO in TVAC2 NomOps (89.5K) and HotQual (92.0K) science monitor data, but the amplitude of the pattern was less due to the smaller temperature difference.

Figure 65: Temperature dependent ZTO structure in Flight FPS TVAC

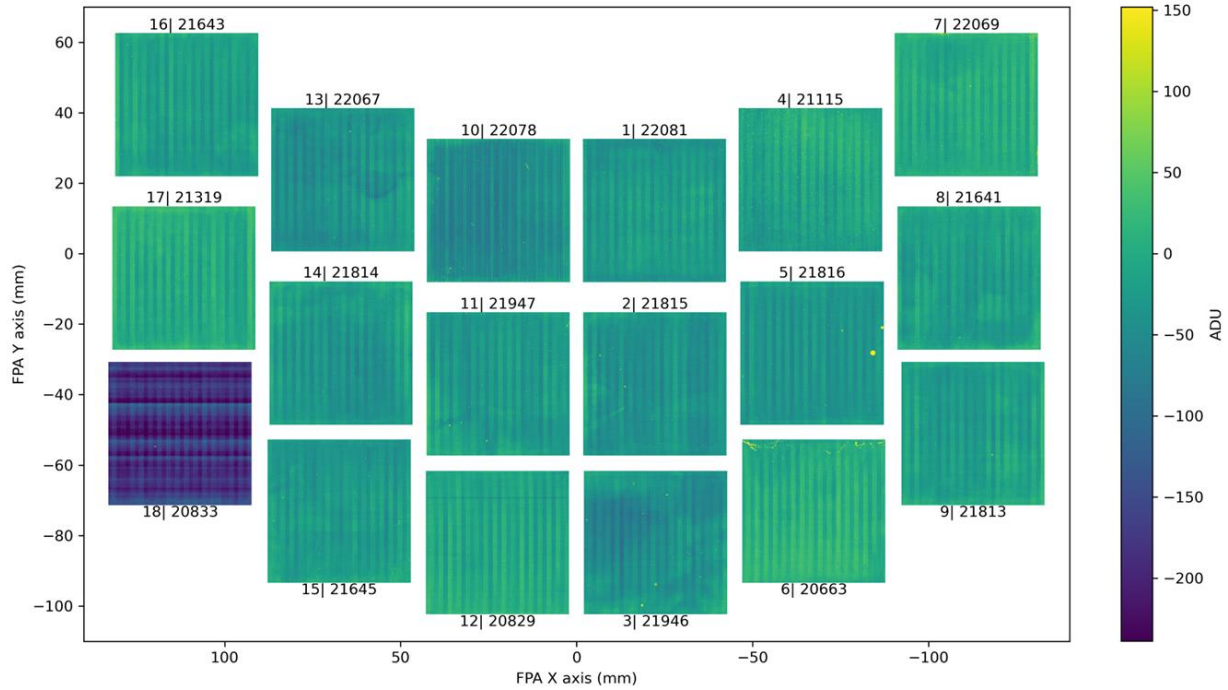

Unlike the illumination dependent pattern, the temperature dependent pattern does not have a gradient following the pixel read-out direction, and fades along the top and bottom edges of the SCAs. The median difference between output channels was 25 ADU for the 10K temperature difference in FPS TVAC, and 7 ADU for the 2.5K temperature difference in WFI TVAC2.

Figure 66: Zoomed-in view of temperature dependent ZTO pattern in center of SCA 1

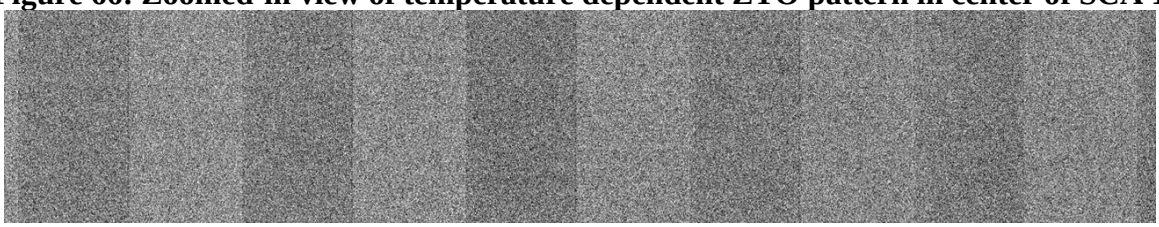

Figure 67: Zoomed-in view of pattern fading along bottom edge of SCA 1

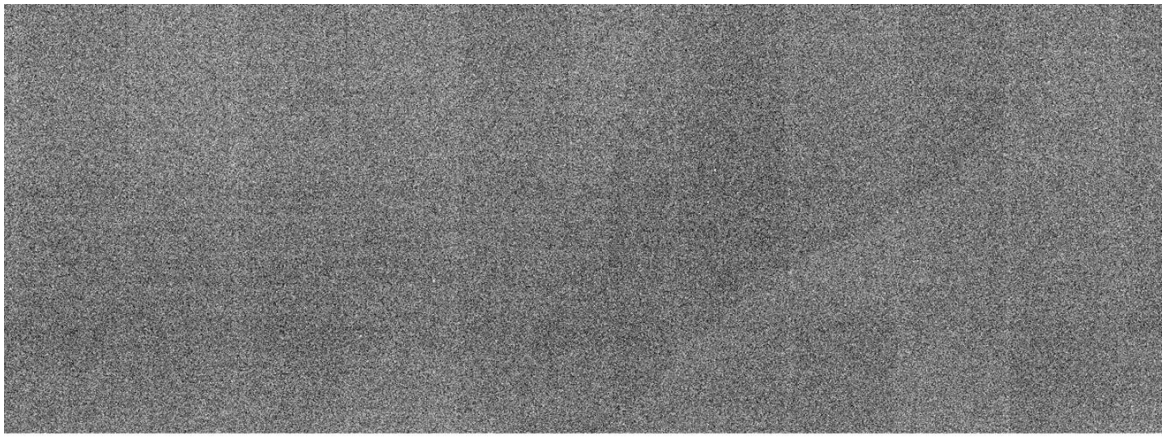

10 WELL DEPTH

10.1 Intro

The well depth of the detectors is calculated from exposures where the pixels are fully saturated with flat field illumination. This data was collected during the flight FPS TVAC initial performance test where the detectors were illuminated with 1600nm LEDs. Separate datasets for 1.0V and 0.5V bias voltages were acquired, though only 1.0V is expected to be flight-like. The first science frame in the exposure was subtracted from the other frames to correct for the pixel offset value, then a second-degree polynomial fit was calculated per pixel using science frames 2-6. The negative Y-intercept of the fit represented the amount of signal that was accumulated in the reset-read frame and first science frame. This Y-intercept value was then added back to the science frames. IPC-corrected photon transfer gain was calculated for each output channel of the SCAs and applied to reference pixel-corrected saturated frames to convert from ADUs to electrons. Since the classical nonlinearity correction is invalid for signal levels above 80ke-, no linearity correction was applied. Because of this the results here represent a conservative estimate of the well depth.

10.2 Histograms

The following plots show the distribution of accumulated signal in the last frame of saturated exposures along with the calculated Cumulative Density Function (CDF).

Figure 68: Well Depth Histograms

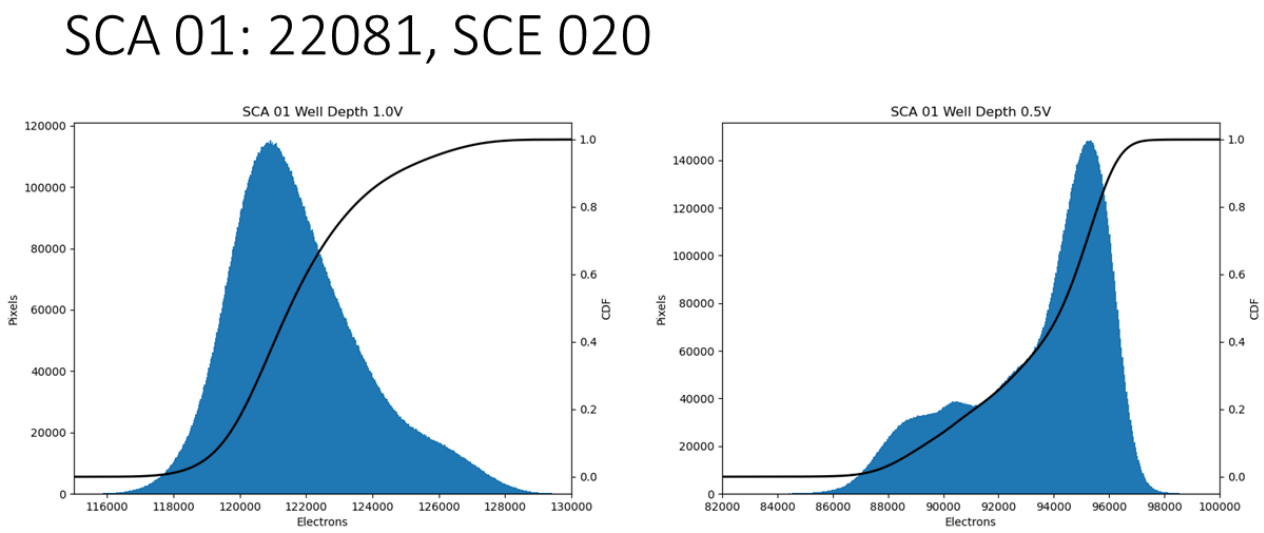

SCA 02: 21815, SCE 013

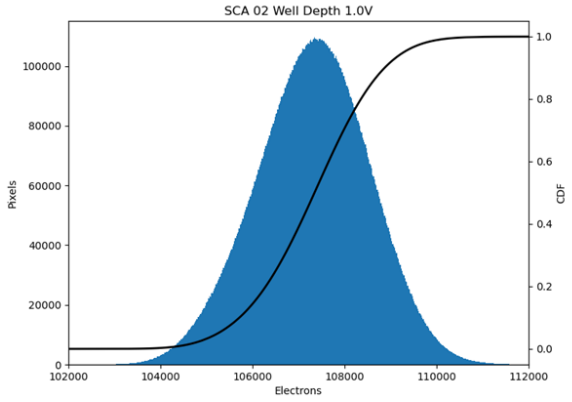

SCA 03: 21946, SCE 097

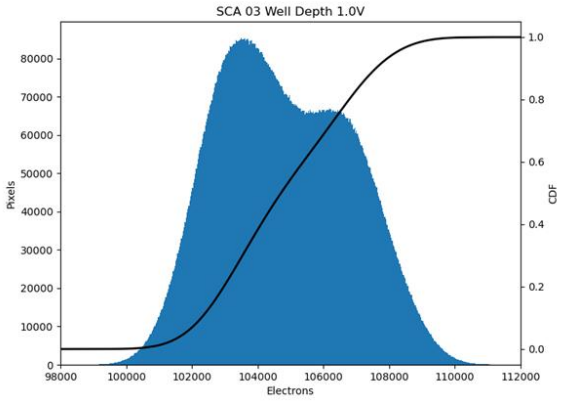

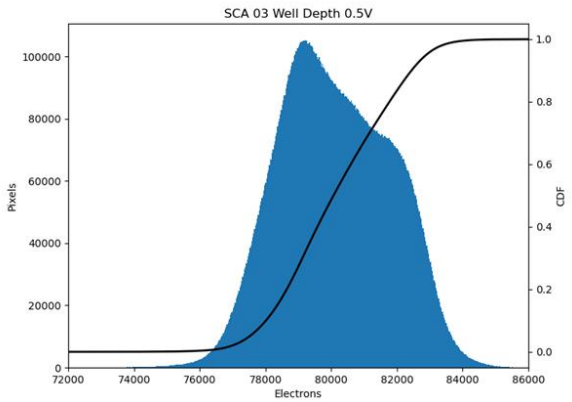

SCA 04: 21115, SCE 019

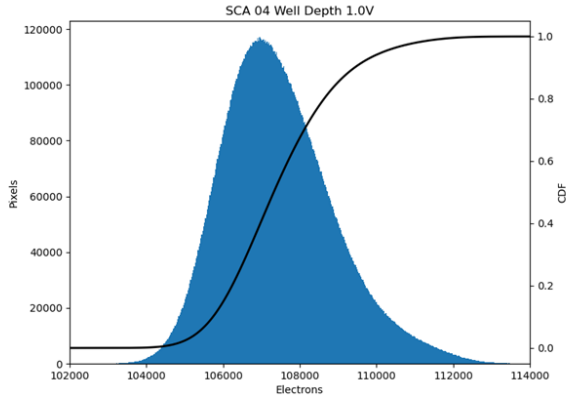

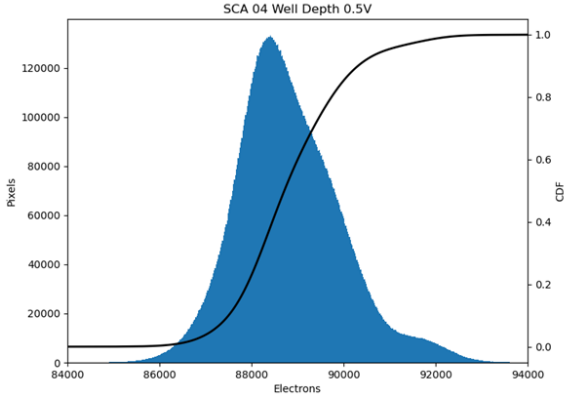

SCA 05: 21816, SCE 002

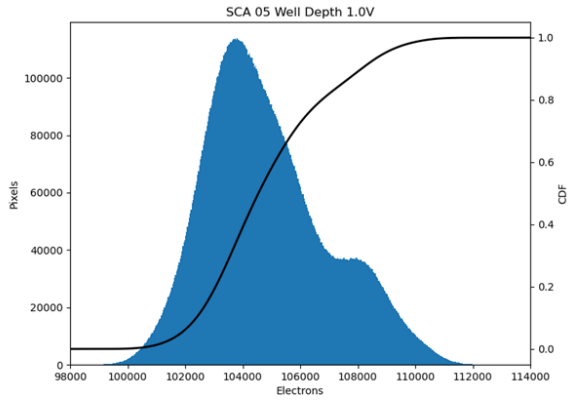

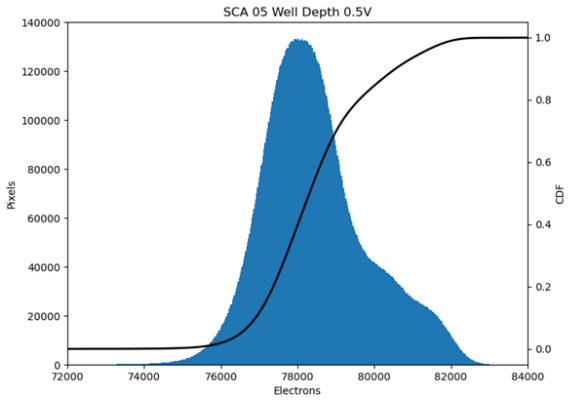

SCA 06: 20663, SCE 075

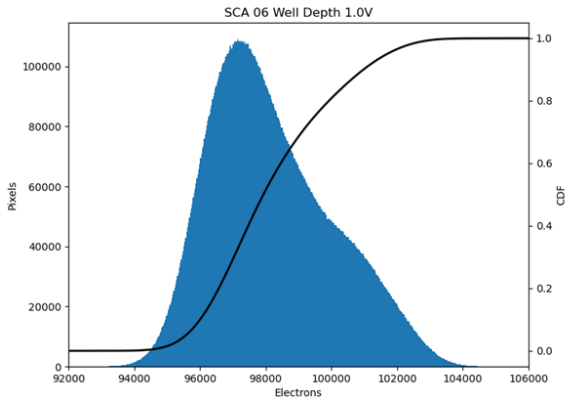

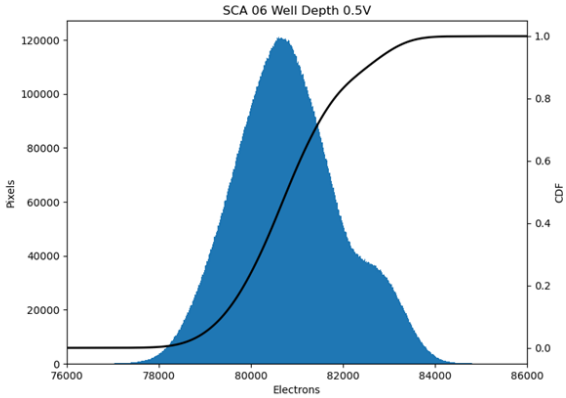

SCA 07: 22069, SCE 021

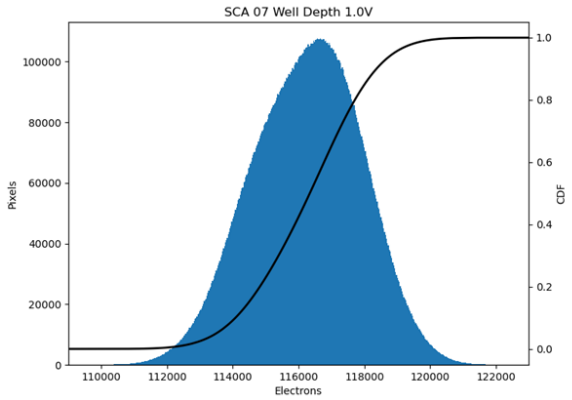

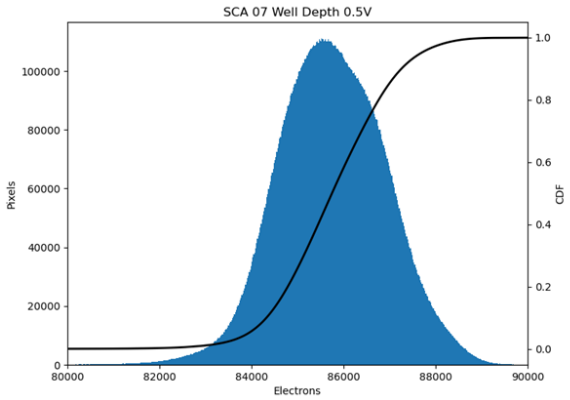

SCA 08: 21641, SCE 003

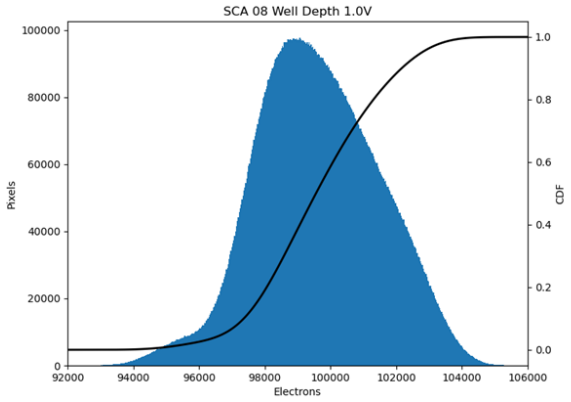

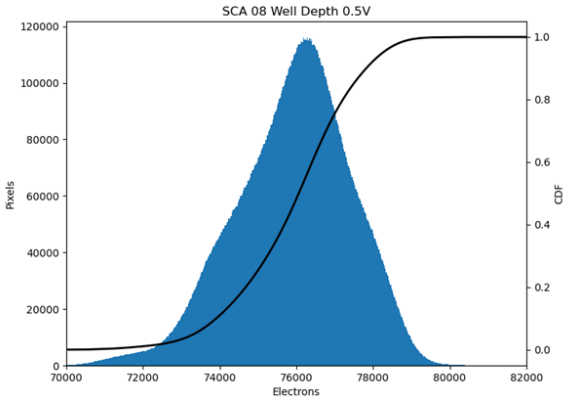

SCA 09: 21813, SCE 087

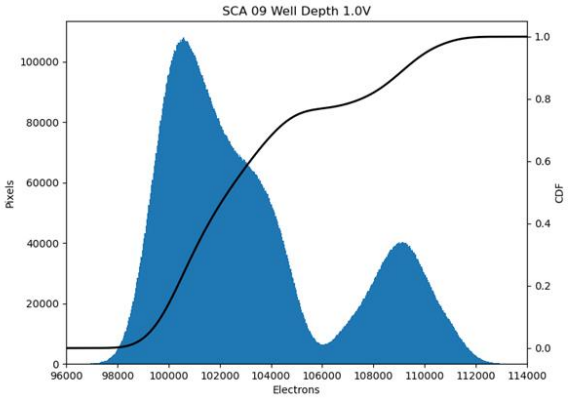

SCA 10: 22078, SCE 026

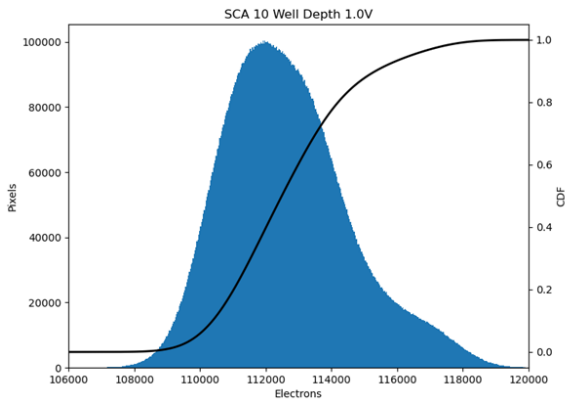

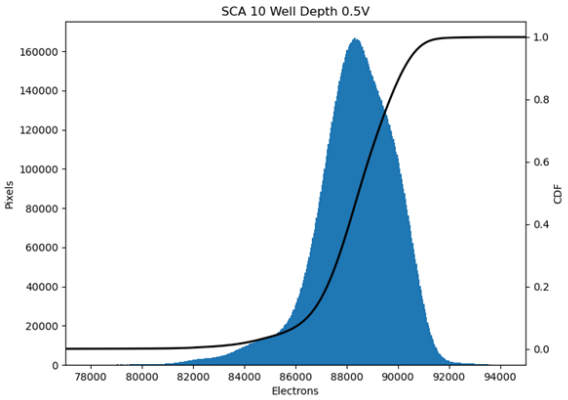

SCA 11: 21947, SCE 016

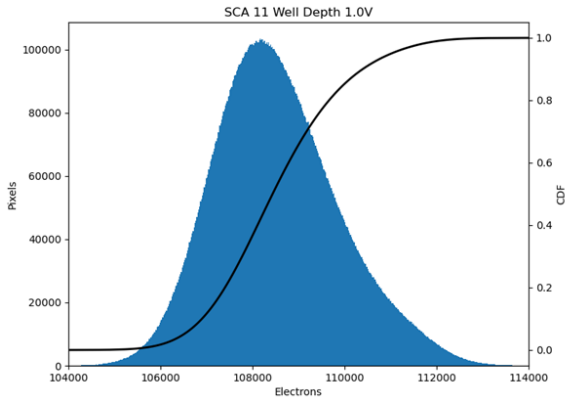

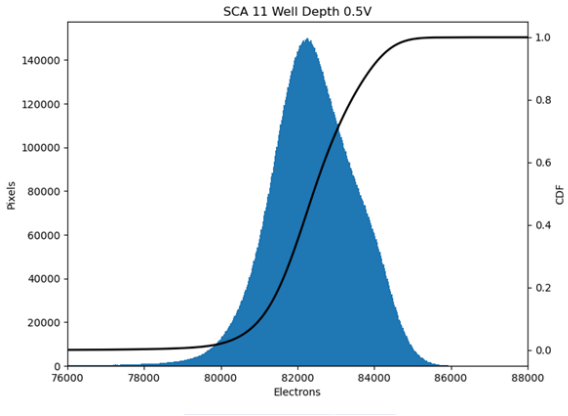

SCA 12: 20829, SCE 089

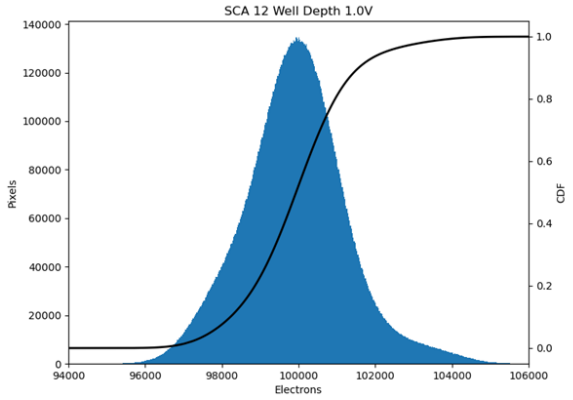

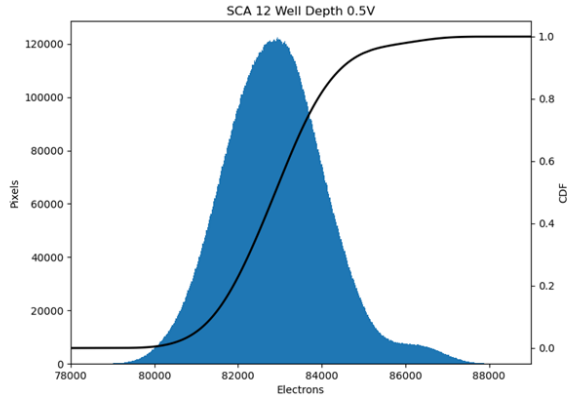

SCA 13: 22607, SCE 017

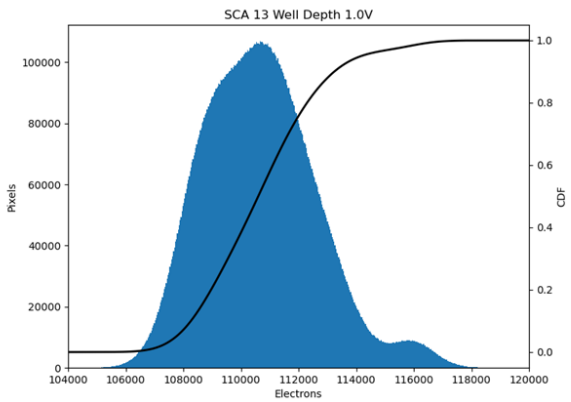

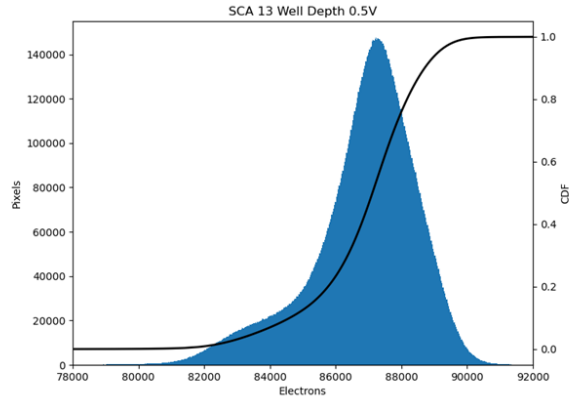

SCA 14: 21814, SCE 015

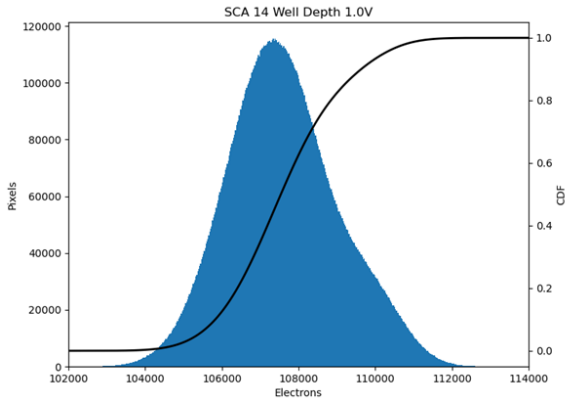

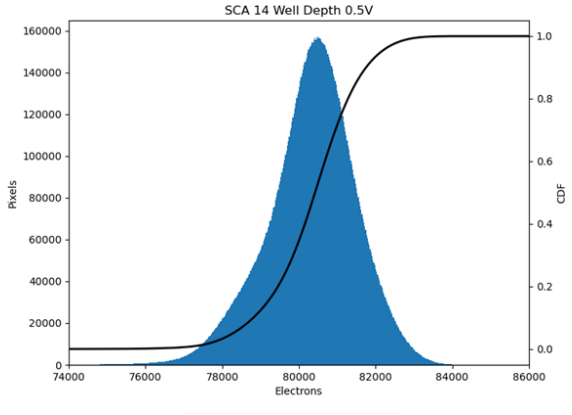

SCA 15: 21645, SCE 005

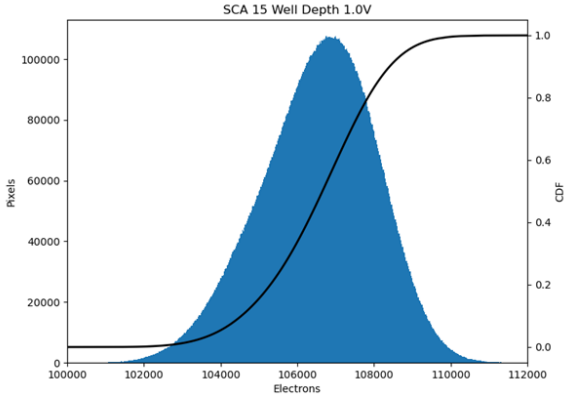

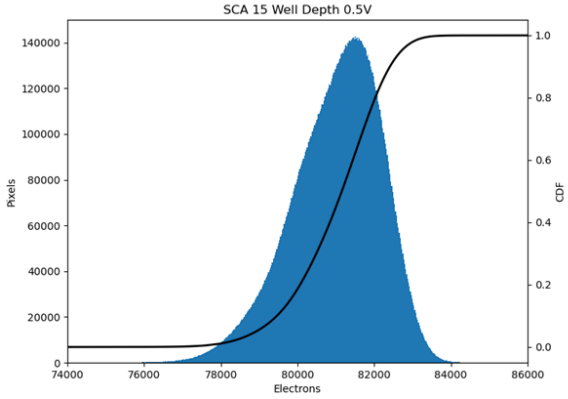

SCA 16: 21643, SCE 018

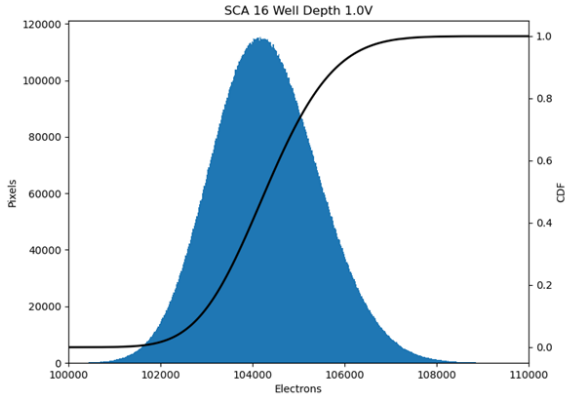

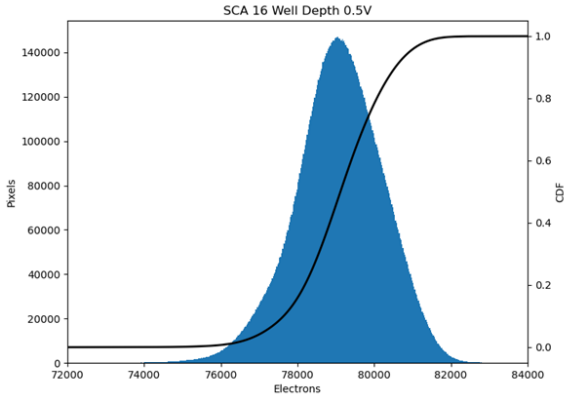

SCA 17: 21319, SCE 012

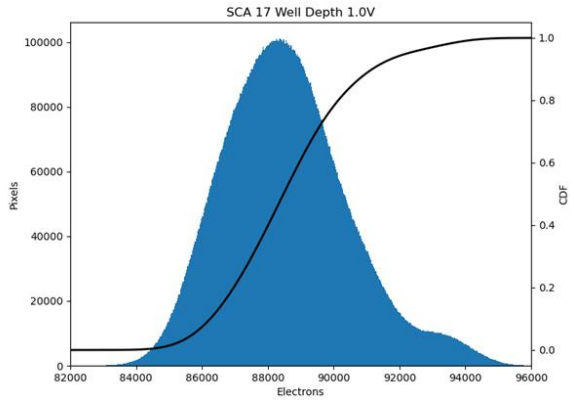

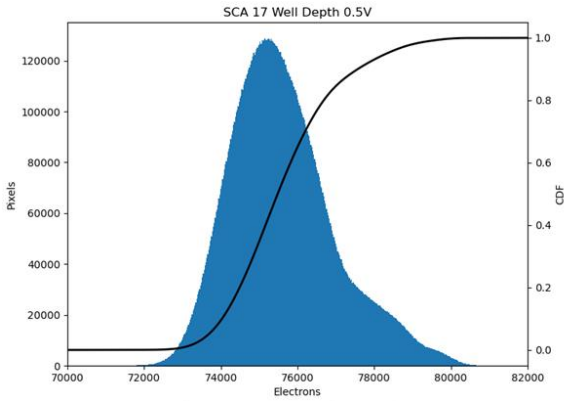

SCA 18: 20833, SCE 099

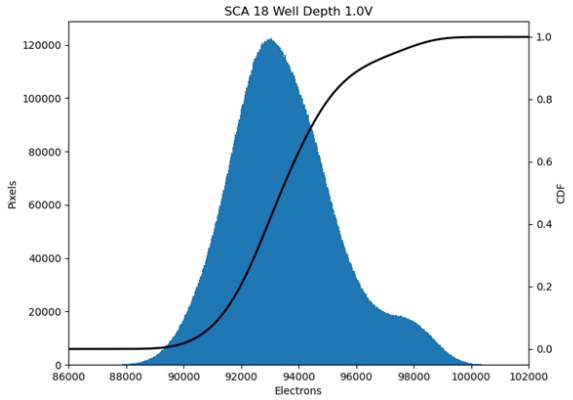

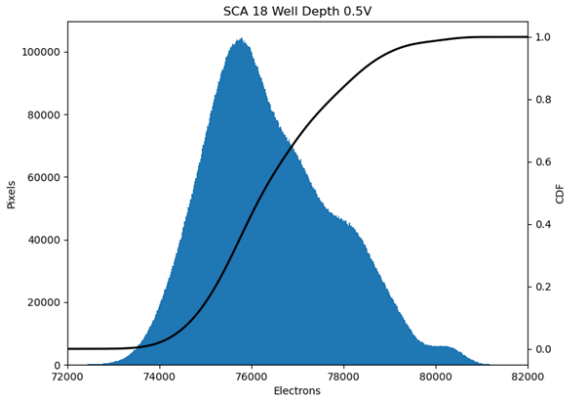

10.3 Summary

Table 13: Statistics for the well depth of each SCA in units of electrons

SCA #	Median well depth	Stdev last frame	Well depth at CDF 0.0005	Well depth at CDF 0.005	Well depth at CDF 0.05	Well depth at CDF 0.1	Well depth at CDF 0.9	Well depth at CDF 0.95
1	121464	3643	116428	117531	118940	119475	124715	125853
2	107331	3337	103343	104171	105246	105712	108870	109286
3	104650	4481	99594	100575	101770	102282	107595	108193
4	107301	2361	103531	104392	105345	105734	109429	110168
5	104499	4148	99339	100504	101832	102383	108129	108933
6	97890	2970	93697	94558	95571	96002	100976	101696
7	116303	8154	16760	111967	113484	114072	118370	118895
8	99518	2521	93445	94627	96715	97358	102164	102768
9	102203	4855	97455	98244	99249	99708	109268	110074
10	112457	2446	107683	108703	109891	110381	115339	116411
11	108418	3421	104660	105497	106499	106900	110395	111017

12	99919	2057	95858	96594	97701	98222	101569	102240
13	110562	3974	105635	106582	107752	108262	113240	114177
14	107517	4223	103148	104176	105354	105826	109634	110225
15	106634	2339	101563	102514	103938	104540	108406	108856
16	104260	1890	100831	101549	102482	102859	105826	106284
17	88436	2809	83667	84526	85717	86250	91172	92224
18	93337	4462	88223	89302	90671	91255	96209	97388

Figure 69: Estimated well depth per pixel for the detectors in the FPA.

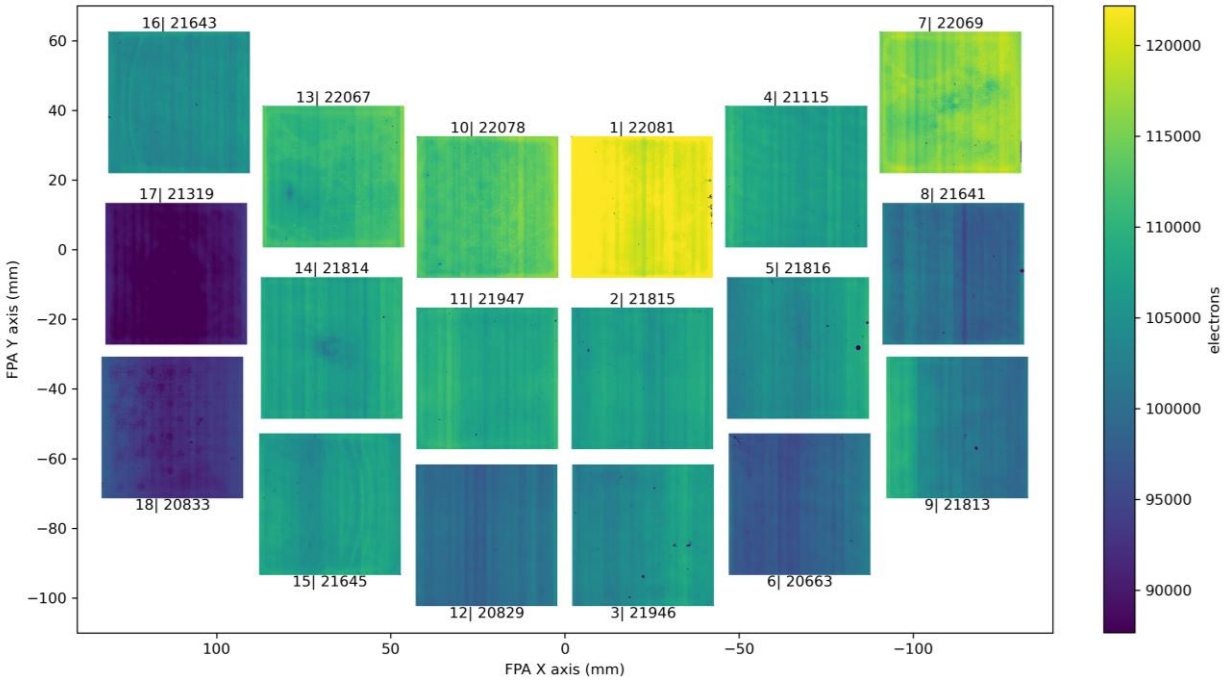

11 PERSISTENCE

11.1 DCL Acceptance Test Description

Persistence in the flight detectors was measured during the DCL Acceptance Tests and as a by-product of the WFI TVAC tests. The DCL acceptance tests measured persistence in two ways: 1) Illuminating the detector with different flux levels and analyzing the persistence during the first 10 minutes after illumination, 2) illuminating the detector with 300 ke- and analyzing persistence decay over the course of several hours. For both kinds of tests 10-minute-long exposures were used and the detectors were exposed to light during the last 440-540 seconds of the first exposure. The diagram below illustrates the illumination/exposure scheme for DCL Acceptance Testing. Data analysis for persistence is performed by calculating e-/s signal per pixel in the dark exposures after illumination, subtracting out signal from dark current.

Figure 70: Scheme for DCL persistence data acquisition

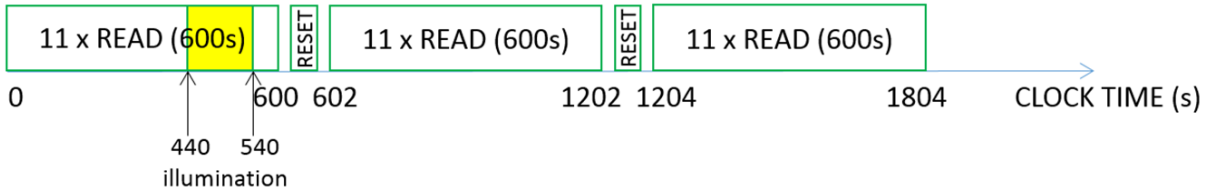

Persistence per pixel was calculated at the DCL for two levels of illumination: “low” level with 50 ke- (500 e-/s) and “high” level illumination with 300 ke- (3000 e-/s). The reported excess dark current per pixel represents the persistence in the first 10-minute-long dark exposure after illumination.

11.2 WFI TVAC1 and TVAC2 Description

Persistence was measured during the WFI TVAC tests as a byproduct of the OTP00636_SciMonDark test. Since the illumination level was changed from 86 ke- (500 e-/s) in TVAC1 to 155ke- (900 e-/s) in TVAC2 the results from the two WFI TVAC tests are not directly comparable to each other or to the DCL Acceptance Tests. The timing of exposures in the WFI TVAC tests was also different from DCL testing, with a sequence of either 3 or 10 170-second duration exposures in the dark following illuminated exposures of the same length. The data analysis method for both WFI TVAC tests was consistent and matched the method used by the DCL: calculate the signal per pixel in electrons/second for the first dark exposure after illumination, subtracting out dark current and instrument background contribution.

11.3 Persistence Modeling

During WFI TVAC2 10 dark exposures were collected after illumination during the science monitor test at the HotQual plateau (92K) and the NomOps plateau (89.5K). These 10 dark exposures captured the persistence decay in the detectors following exposures of 56 frames where the SCAs were exposed to 900 e-/s illumination for a total of 159 ke-. The median persistence was fit to an exponential function in this form:

$$a * \exp(-b * x) + d * \exp(-e * x) + c$$

Where x is the time in seconds since the end of the illuminated exposure. The measured persistence data had good agreement with the exponential fit. The plots below show examples of the measured median persistence values in orange and the modeled values in blue.

Figure 71: SCA 4 Persistence Decay

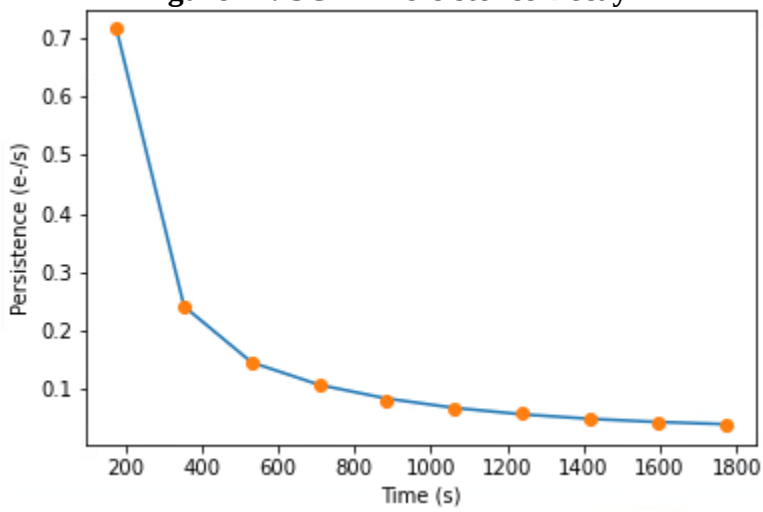

Figure 72: SCA 15 Persistence Decay

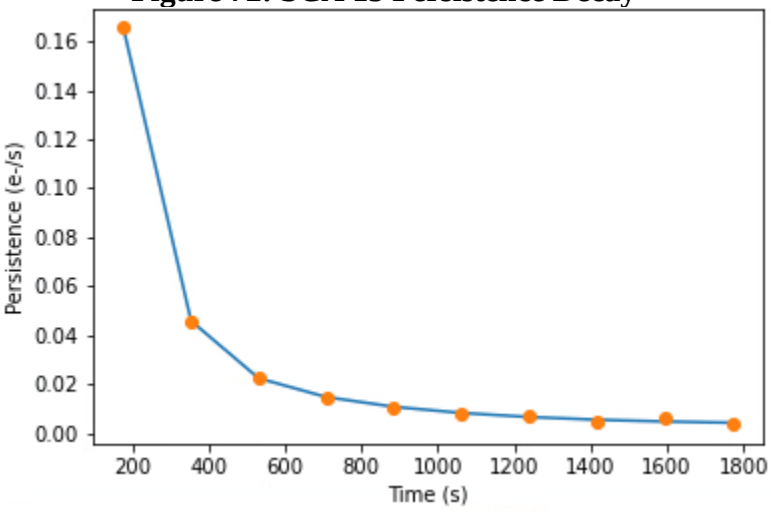

More information on modeling the persistence behavior and the coefficients of the fit are available on TDMS in RST-WFI-TN-0597.

11.4 Persistence Mosaics

See following pages for summary Figures showing persistence in the flight WFI detectors.

Figure 73: DCL low level persistence (50 ke-, 95K)

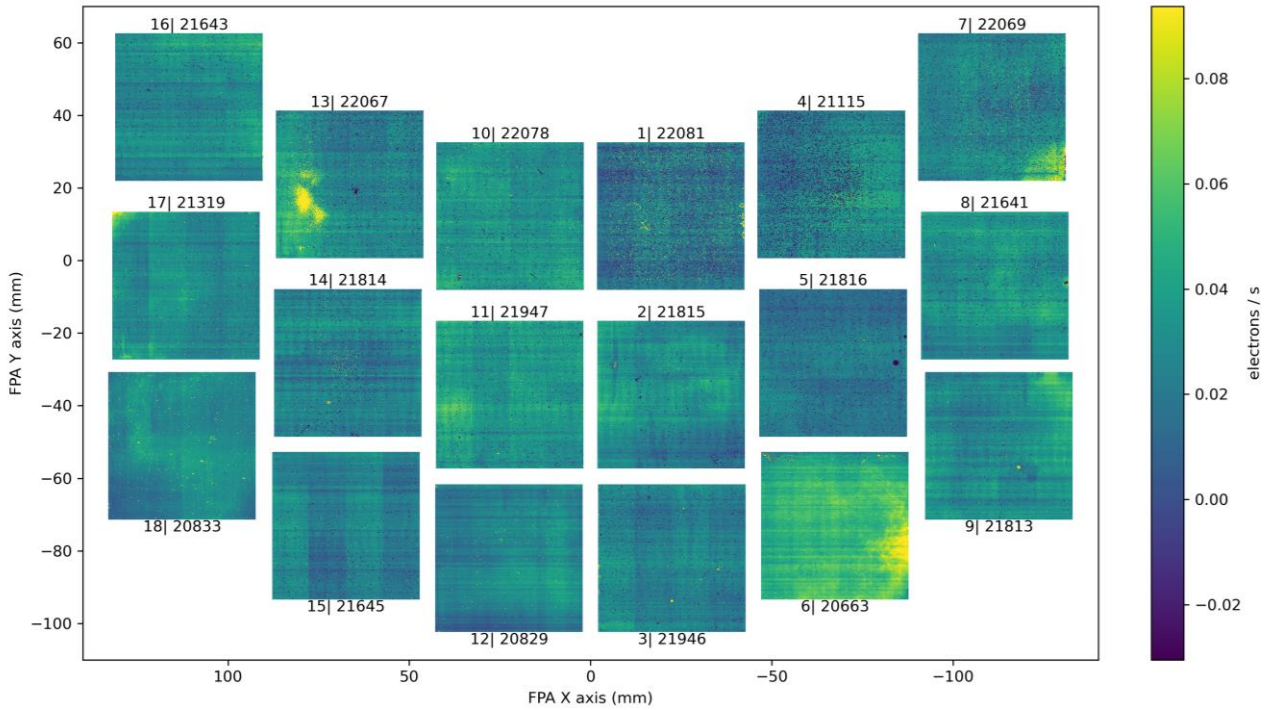

Figure 74: DCL high level persistence (300ke-, 95K)

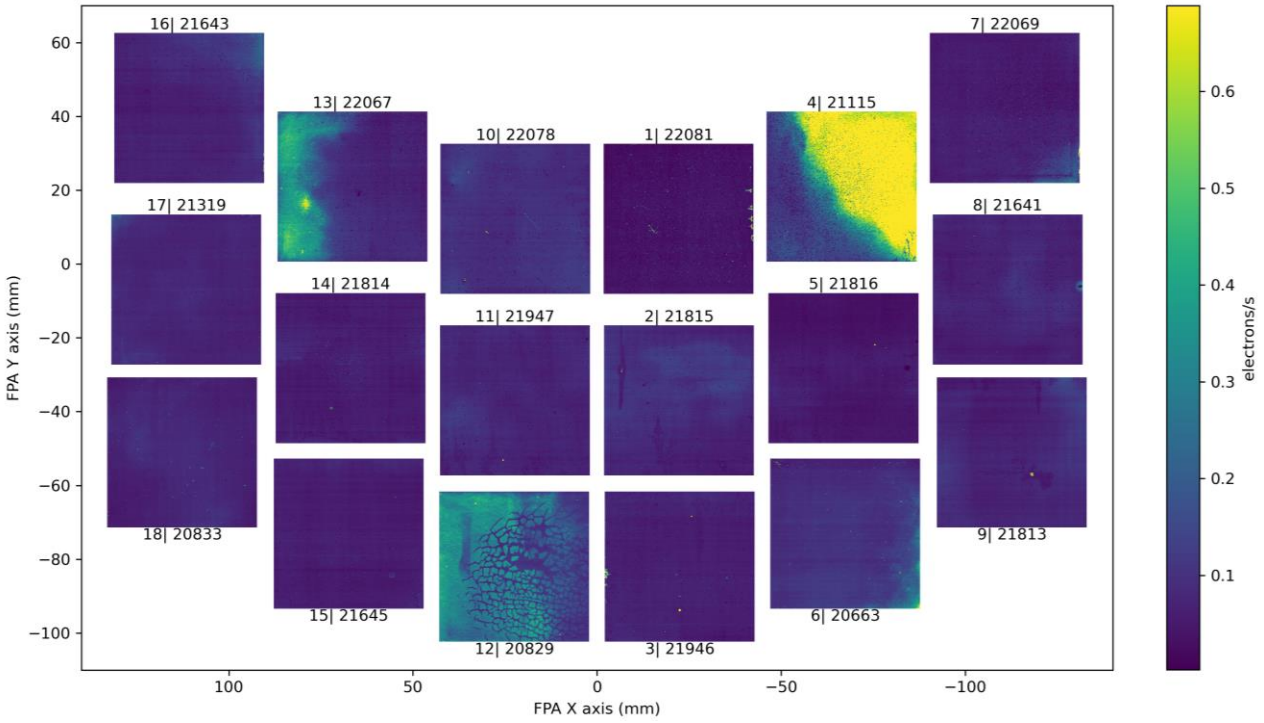

Figure 75: Persistence in WFI TVAC1 (86 ke-, 88.8K)

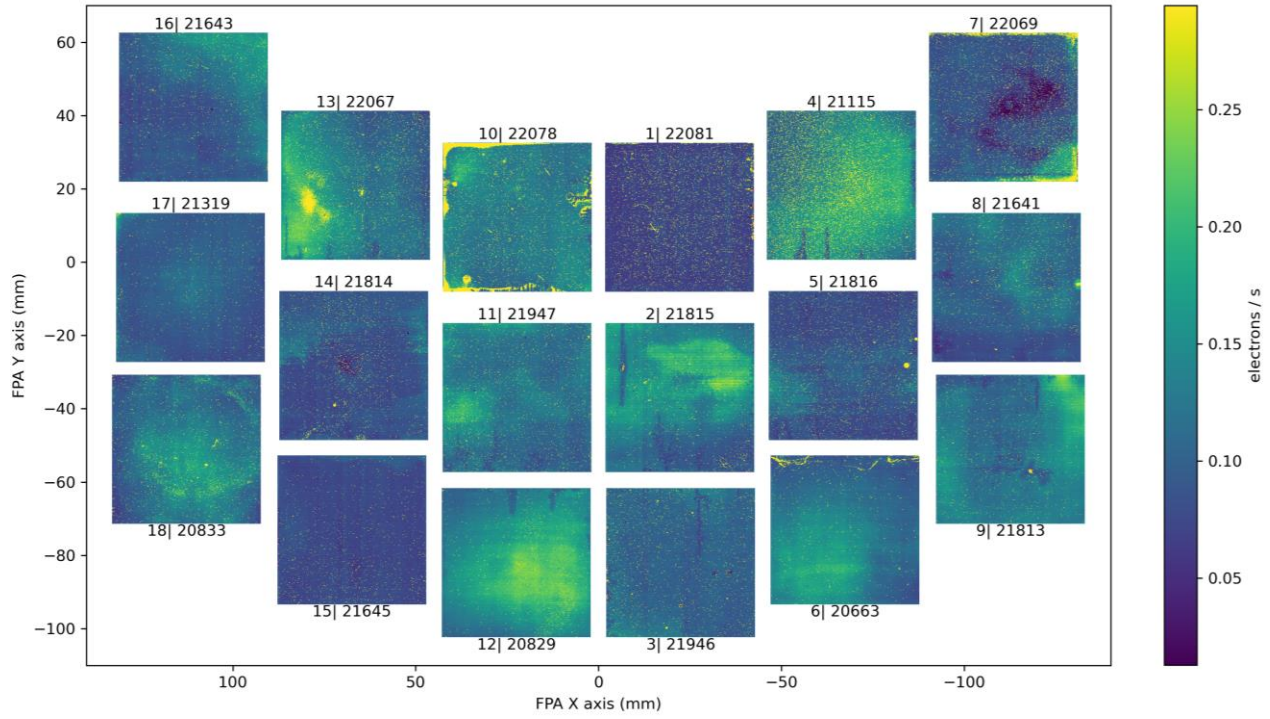

Figure 76: Persistence in WFI TVAC2 (155ke-, 89.5K)

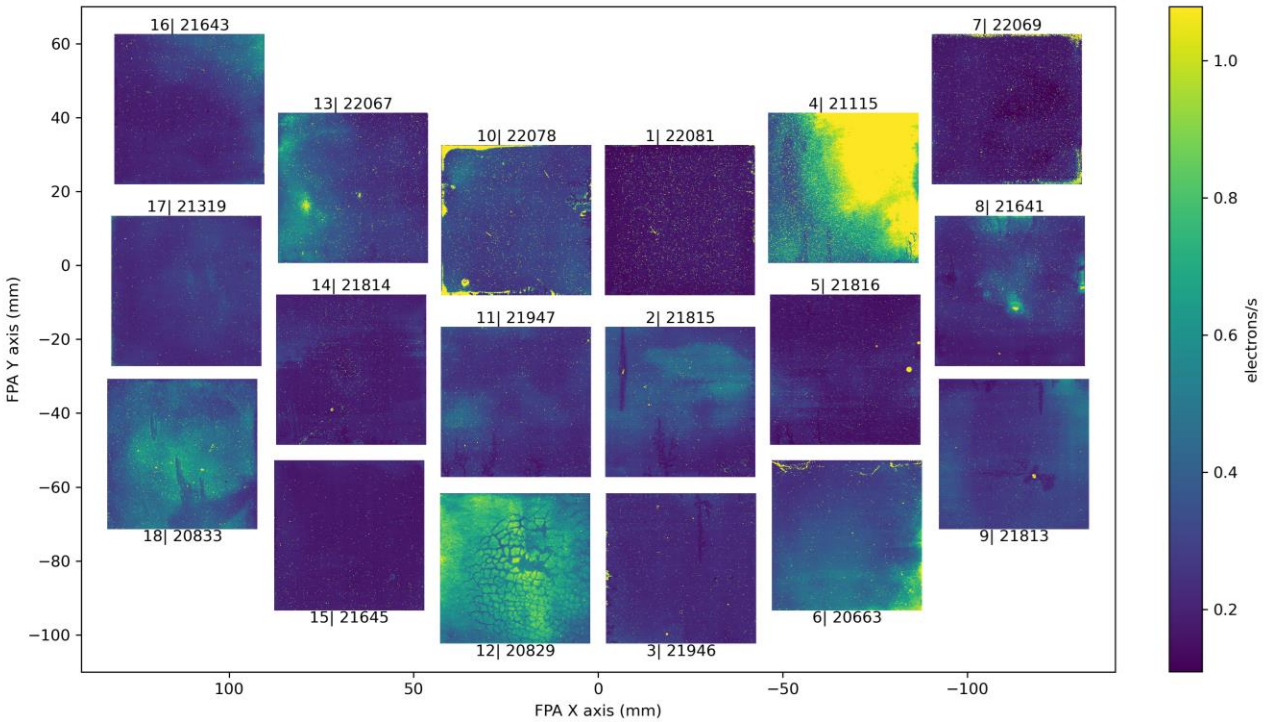

11.5 Persistence: SCA 4, 21115

High persistence in 21115 triggered by high intensity illumination initially disqualified it from being included in the flight unit. However, this SCA was ultimately chosen to replace SCA

22073 in location 4 on the flight FPA following the direction of the DD-ARB. Its high intensity persistence behavior was observed again in WFI TVAC2, but because the test parameters were different from the initial DCL acceptance test it is difficult to say whether the persistence in this detector has changed since it was first measured in 2020.

11.6 Persistence: SCA 6, 20663

SCA 20663 in location 6 on the FPA has curved linear features along the top edge of the active area which are characterized by high total noise, dark current, and persistence. These features have been present since DCL acceptance testing and their dark current and total noise performance continued to worsen through WFI TVAC testing.

11.7 Persistence: SCA 7, 22069

SCA 22069 in location 7 of the FPA is characterized by an inverse S-shaped pattern of low persistence in the center of the active area. This area also has a high residual when the Classical Nonlinearity correction is applied.

11.8 Persistence: SCA 8, 21641

During WFI TVAC2 new areas of elevated persistence were observed in SCA 21641 in the center and along the edges of the array. These features were not previously seen in DCL, FPS, or WFI TVAC1 testing, and had elevated persistence of about 0.75 e-/s higher than the surrounding pixels. In TVAC2 these features were not present in the dark current data for ColdQual and NomOps (89.5K) but were faintly visible in the dark current at HotQual (92K). The temperature dependent elevated signal was small but visible and is unique to the new feature in SCA 8. Other high persistence areas in other SCAs were not elevated. The overall dark current performance of this detector has changed little overall since FPS testing. The bright feature in the red box in the figure below is centered at approximately X=2186, Y=2543. Prior to DCL acceptance testing this SCA was refurbished (its rigid-flex cable was replaced) by Teledyne Imaging Systems (TIS) because it had a non-functional output channel in the area where the bright central feature currently is.

Figure 77: Right: Persistence in WFI TVAC2 for SCA 8. Left: Zoom-in on red box area.

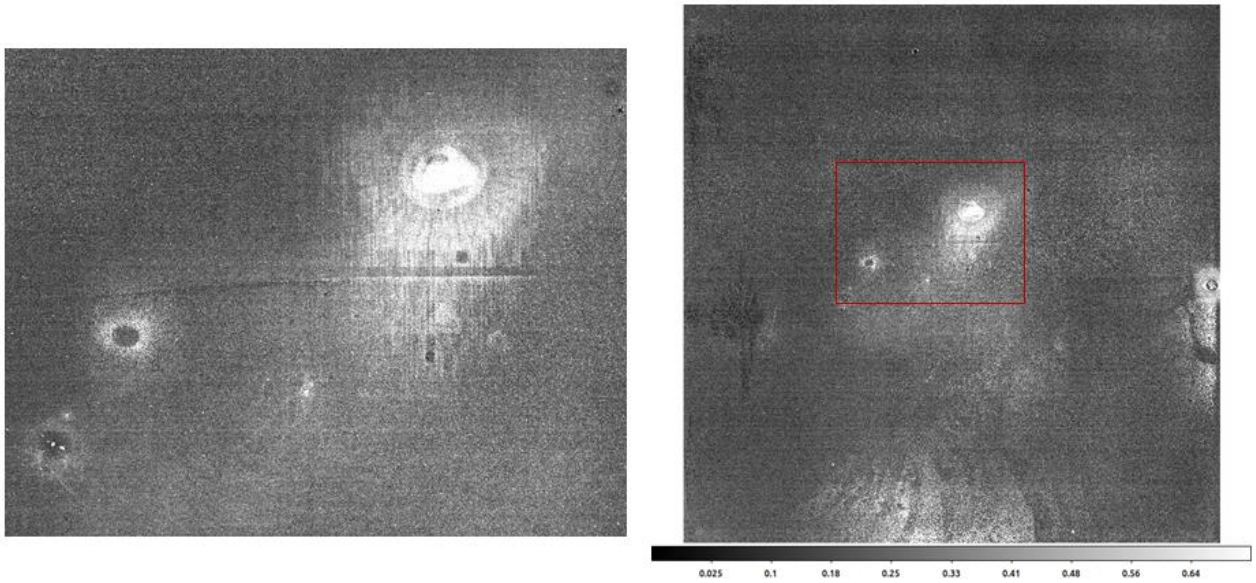

During WFI TVAC2 the new regions of elevated persistence were characterized by collecting more dark exposures during the science monitor test to measure the persistence decay. 10 dark exposures instead of 3 were collected after illumination with the sRCS band 6 LED. The median persistence of the central pixels in the bright spot highlighted in Figure 77 is plotted in the graph below.

Figure 78: Decay of SCA 8 bright spot persistence in WFI TVAC2

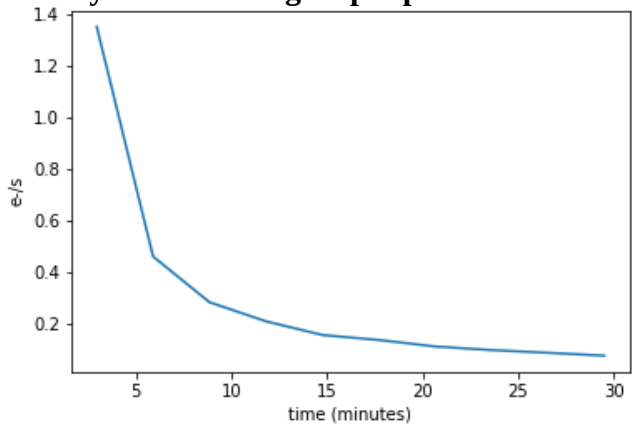

11.9 Persistence: SCA 10, 22078

After DCL acceptance testing SCA 22078 developed regions of high persistence around the edges of the active area that were first observed during semiflight FPS TVAC. Although persistence was not directly measured in FPS testing, the pattern of degradation was visible in the crosstalk data. No suitable replacement for this detector was identified so it was not replaced following the DD-ARB.

11.10 Persistence: SCA 12, 20829

The persistence in 20829, SCA 12 is characterized by a “cracked earth” pattern that is visible in the high illumination persistence response. The DCL first observed it during their test with 300 ke- signal, and it was observed again during WFI TVAC2 with 155 ke- signal.

11.11 Persistence: SCA 13, 22067

SCA 13, 22067 has a region of elevated persistence that activates at both high and low levels of illumination. This spot was visible in the dark current data collected during the WFI TVAC2 NomOps plateau, suggesting that persistence was activated during the time when this data was acquired.

Figure 79: Dark current in SCA 13 with high persistence region highlighted

11.12 Bright Star Persistence Observations

Detector persistence induced by a bright point source (as opposed to flat field illumination) is of interest because astronomical targets resemble point sources. Data were collected during WFI TVAC2 using the SORC (Stimulus of Ray Cones) to illuminate several SCAs with point sources of varying brightness. Several exposures in dark conditions were acquired before and after illumination for background subtraction purposes. SORC illumination simulated bright stars from magnitude 18 (dimmest) to magnitude 4 (brightest).

Figure 80: Bright star persistence illumination levels and targets.

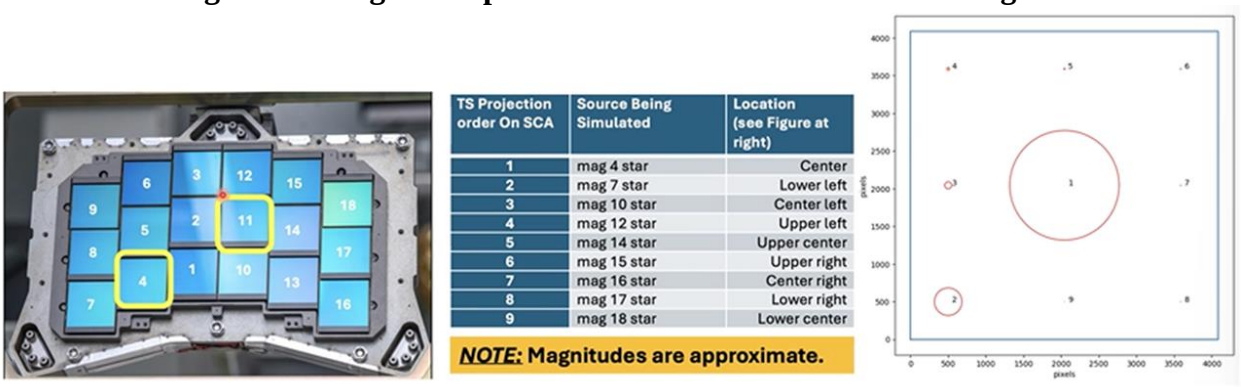

TS Projection order On SCA	Source Being Simulated	Location (see Figure at right)
1	mag 4 star	Center
2	mag 7 star	Lower left
3	mag 10 star	Center left
4	mag 12 star	Upper left
5	mag 14 star	Upper center
6	mag 15 star	Upper right
7	mag 16 star	Center right
8	mag 17 star	Lower right
9	mag 18 star	Lower center

NOTE: **Magnitudes are approximate.**

Figure 81: Zoomed-in view of frame 56 of Mag 4 illuminated exposure on SCA 4

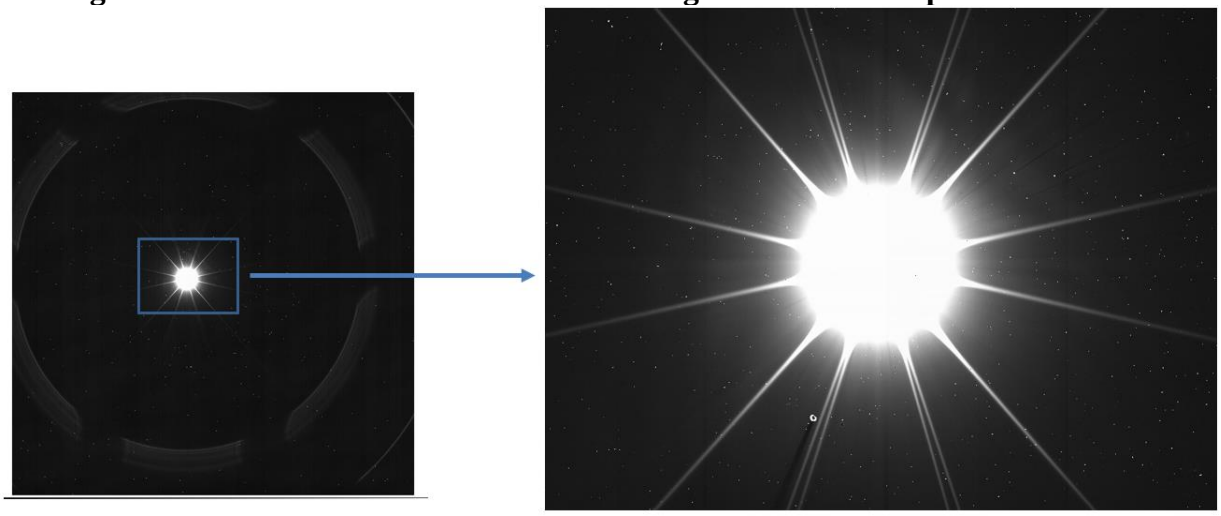

Some features within the magnitude 4 PSF (Point Spread Function) appear to cast shadows away from the center of the point source. It is theorized that the extremely high signal on the center pixels generates enough charge carriers such that a sufficient amount undergo radiative recombination in the detector material. This radiative recombination generates light close to the cut-off wavelength of the detector material that travels through the detector material and causes physical defects to cast shadows.

The region of interest for persistence calculation is shown in the Figure below. Dark current and instrument background from the pre-illumination dark images was calculated and subtracted from the post-illumination dark images to find the persistence. The two brightest spots in the

dark map are caused by light leaks from SORC illumination fibers that were left open during data collection.

Figure 82: Region of interest for persistence calculation and its pre-test background

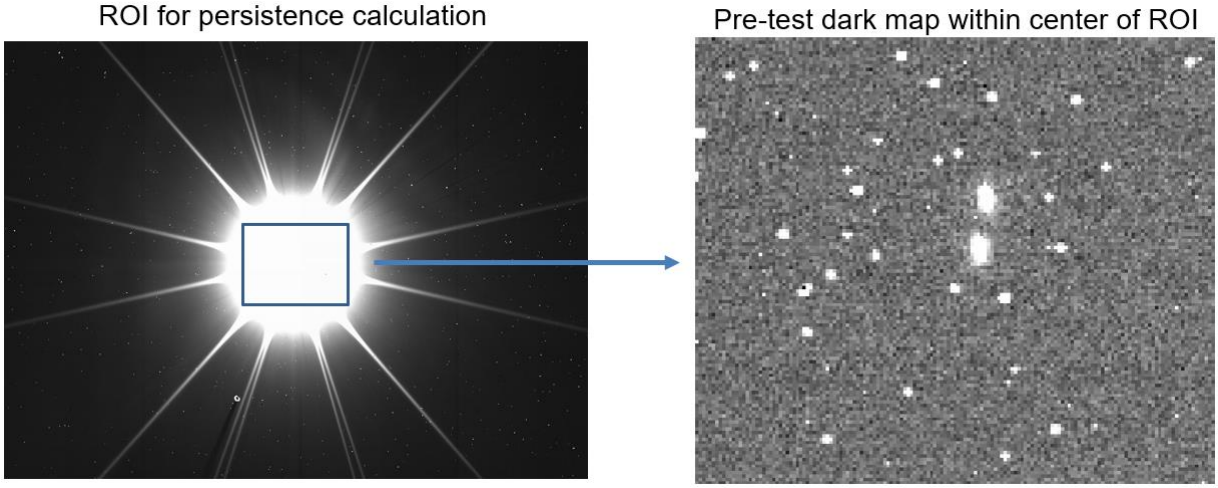

Each exposure was 56 frames, or about 3 minutes long. Despite the extremely high signal the persistence within the region of interest dropped significantly after about 20 minutes post-illumination. For reference, the DCL measured high level persistence (signal of 300 ke-) of 0.36 e-/s within 10 minutes of illumination within this same area.

Figure 83: Persistence in the SCA 4, Mag 4 Region of Interest

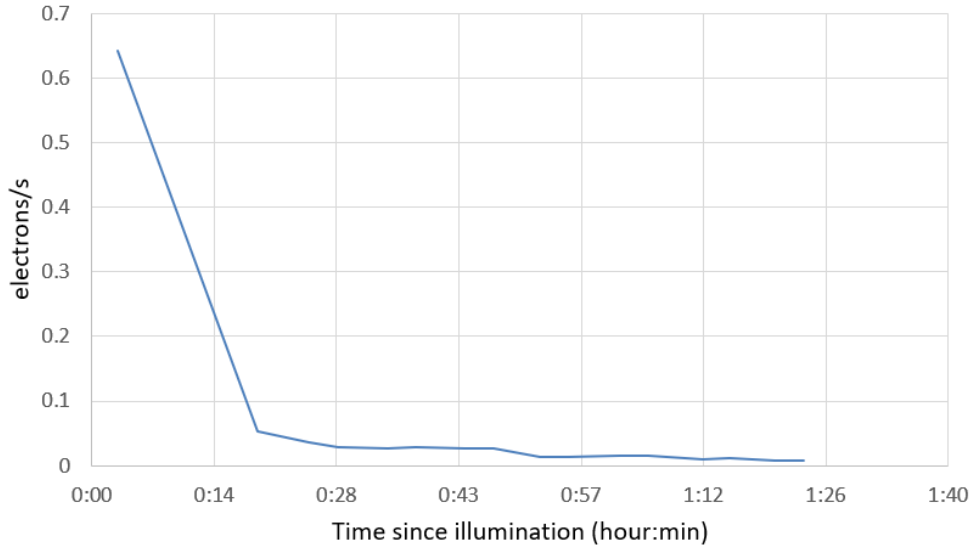

The persistence behavior for the full suit of simulated point sources is ongoing and will be used to better understand expectations for flight observations of sources with a wide variety of fluxes.

12 QUANTUM EFFICIENCY

12.1 Test Description

Quantum Efficiency (QE) is the percentage of photons that interact with the detector material to generate electrons which are then read out as signal. QE was measured during DCL acceptance testing at 95K with a 1.0V bias voltage as a function of wavelength from 480-2700nm. During this test the detectors are illuminated by a quartz tungsten halogen lamp whose light goes through a 6-position order sorting filter wheel to a monochromator with selectable holographic gratings. From the monochromator the light passes through the sapphire window of the cryostat into a cold (100K) integrating sphere and then to the focal plane. Two monitoring photodiodes in the integrating sphere measure the photon flux. These monitor diodes are tested separately with a calibrated standard photodiode mounted in the focal plane to create responsivity curves that relate the monitor diode signal to the photon flux at the focal plane.
During SCA testing the number of frames in the exposures for each wavelength were adjusted for approximately 8000 electrons of accumulated signal. Reference pixel correction, median detector photon transfer gain measured at 1400nm, electronics gain, Lambertian correction, and photon flux calibration with the photodiodes were then applied to the data.

12.2 Median Plots

The charts on the following pages show the median SCA QE per wavelength using the most recent flux calibration photodiode data collected by the DCL in January 2023. The 50% of max QE cutoff is calculated based on a linear fit of QE median values between 2450 and 2550 nm. These QE curves also show a slight increase in QE above the cutoff wavelength of 2500nm, which was recently attributed to a 2-3% short wavelength leak in the 1850 nm long pass filter used for wavelengths longer than 1350nm. Four non-flight SCAs were re-measured for QE with a 2500nm long pass filter, which confirmed that the QE drops off to near zero for wavelengths between 2500-2700nm. No light leaks were found in the other filters.

Figure 84: Median QE for flight SCAs

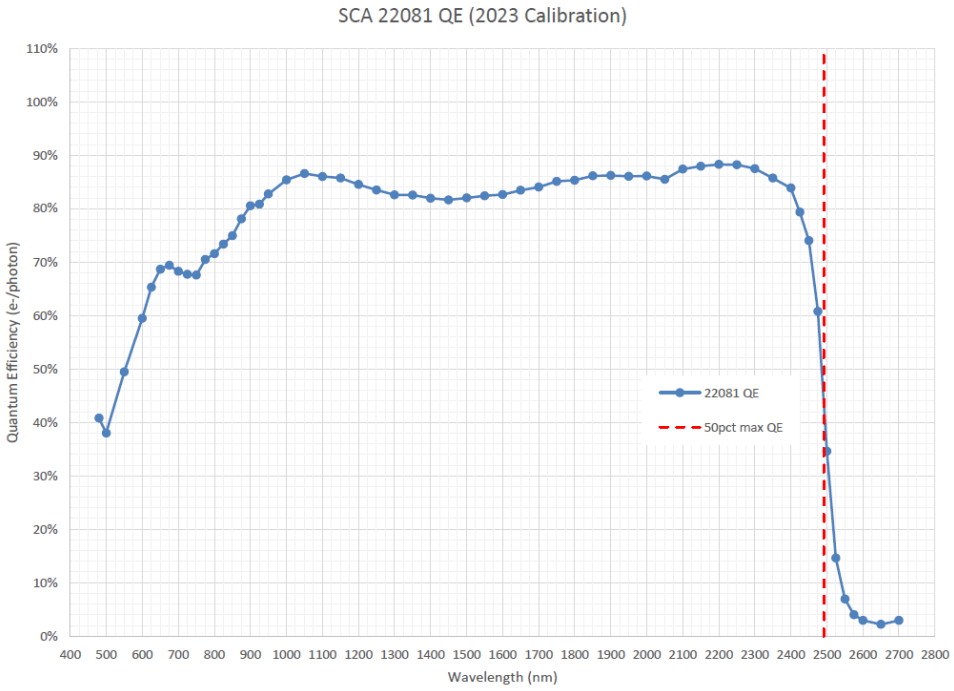

WL (nm)	QE (%)	WL (nm)	QE (%)
480	40.8%	1500	82.0%
500	38.0%	1550	82.4%
550	49.5%	1600	82.6%
600	59.5%	1650	83.5%
625	65.3%	1700	84.0%
650	68.7%	1750	85.1%
675	69.4%	1800	85.3%
700	68.3%	1850	86.1%
725	67.7%	1900	86.2%
750	67.6%	1950	86.1%
775	70.5%	2000	86.1%
800	71.6%	2050	85.5%
825	73.4%	2100	87.4%
850	74.9%	2150	87.9%
875	78.1%	2200	88.3%
900	80.5%	2250	88.2%
925	80.8%	2300	87.5%
950	82.7%	2350	85.7%
1000	85.4%	2400	83.9%
1050	86.6%	2425	79.4%
1100	86.0%	2450	74.0%
1150	85.7%	2475	60.8%
1200	84.5%	2500	34.6%
1250	83.5%	2525	14.6%
1300	82.6%	2550	6.9%
1350	82.6%	2575	4.0%
1400	82.0%	2600	2.9%
1450	81.6%	2650	2.2%
		2700	2.9%

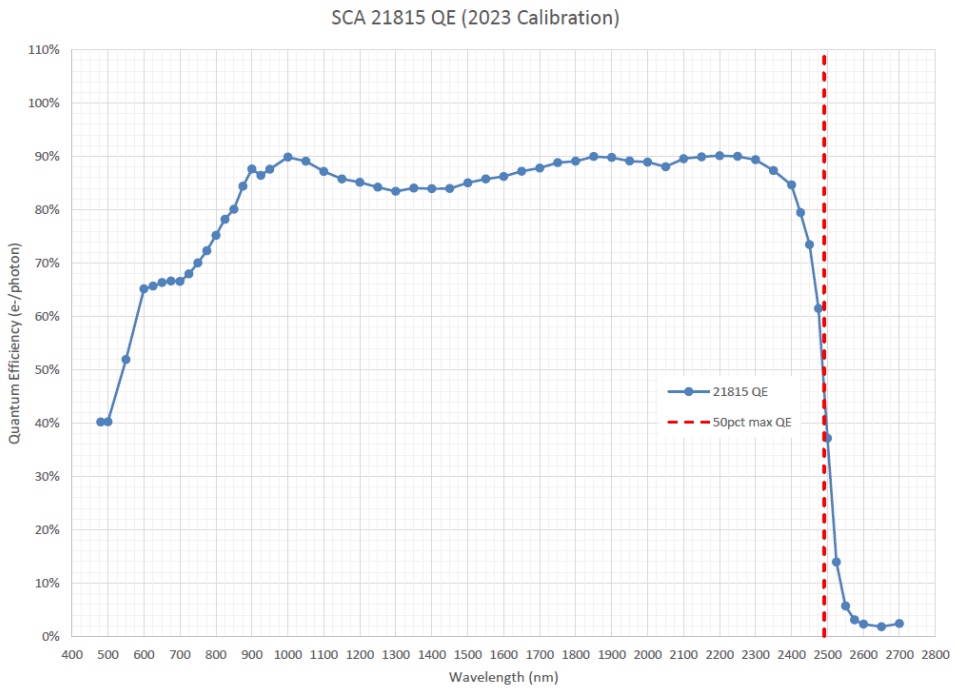

WL (nm)	QE (%)	WL (nm)	QE (%)
480	40.2%	1500	85.0%
500	40.2%	1550	85.8%
550	51.9%	1600	86.2%
600	65.1%	1650	87.2%
625	65.7%	1700	87.8%
650	66.3%	1750	88.8%
675	66.6%	1800	89.1%
700	66.6%	1850	90.0%
725	68.0%	1900	89.8%
750	70.0%	1950	89.1%
775	72.3%	2000	88.9%
800	75.2%	2050	88.1%
825	78.2%	2100	89.6%
850	80.1%	2150	89.9%
875	84.4%	2200	90.1%
900	87.6%	2250	90.0%
925	86.4%	2300	89.4%
950	87.6%	2350	87.3%
1000	89.9%	2400	84.6%
1050	89.1%	2425	79.5%
1100	87.2%	2450	73.5%
1150	85.8%	2475	61.5%
1200	85.1%	2500	37.1%
1250	84.2%	2525	13.9%
1300	83.5%	2550	5.7%
1350	84.1%	2575	3.1%
1400	83.9%	2600	2.3%
1450	84.0%	2650	1.8%
		2700	2.4%

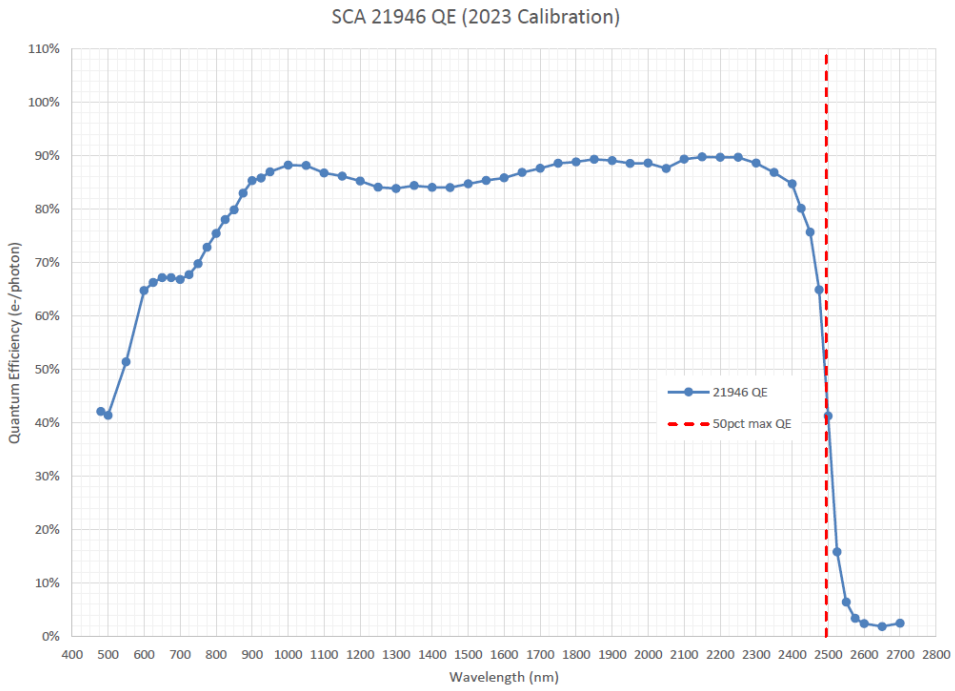

WL (nm)	QE (%)	WL (nm)	QE (%)
480	42.1%	1500	84.7%
500	41.4%	1550	85.4%
550	51.4%	1600	85.8%
600	64.7%	1650	86.8%
625	66.2%	1700	87.6%
650	67.2%	1750	88.6%
675	67.1%	1800	88.8%
700	66.8%	1850	89.3%
725	67.7%	1900	89.1%
750	69.8%	1950	88.5%
775	72.8%	2000	88.6%
800	75.4%	2050	87.6%
825	78.0%	2100	89.3%
850	79.9%	2150	89.8%
875	83.0%	2200	89.7%
900	85.3%	2250	89.7%
925	85.8%	2300	88.6%
950	87.0%	2350	86.9%
1000	88.2%	2400	84.7%
1050	88.2%	2425	80.1%
1100	86.7%	2450	75.7%
1150	86.2%	2475	64.9%
1200	85.3%	2500	41.3%
1250	84.1%	2525	15.8%
1300	83.8%	2550	6.4%
1350	84.4%	2575	3.3%
1400	84.1%	2600	2.4%
1450	84.0%	2650	1.8%
		2700	2.5%

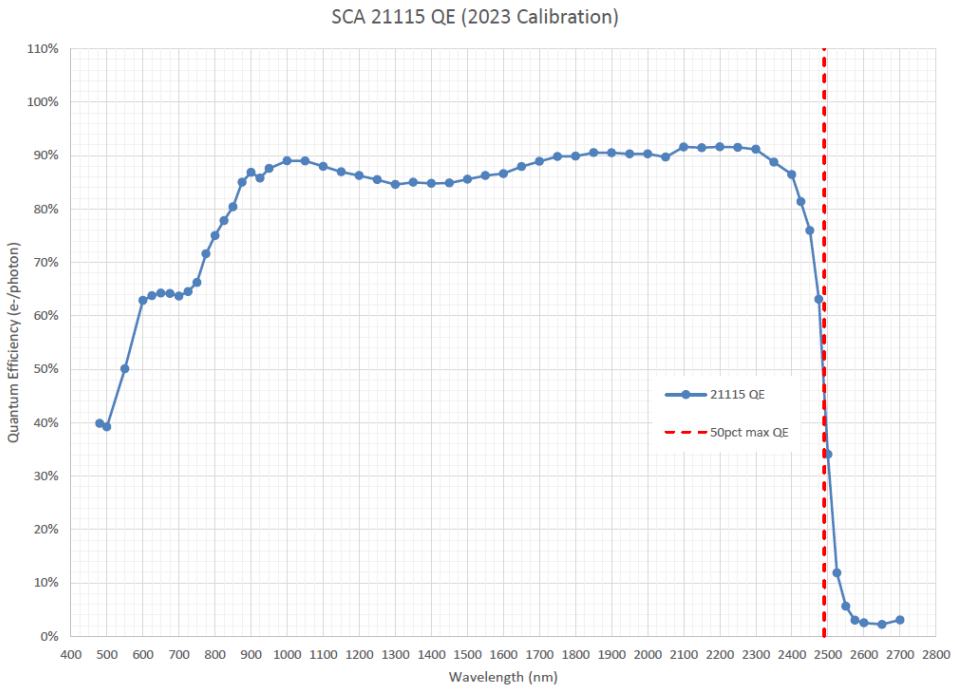

WL (nm)	QE (%)	WL (nm)	QE (%)
480	39.9%	1500	85.6%
500	39.2%	1550	86.3%
550	50.1%	1600	86.6%
600	62.9%	1650	87.9%
625	63.8%	1700	88.9%
650	64.3%	1750	89.8%
675	64.2%	1800	89.9%
700	63.7%	1850	90.5%
725	64.5%	1900	90.5%
750	66.2%	1950	90.3%
775	71.6%	2000	90.3%
800	75.0%	2050	89.7%
825	77.8%	2100	91.6%
850	80.4%	2150	91.5%
875	85.0%	2200	91.6%
900	86.8%	2250	91.5%
925	85.8%	2300	91.2%
950	87.6%	2350	88.8%
1000	89.0%	2400	86.4%
1050	89.0%	2425	81.4%
1100	88.0%	2450	76.0%
1150	86.9%	2475	63.1%
1200	86.3%	2500	34.1%
1250	85.5%	2525	11.9%
1300	84.6%	2550	5.6%
1350	85.0%	2575	3.0%
1400	84.8%	2600	2.5%
1450	84.9%	2650	2.2%
		2700	3.1%

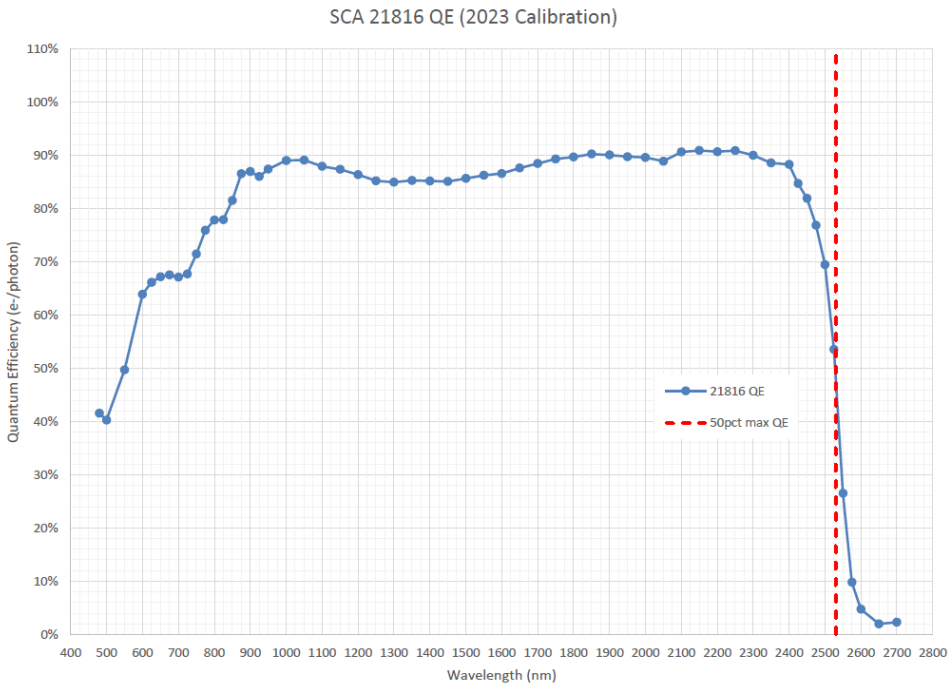

WL (nm)	QE (%)	WL (nm)	QE (%)
480	41.6%	1500	85.7%
500	40.3%	1550	86.3%
550	49.7%	1600	86.6%
600	63.9%	1650	87.6%
625	66.2%	1700	88.5%
650	67.2%	1750	89.3%
675	67.6%	1800	89.7%
700	67.1%	1850	90.3%
725	67.7%	1900	90.1%
750	71.5%	1950	89.7%
775	75.9%	2000	89.6%
800	77.8%	2050	88.9%
825	77.9%	2100	90.6%
850	81.5%	2150	90.9%
875	86.5%	2200	90.7%
900	87.0%	2250	90.9%
925	86.0%	2300	90.0%
950	87.4%	2350	88.6%
1000	89.0%	2400	88.3%
1050	89.1%	2425	84.7%
1100	87.9%	2450	81.9%
1150	87.4%	2475	76.9%
1200	86.4%	2500	69.5%
1250	85.2%	2525	53.5%
1300	84.9%	2550	26.5%
1350	85.3%	2575	9.8%
1400	85.2%	2600	4.8%
1450	85.1%	2650	2.0%
		2700	2.3%

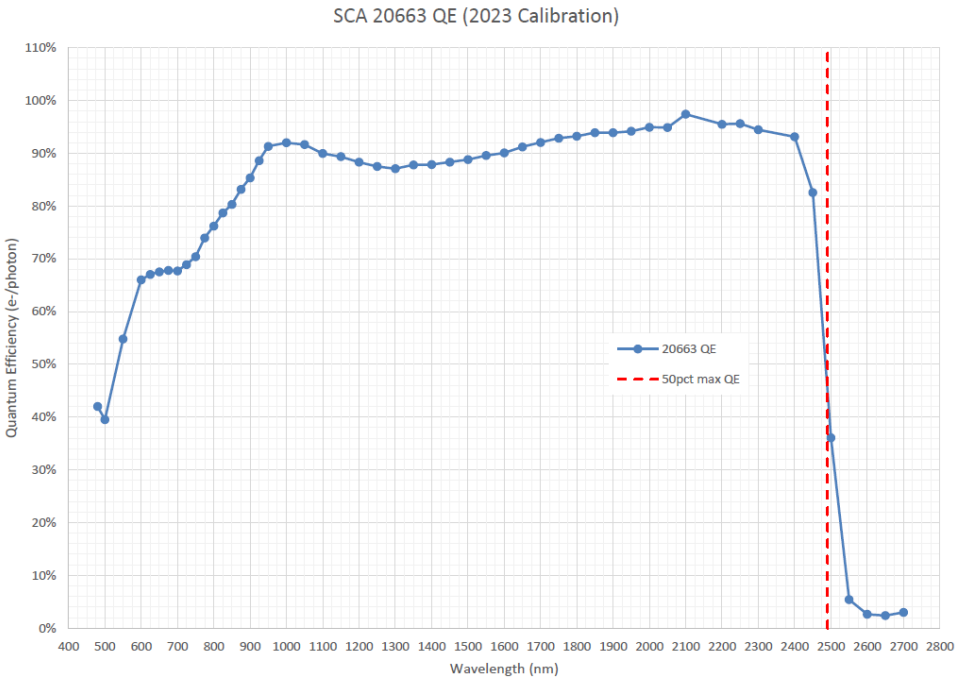

WL (nm)	QE (%)	WL (nm)	QE (%)
480	42.0%	1500	88.8%
500	39.5%	1550	89.6%
550	54.8%	1600	90.1%
600	66.0%	1650	91.2%
625	67.0%	1700	92.1%
650	67.5%	1750	92.9%
675	67.8%	1800	93.2%
700	67.7%	1850	93.9%
725	68.9%	1900	93.9%
750	70.4%	1950	94.2%
775	74.0%	2000	94.9%
800	76.2%	2050	94.9%
825	78.7%	2100	97.4%
850	80.3%	2150	-
875	83.2%	2200	95.5%
900	85.4%	2250	95.6%
925	88.6%	2300	94.5%
950	91.3%	2350	-
1000	92.0%	2400	93.1%
1050	91.7%	2425	-
1100	90.0%	2450	82.6%
1150	89.4%	2475	-
1200	88.3%	2500	36.1%
1250	87.5%	2525	-
1300	87.1%	2550	5.4%
1350	87.8%	2575	-
1400	87.9%	2600	2.6%
1450	88.3%	2650	2.4%
		2700	3.0%

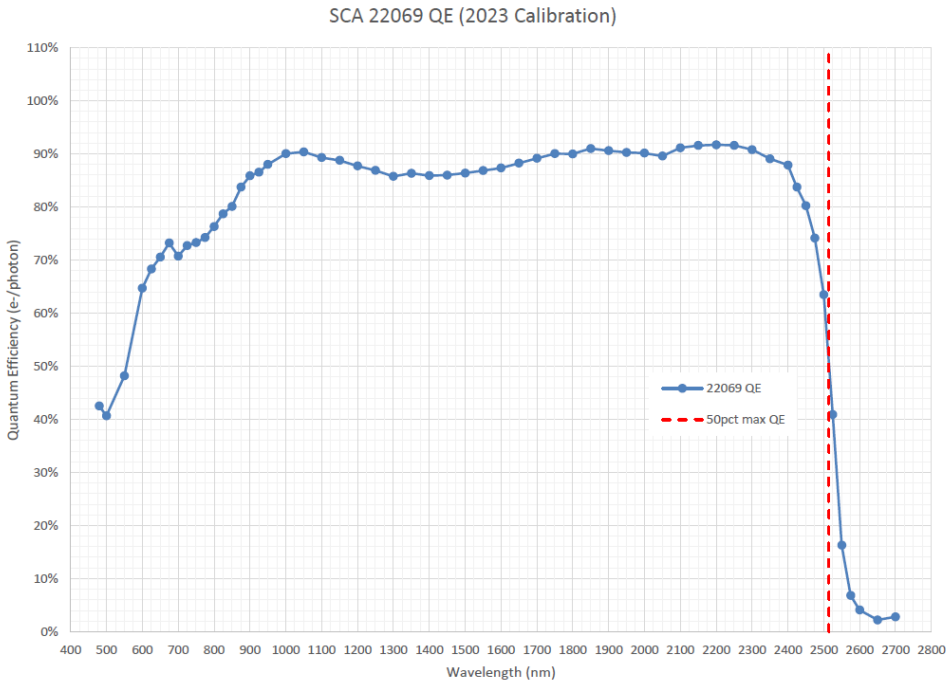

WL (nm)	QE (%)	WL (nm)	QE (%)
480	42.5%	1500	86.4%
500	40.6%	1550	86.8%
550	48.2%	1600	87.3%
600	64.7%	1650	88.2%
625	68.3%	1700	89.2%
650	70.6%	1750	90.0%
675	73.2%	1800	90.0%
700	70.7%	1850	91.0%
725	72.7%	1900	90.6%
750	73.3%	1950	90.3%
775	74.2%	2000	90.1%
800	76.3%	2050	89.6%
825	78.7%	2100	91.1%
850	80.1%	2150	91.6%
875	83.7%	2200	91.7%
900	85.9%	2250	91.6%
925	86.5%	2300	90.8%
950	88.0%	2350	89.1%
1000	90.0%	2400	87.9%
1050	90.4%	2425	83.7%
1100	89.3%	2450	80.2%
1150	88.8%	2475	74.1%
1200	87.7%	2500	63.5%
1250	86.9%	2525	40.9%
1300	85.8%	2550	16.3%
1350	86.3%	2575	6.8%
1400	85.9%	2600	4.1%
1450	86.0%	2650	2.2%
		2700	2.8%

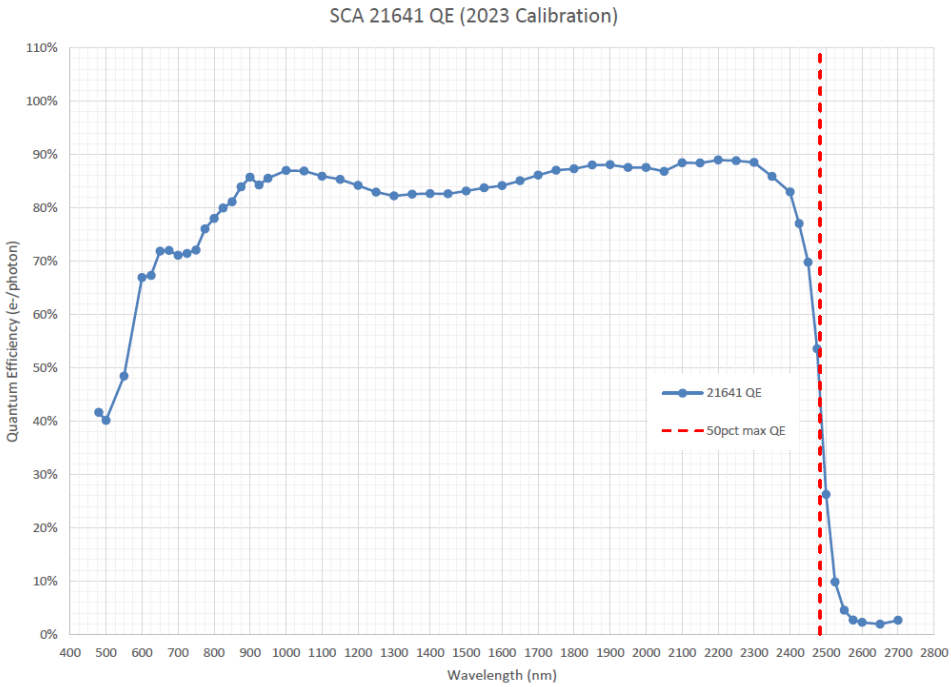

WL (nm)	QE (%)	WL (nm)	QE (%)
480	41.6%	1500	83.1%
500	40.1%	1550	83.7%
550	48.4%	1600	84.1%
600	66.9%	1650	85.1%
625	67.3%	1700	86.1%
650	71.8%	1750	87.0%
675	72.0%	1800	87.3%
700	71.1%	1850	88.0%
725	71.4%	1900	88.1%
750	72.1%	1950	87.5%
775	76.0%	2000	87.5%
800	78.0%	2050	86.8%
825	79.9%	2100	88.4%
850	81.1%	2150	88.4%
875	83.9%	2200	88.9%
900	85.7%	2250	88.8%
925	84.3%	2300	88.5%
950	85.5%	2350	85.9%
1000	87.0%	2400	83.0%
1050	86.9%	2425	77.0%
1100	85.9%	2450	69.8%
1150	85.3%	2475	53.5%
1200	84.2%	2500	26.2%
1250	82.9%	2525	9.8%
1300	82.2%	2550	4.6%
1350	82.6%	2575	2.7%
1400	82.7%	2600	2.3%
1450	82.6%	2650	1.9%
		2700	2.6%

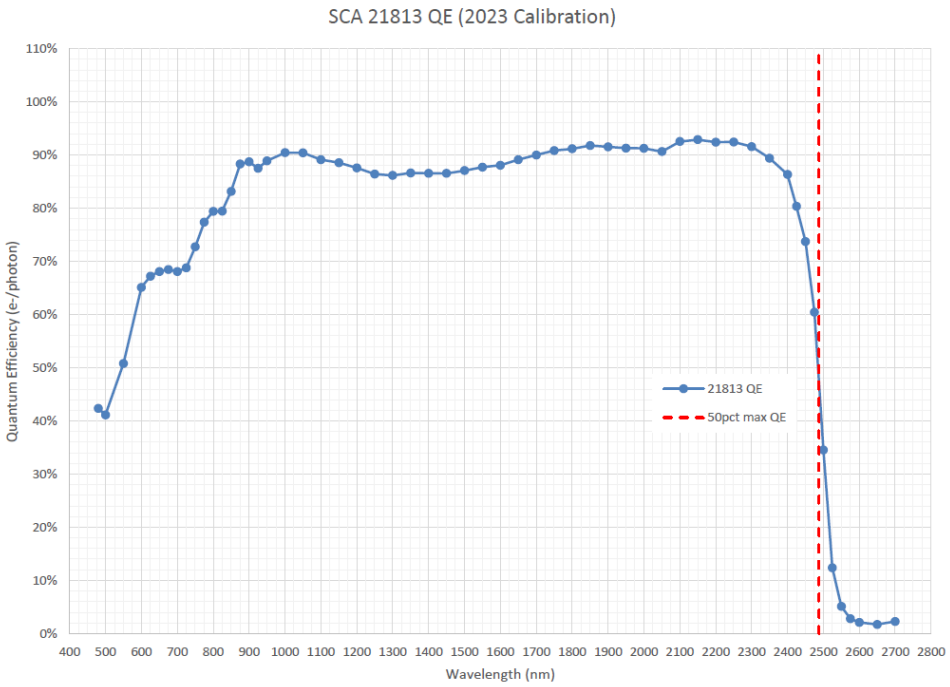

WL (nm)	QE (%)	WL (nm)	QE (%)
480	42.3%	1500	87.1%
500	41.1%	1550	87.7%
550	50.8%	1600	88.1%
600	65.1%	1650	89.1%
625	67.2%	1700	90.0%
650	68.1%	1750	90.8%
675	68.5%	1800	91.2%
700	68.1%	1850	91.8%
725	68.8%	1900	91.5%
750	72.7%	1950	91.3%
775	77.3%	2000	91.2%
800	79.4%	2050	90.6%
825	79.4%	2100	92.5%
850	83.1%	2150	92.9%
875	88.3%	2200	92.4%
900	88.7%	2250	92.4%
925	87.5%	2300	91.6%
950	88.9%	2350	89.4%
1000	90.4%	2400	86.3%
1050	90.4%	2425	80.3%
1100	89.1%	2450	73.7%
1150	88.5%	2475	60.4%
1200	87.6%	2500	34.5%
1250	86.4%	2525	12.4%
1300	86.1%	2550	5.1%
1350	86.6%	2575	2.8%
1400	86.6%	2600	2.1%
1450	86.5%	2650	1.7%
		2700	2.3%

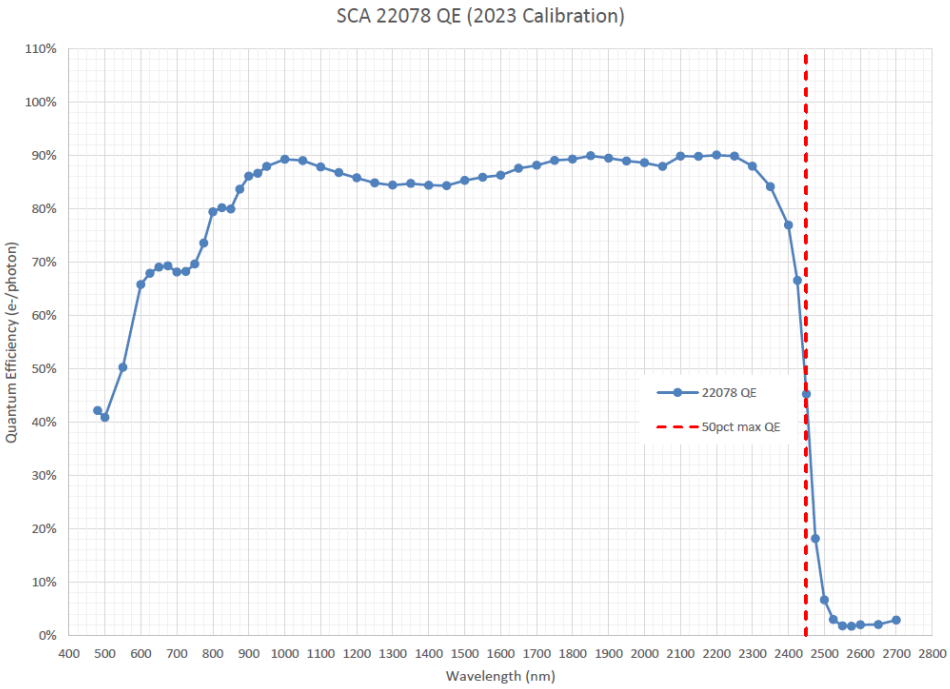

WL (nm)	QE (%)	WL (nm)	QE (%)
480	42.2%	1500	85.3%
500	40.8%	1550	85.9%
550	50.2%	1600	86.3%
600	65.8%	1650	87.6%
625	67.9%	1700	88.1%
650	69.1%	1750	89.1%
675	69.3%	1800	89.3%
700	68.1%	1850	89.9%
725	68.3%	1900	89.5%
750	69.6%	1950	89.0%
775	73.6%	2000	88.6%
800	79.4%	2050	87.9%
825	80.2%	2100	89.9%
850	79.9%	2150	89.8%
875	83.6%	2200	90.1%
900	86.1%	2250	89.9%
925	86.6%	2300	88.0%
950	88.0%	2350	84.2%
1000	89.3%	2400	76.9%
1050	89.0%	2425	66.6%
1100	87.8%	2450	45.2%
1150	86.8%	2475	18.2%
1200	85.8%	2500	6.6%
1250	84.9%	2525	3.0%
1300	84.4%	2550	1.8%
1350	84.7%	2575	1.7%
1400	84.4%	2600	2.0%
1450	84.3%	2650	2.0%
		2700	2.9%

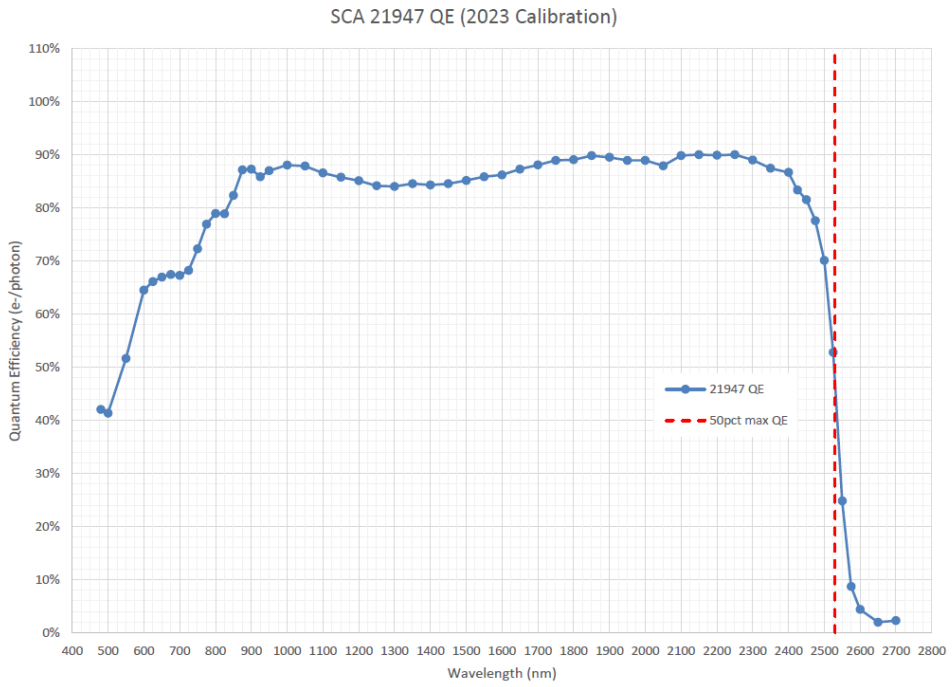

WL (nm)	QE (%)	WL (nm)	QE (%)
480	42.0%	1500	85.1%
500	41.3%	1550	85.8%
550	51.6%	1600	86.2%
600	64.5%	1650	87.3%
625	66.1%	1700	88.1%
650	66.9%	1750	88.9%
675	67.4%	1800	89.1%
700	67.3%	1850	89.8%
725	68.2%	1900	89.5%
750	72.3%	1950	88.9%
775	76.9%	2000	88.9%
800	78.9%	2050	87.9%
825	78.9%	2100	89.8%
850	82.3%	2150	90.0%
875	87.1%	2200	89.9%
900	87.3%	2250	90.0%
925	85.9%	2300	89.0%
950	87.0%	2350	87.4%
1000	88.1%	2400	86.7%
1050	87.9%	2425	83.4%
1100	86.6%	2450	81.5%
1150	85.8%	2475	77.6%
1200	85.1%	2500	70.1%
1250	84.1%	2525	52.8%
1300	84.0%	2550	24.8%
1350	84.5%	2575	8.7%
1400	84.3%	2600	4.4%
1450	84.5%	2650	2.0%
		2700	2.3%

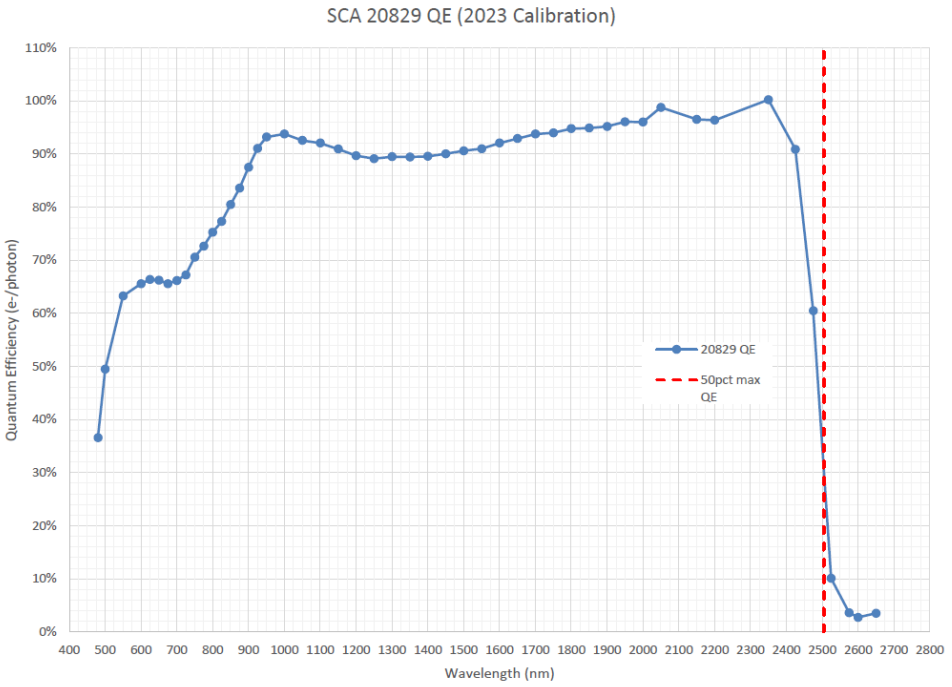

WL (nm)	QE (%)	WL (nm)	QE (%)
480	40.6%	1500	90.0%
500	36.6%	1550	90.6%
550	49.5%	1600	91.0%
600	63.3%	1650	92.1%
625	65.6%	1700	92.9%
650	66.4%	1750	93.8%
675	66.2%	1800	94.0%
700	65.6%	1850	94.8%
725	66.2%	1900	94.9%
750	67.2%	1950	95.2%
775	70.6%	2000	96.1%
800	72.7%	2050	96.0%
825	75.3%	2100	98.8%
850	77.3%	2150	-
875	80.5%	2200	96.5%
900	83.6%	2250	96.4%
925	87.5%	2300	-
950	91.1%	2350	-
1000	93.2%	2400	100.2%
1050	93.8%	2425	-
1100	92.6%	2450	90.9%
1150	92.1%	2475	-
1200	90.9%	2500	60.5%
1250	89.7%	2525	-
1300	89.1%	2550	10.1%
1350	89.5%	2575	-
1400	89.4%	2600	3.6%
1450	89.6%	2650	2.7%
		2700	3.5%

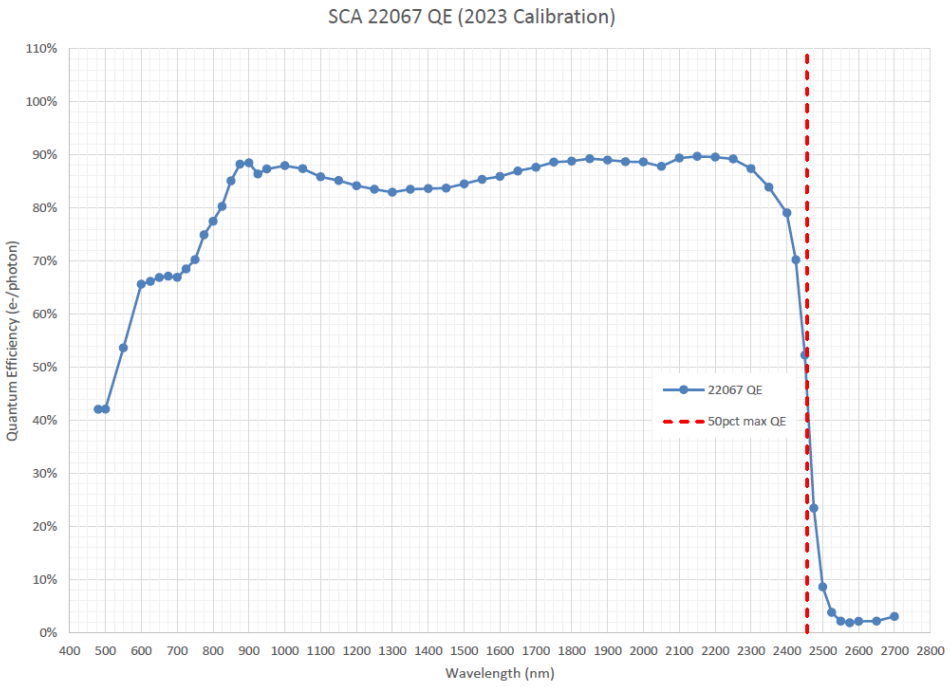

WL (nm)	QE (%)	WL (nm)	QE (%)
480	42.1%	1500	84.5%
500	42.1%	1550	85.4%
550	53.6%	1600	85.9%
600	65.6%	1650	86.9%
625	66.1%	1700	87.6%
650	66.9%	1750	88.6%
675	67.1%	1800	88.8%
700	66.9%	1850	89.2%
725	68.5%	1900	89.0%
750	70.2%	1950	88.7%
775	74.9%	2000	88.6%
800	77.5%	2050	87.8%
825	80.3%	2100	89.4%
850	85.1%	2150	89.7%
875	88.2%	2200	89.6%
900	88.5%	2250	89.2%
925	86.4%	2300	87.4%
950	87.3%	2350	83.9%
1000	87.9%	2400	79.0%
1050	87.4%	2425	70.2%
1100	85.8%	2450	52.2%
1150	85.2%	2475	23.4%
1200	84.2%	2500	8.6%
1250	83.5%	2525	3.8%
1300	82.9%	2550	2.2%
1350	83.5%	2575	1.9%
1400	83.6%	2600	2.1%
1450	83.7%	2650	2.2%
		2700	3.1%

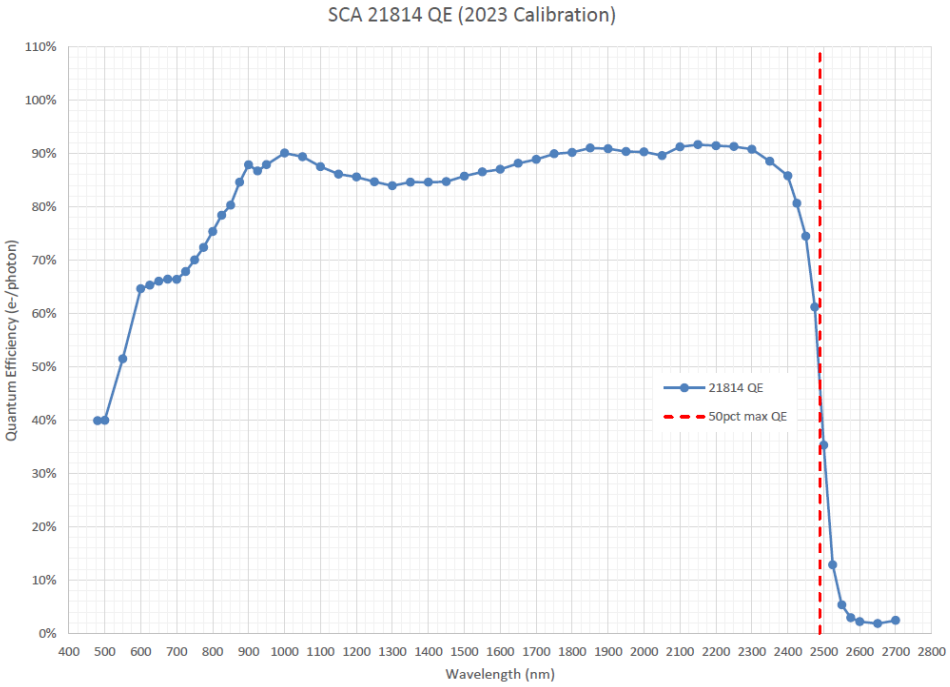

WL (nm)	QE (%)	WL (nm)	QE (%)
480	39.9%	1500	85.7%
500	40.0%	1550	86.5%
550	51.5%	1600	87.0%
600	64.6%	1650	88.1%
625	65.3%	1700	88.9%
650	66.0%	1750	89.9%
675	66.4%	1800	90.2%
700	66.4%	1850	91.0%
725	67.8%	1900	90.9%
750	70.0%	1950	90.4%
775	72.4%	2000	90.3%
800	75.3%	2050	89.6%
825	78.4%	2100	91.2%
850	80.3%	2150	91.7%
875	84.6%	2200	91.5%
900	87.9%	2250	91.3%
925	86.7%	2300	90.8%
950	87.9%	2350	88.5%
1000	90.1%	2400	85.8%
1050	89.4%	2425	80.7%
1100	87.5%	2450	74.5%
1150	86.1%	2475	61.2%
1200	85.6%	2500	35.3%
1250	84.7%	2525	12.9%
1300	83.9%	2550	5.4%
1350	84.6%	2575	2.9%
1400	84.6%	2600	2.2%
1450	84.7%	2650	1.8%
		2700	2.4%

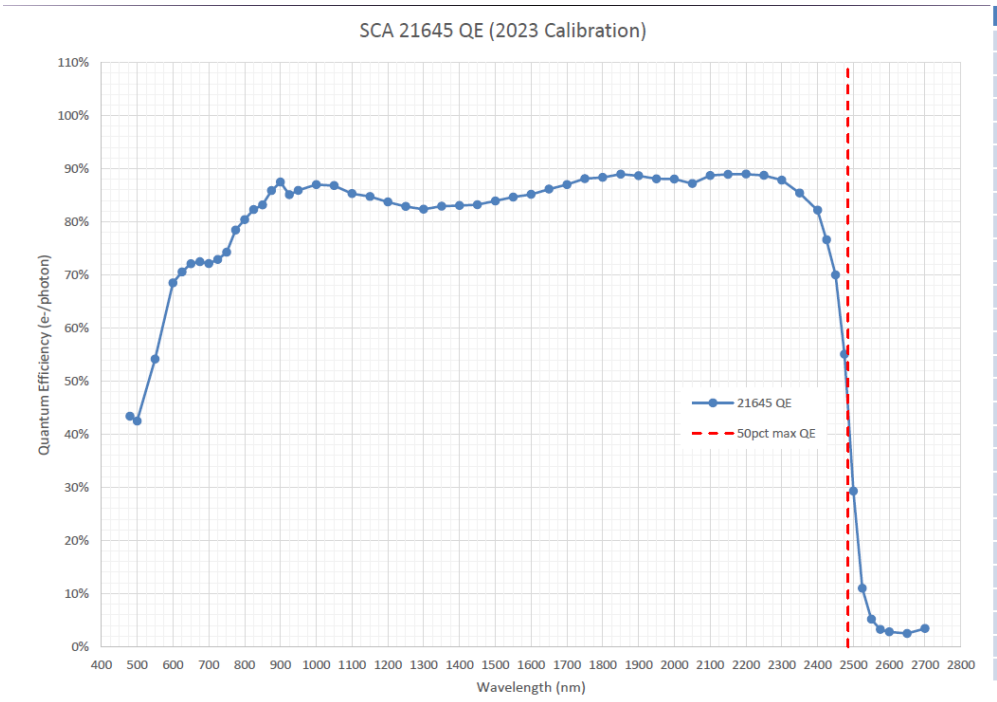

WL (nm)	QE (%)	WL (nm)	QE (%)
480	43.4%	1500	83.9%
500	42.5%	1550	84.7%
550	54.2%	1600	85.2%
600	68.5%	1650	86.1%
625	70.5%	1700	87.0%
650	72.1%	1750	88.1%
675	72.5%	1800	88.3%
700	72.1%	1850	89.0%
725	72.9%	1900	88.7%
750	74.3%	1950	88.1%
775	78.4%	2000	88.1%
800	80.4%	2050	87.2%
825	82.3%	2100	88.7%
850	83.2%	2150	88.9%
875	85.9%	2200	89.0%
900	87.5%	2250	88.7%
925	85.1%	2300	87.8%
950	85.9%	2350	85.4%
1000	87.0%	2400	82.2%
1050	86.8%	2425	76.6%
1100	85.3%	2450	70.0%
1150	84.8%	2475	55.1%
1200	83.7%	2500	29.3%
1250	82.9%	2525	11.0%
1300	82.4%	2550	5.2%
1350	82.9%	2575	3.2%
1400	83.1%	2600	2.8%
1450	83.2%	2650	2.5%
		2700	3.4%

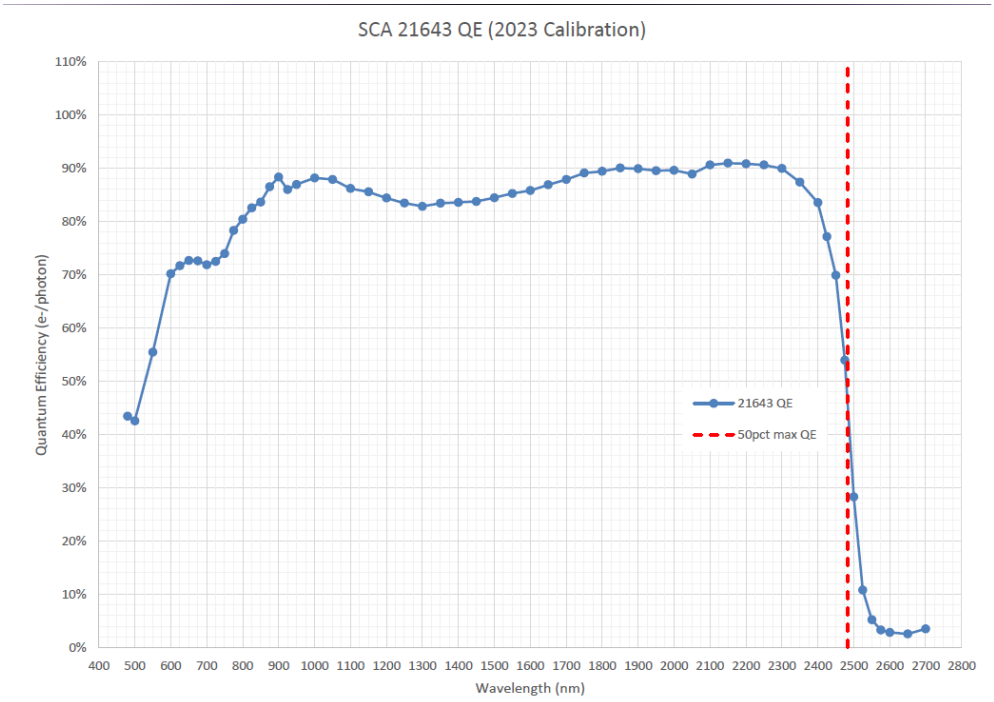

WL (nm)	QE (%)	WL (nm)	QE (%)
480	43.4%	1500	84.4%
500	42.6%	1550	85.3%
550	55.4%	1600	85.8%
600	70.2%	1650	86.9%
625	71.7%	1700	87.9%
650	72.7%	1750	89.1%
675	72.6%	1800	89.4%
700	71.9%	1850	90.0%
725	72.5%	1900	89.9%
750	74.0%	1950	89.5%
775	78.3%	2000	89.6%
800	80.4%	2050	88.9%
825	82.5%	2100	90.6%
850	83.6%	2150	90.9%
875	86.5%	2200	90.8%
900	88.3%	2250	90.6%
925	86.0%	2300	89.9%
950	86.9%	2350	87.4%
1000	88.2%	2400	83.5%
1050	87.9%	2425	77.1%
1100	86.2%	2450	69.9%
1150	85.6%	2475	54.0%
1200	84.4%	2500	28.3%
1250	83.4%	2525	10.8%
1300	82.8%	2550	5.2%
1350	83.4%	2575	3.3%
1400	83.6%	2600	2.8%
1450	83.7%	2650	2.5%
		2700	3.5%

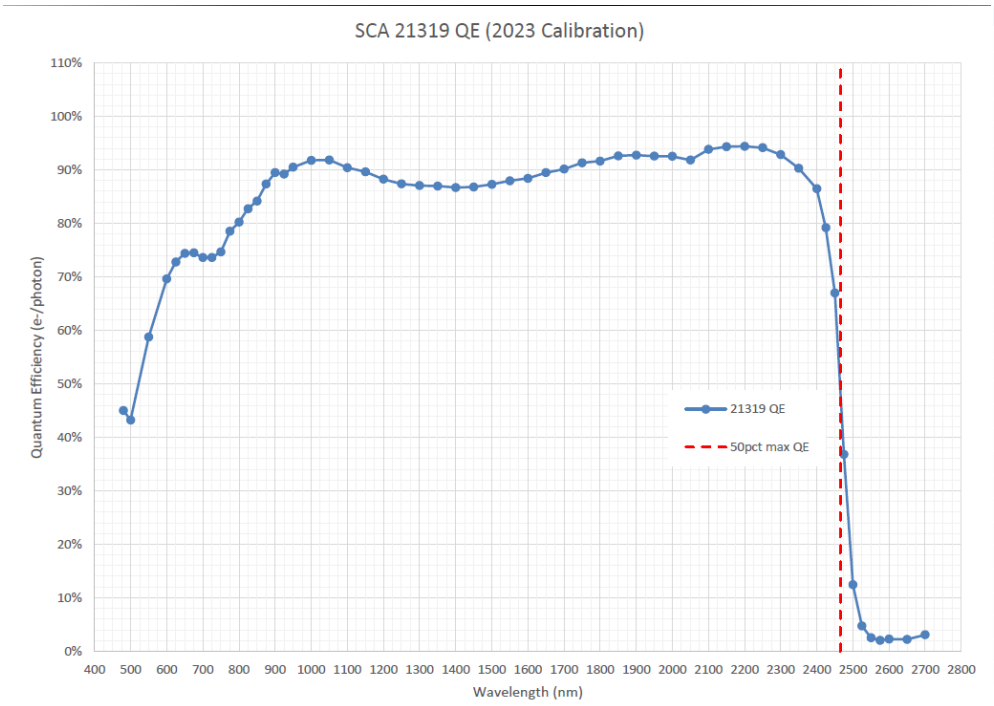

WL (nm)	QE (%)	WL (nm)	QE (%)
480	45.0%	1500	87.3%
500	43.2%	1550	88.0%
550	58.8%	1600	88.4%
600	69.6%	1650	89.5%
625	72.8%	1700	90.1%
650	74.4%	1750	91.3%
675	74.5%	1800	91.6%
700	73.6%	1850	92.6%
725	73.6%	1900	92.8%
750	74.7%	1950	92.6%
775	78.5%	2000	92.5%
800	80.2%	2050	91.8%
825	82.7%	2100	93.8%
850	84.2%	2150	94.3%
875	87.3%	2200	94.4%
900	89.5%	2250	94.1%
925	89.2%	2300	92.8%
950	90.5%	2350	90.3%
1000	91.8%	2400	86.5%
1050	91.8%	2425	79.2%
1100	90.4%	2450	67.0%
1150	89.6%	2475	36.8%
1200	88.3%	2500	12.4%
1250	87.4%	2525	4.7%
1300	87.1%	2550	2.5%
1350	87.0%	2575	2.0%
1400	86.7%	2600	2.3%
1450	86.8%	2650	2.2%
		2700	3.1%

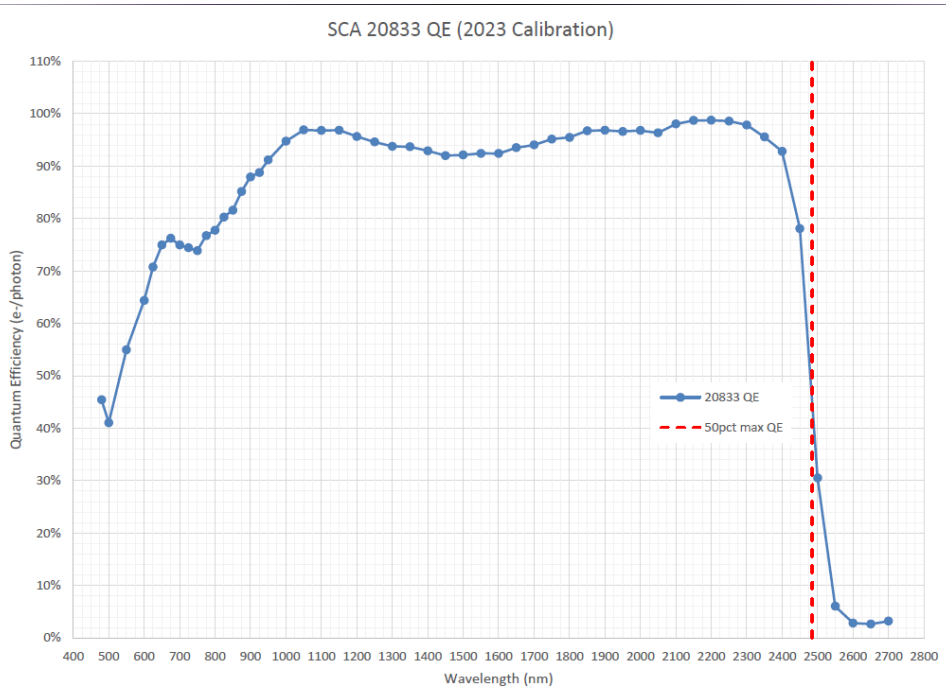

WL (nm)	QE (%)	WL (nm)	QE (%)
480	45.4%	1500	92.1%
500	41.0%	1550	92.4%
550	55.0%	1600	92.4%
600	64.4%	1650	93.5%
625	70.7%	1700	94.1%
650	74.9%	1750	95.2%
675	76.2%	1800	95.5%
700	75.0%	1850	96.7%
725	74.4%	1900	96.8%
750	73.9%	1950	96.6%
775	76.7%	2000	96.8%
800	77.8%	2050	96.3%
825	80.3%	2100	98.1%
850	81.6%	2150	98.7%
875	85.2%	2200	98.8%
900	87.9%	2250	98.6%
925	88.8%	2300	97.9%
950	91.2%	2350	95.6%
1000	94.8%	2400	92.8%
1050	96.9%	2425	-
1100	96.8%	2450	78.1%
1150	96.9%	2475	-
1200	95.7%	2500	30.5%
1250	94.6%	2525	-
1300	93.8%	2550	6.0%
1350	93.7%	2575	-
1400	92.9%	2600	2.8%
1450	92.0%	2650	2.6%
		2700	3.2%

12.3 Cutoff Wavelength

The requirement for the cutoff wavelength for the SCAs is 2.5±.05 μm (2500 ± 50 nm). The cutoff wavelength is defined to be where the QE is 50% of its peak value. QE was measured during Acceptance Testing in increments of 25nm in a range of 2400nm to 2600nm, the 50% peak value threshold was determined by interpolation of the median QE between the closest increments. Waivers for 22078 and 22067 have been written and accepted by the project.

Table 14: Cutoff Wavelength

SCA SN	Cutoff Wavelength (nm)
22081	2490
21815	2480
21946	2493
21115	2489
21816	2537
20663	2490
22069	2516
21641	2482
21813	2486
22078	2424
21947	2525
20829	2504
22067	2442
21814	2488
21645	2483
21643	2481
21319	2463
20833	2485

13 COSMIC RAYS

13.1 Snowballs

Snowballs are transient events observed in HgCdTe detectors. They occur when the charge of a few pixels suddenly increases. They appear between consecutive detector reads, after which the affected pixels return to normal behavior.
Several authors have noticed the appearance of snowball events in HgCdTe photodiode arrays. These features were observed, for example, in the Wide Field Camera 3 (WFC3) of the Hubble Space Telescope and in the NIRSpec and NIRCam instruments of the James Webb Space Telescope (JWST). In all cases, they had a low rate of occurrence, but it was challenging to present a clear picture of what may be the source of the snowball's events. Several hypotheses have been proposed about its origin, from the decay of radioactive contaminants to cosmic rays.

Per requirements the materials used in SCA construction shall not cause detectable high-energy particle impingement effects at a rate greater than one event/hour. To investigate whether this requirement is met, dark current and noise data sets acquired during all tests performed in RST Flight detectors were analyzed.

The data was collected in the NASA/GSFC and BAE Systems, Inc (former Ball Aerospace).
A snowball event was selected if it met the following criteria: the value of the pixel was above the Gaussian mean plus 50 times the Gaussian standard deviation of the background signal level in the frame; the pixel exceeded this threshold less than 70 percent of the time (to avoid hot pixels); the event was kept only if the four nearest neighbor pixels were above the Gaussian mean plus 25 times the Gaussian standard deviation of the signal level in the frame; and if the second nearest neighbors were above the Gaussian mean plus ten times the Gaussian standard deviation in the frame. Only events circular in shape, where the charge collected was larger or equal to 10^5 electrons, and the snowball size was larger than 9 pixels, were counted as a "snowball."

Figure 85 shows the snowball rate from all snowballs found during the Flight Acceptance Test (SCA), Triplet test, FPS test, WFI-TVAC1, and WFI-TVAC2.

Figure 85: Snowball rate in Flight detectors during Flight Acceptance Test (SCA), Triplet test, FPS, WFI-TVAC1, and WFI-TVAC2.

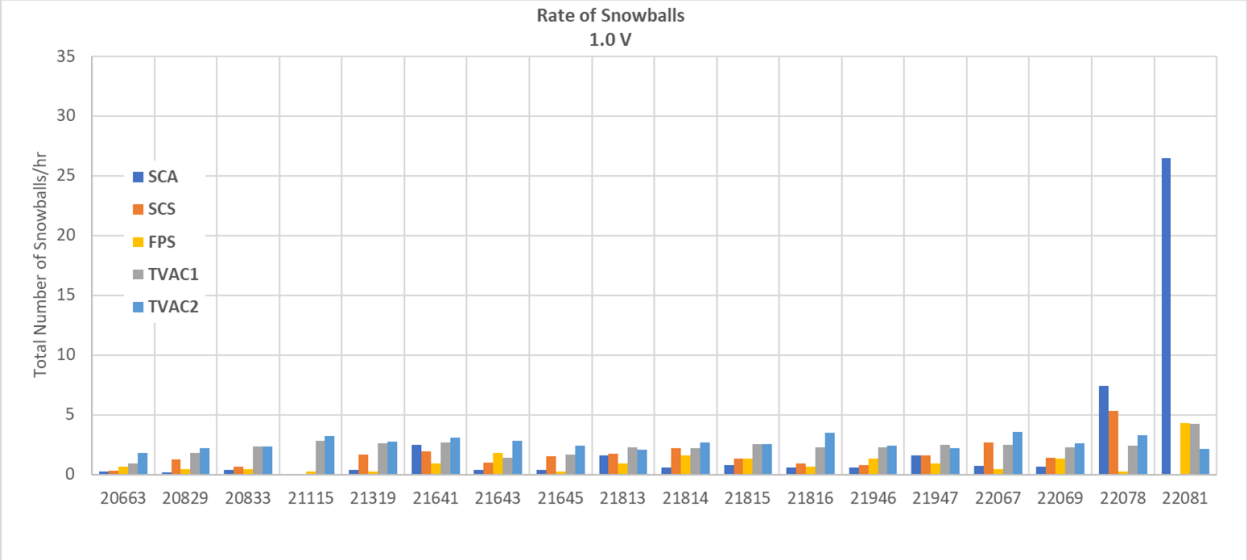

On average, the snowball rate during WFI-TVAC1 and WFI-TVAC2 increased compared to the Flight Acceptance test, Triplet test, and FPS test. The WFI-TVAC1 and WFI-TVAC2 were conducted in Boulder, Colorado, while previous tests were carried out at Goddard Space Flight Center (Greenbelt, MD).
Several of the snowballs observed were repeaters, falling in the same location as a previous snowball. The Figures below show the number of snowballs found in each detector and each test for non-repeated and repeated locations.

Figure 86: Snowball rate for non-repeated snowballs in Flight detectors during Flight Acceptance Test (SCA), Triplet test (SCS), FPS, WFI-TVAC1, and WFI-TVAC2.

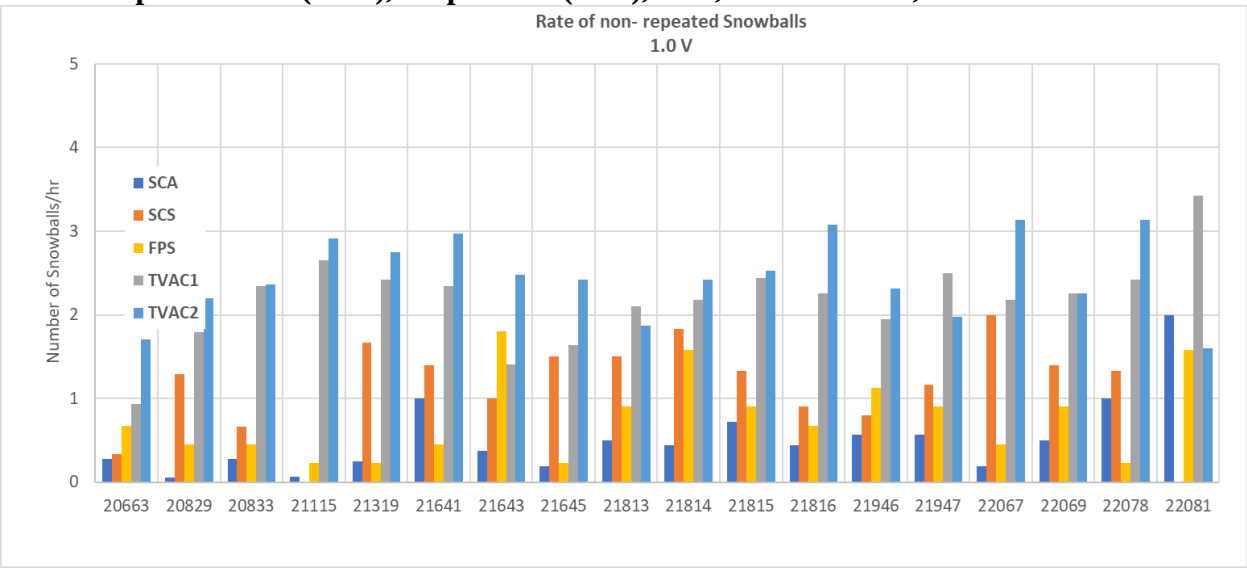

Figure 87: Snowball rate for repeated snowballs in RST Flight detectors during Flight Acceptance Test (SCA), Triplet test (SCS), FPS, WFI-TVAC1, and WFI-TVAC2.

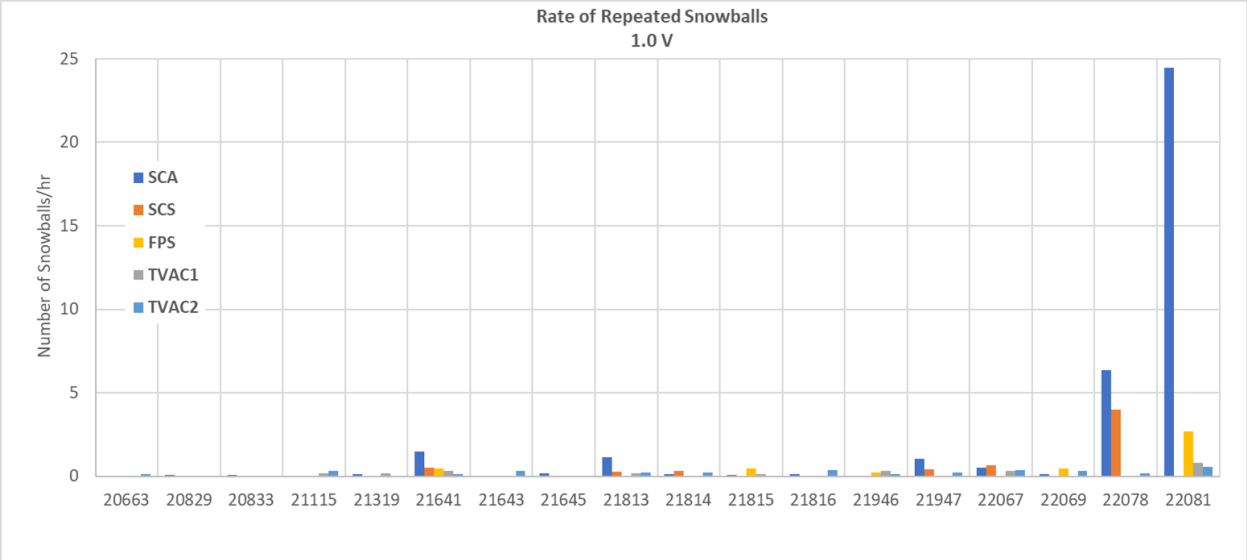

The number of snowballs repeating at the same localization decreased significantly over time. Figure 88 shows the snowball rate for all detectors for the different tests. It discriminates between snowballs that are repeated or not at the same location. The decrease in the snowball rate at the same location over time is most evident in detectors 22078 and 22081.

Figure 88: Snowball rate for all detectors combined for the different tests.

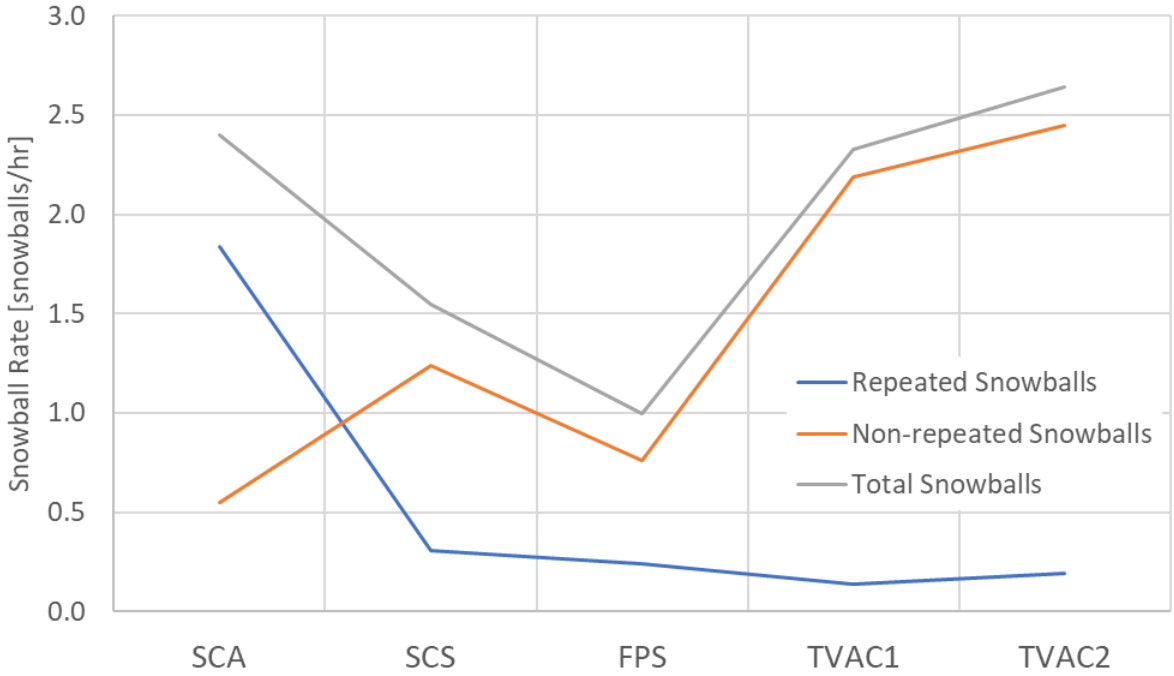

Figure 89 presents an example of the accumulated charge versus the number of affected pixels for snowballs during GSFC tests and BAE tests in detector 22078. Sixteen snowballs repeated several times at the same location during GSFC tests. The right plot of Figure 89 shows the accumulated charge vs affected pixels in those 16 repeated snowballs.

The central pixels within several of the snowballs were saturated which caused the accumulated charge to flatten out even as the number of affected pixels increased.

Figure 89: Accumulated charge vs number of affected pixels in detector 22078. Left: All snowballs. Right: 16 snowballs repeated several times.

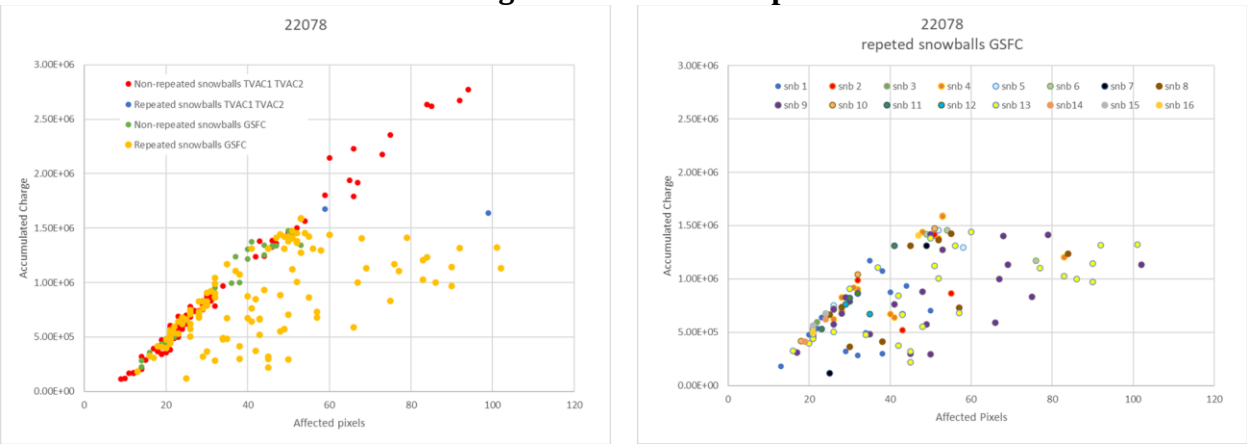

The following tables show snowball statistics during each SCA test campaign.

Table 15: Snowballs statistics during Flight Acceptance Test

Flight Acceptance Test							
Detector	Hours	number of snowballs	Rate of Snowballs (snb/hr)	Number of non-repeated snowballs	Number of repeated snowballs	Non-repeated snowballs/ hr	Repeated snowballs/ hr
20663	22	6	0.273	6	0	0.273	0.000
20829	20	3	0.150	1	2	0.050	0.100
20833	32	11	0.344	9	2	0.281	0.063
21115	16	1	0.063	1	0	0.063	0.000
21319	16	6	0.375	4	2	0.250	0.125
21641	16	40	2.500	16	24	1.000	1.500
21643	16	6	0.375	6	0	0.375	0.000
21645	16	6	0.375	3	3	0.188	0.188
21813	16	26	1.625	8	18	0.500	1.125
21814	32	18	0.563	14	4	0.438	0.125
21815	32	25	0.781	23	2	0.719	0.063
21816	16	9	0.563	7	2	0.438	0.125
21946	16	9	0.563	9	0	0.563	0.000
21947	16	26	1.625	9	17	0.563	1.063
22067	16	11	0.688	3	8	0.188	0.500
22069	16	10	0.625	8	2	0.500	0.125
22078	16	118	7.375	16	102	1.000	6.375
22081	16	423	26.438	32	391	2.000	24.438
Total	330	754	2.28	175	579	0.53	1.75

Table 16: Snowballs statistics during Triplet Test

Triplet Test							
Detector	Hours	number of snowballs	Rate of Snowballs (snb/hr)	Number of non-repeated snowballs	Number of repeated snowballs	Non-repeated snowballs/ hr	Repeated snowballs/ hr
20663	6	2	0.333	2	0	0.333	0.000
20829	14	18	1.286	18	0	1.286	0.000
20833	6	4	0.667	4	0	0.667	0.000
21115	N/A				0		
21319	6	10	1.667	10	0	1.667	0.000
21641	10	19	1.900	14	5	1.400	0.500
21643	12	12	1.000	12	0	1.000	0.000
21645	6	9	1.500	9	0	1.500	0.000
21813	12	21	1.750	18	3	1.500	0.250
21814	6	13	2.167	11	2	1.833	0.333
21815	6	8	1.333	8	0	1.333	0.000
21816	10	9	0.900	9	0	0.900	0.000
21946	10	8	0.800	8	0	0.800	0.000
21947	12	19	1.583	14	5	1.167	0.417
22067	6	16	2.667	12	4	2.000	0.667
22069	10	14	1.400	14	0	1.400	0.000
22078	6	32	5.333	8	24	1.333	4.000
22081	N/A						
Total	138	214	1.55	171	43	1.24	0.31

Table 17: Snowballs statistics during FPS

FPS: Initial Final Cold1-Cold4							
Detector	Hours	number of snowballs	Rate of Snowballs (snb/hr)	Number of non-repeated snowballs	Number of repeated snowballs	Non-repeated snowballs/ hr	Repeated snowballs/ hr
20663	4.44	3	0.676	3	0	0.676	0.000
20829	4.44	2	0.450	2	0	0.450	0.000
20833	4.44	2	0.450	2	0	0.450	0.000
21115	4.44	1	0.225	1	0	0.225	0.000
21319	4.44	1	0.225	1	0	0.225	0.000
21641	4.44	4	0.901	2	2	0.450	0.450
21643	4.44	8	1.802	8	0	1.802	0.000
21645	4.44	1	0.225	1	0	0.225	0.000
21813	4.44	4	0.901	4	0	0.901	0.000

21814	4.44	7	1.577	7	0	1.577	0.000
21815	4.44	6	1.351	4	2	0.901	0.450
21816	4.44	3	0.676	3	0	0.676	0.000
21946	4.44	6	1.351	5	1	1.126	0.225
21947	4.44	4	0.901	4	0	0.901	0.000
22067	4.44	2	0.450	2	0	0.450	0.000
22069	4.44	6	1.351	4	2	0.901	0.450
22078	4.44	1	0.225	1	0	0.225	0.000
22081	4.44	19	4.279	7	12	1.577	2.703
Total	79.92	80	1.00	61	19	0.76	0.24

Table 18: Snowballs statistics during WFI-TVAC1

TVAC1 NOM OPS + COLD QUAL + TO COLD QUAL+ NOM_OPS_noise+COLD_QUAL_noise							
Detector	Hours	number of snowballs	Rate of Snowballs (snb/hr)	Number of non-repeated snowballs	Number of repeated snowballs	Non-repeated snowballs/ hr	Repeated snowballs/ hr
20663	12.83	12	0.935	12	0	0.935	0.000
20829	12.83	23	1.793	23	0	1.793	0.000
20833	12.83	30	2.338	30	0	2.338	0.000
21115	12.83	36	2.806	34	2	2.650	0.156
21319	12.83	33	2.572	31	2	2.416	0.156
21641	12.83	34	2.650	30	4	2.338	0.312
21643	12.83	18	1.403	18	0	1.403	0.000
21645	12.83	21	1.637	21	0	1.637	0.000
21813	12.83	29	2.261	27	2	2.105	0.156
21814	12.83	28	2.183	28	0	2.183	0.000
21815	15.19	39	2.568	37	2	2.436	0.132
21816	12.83	29	2.261	29	0	2.261	0.000
21946	12.83	29	2.261	25	4	1.949	0.312
21947	12.83	32	2.494	32	0	2.494	0.000
22067	12.83	32	2.494	28	4	2.183	0.312
22069	12.83	29	2.261	29	0	2.261	0.000
22078	12.83	31	2.416	31	0	2.416	0.000
22081	15.19	64	4.214	52	12	3.424	0.790
Total	235.64	549	2.33	517	32	2.19	0.14

Table 19: Snowballs statistics during WFI-TVAC2

TVAC2 NOM OPS + COLD QUAL + HOT QUAL + NOM OPS noise + COLD _QUAL noise +HOT QUAL Noise							
Detector	Hours	number of snowballs	Rate of Snowballs (snb/hr)	Number of non-repeated snowballs	Number of repeated snowballs	Non-repeated snowballs/ hr	Repeated snowballs/ hr

20663	18.18	33	1.815	31	2	1.705	0.110
20829	18.18	40	2.200	40	0	2.200	0.000
20833	18.18	43	2.365	43	0	2.365	0.000
21115	18.18	59	3.245	53	6	2.915	0.330
21319	18.18	50	2.750	50	0	2.750	0.000
21641	18.18	56	3.080	54	2	2.970	0.110
21643	18.18	51	2.805	45	6	2.475	0.330
21645	18.18	44	2.420	44	0	2.420	0.000
21813	18.18	38	2.090	34	4	1.870	0.220
21814	18.18	48	2.640	44	4	2.420	0.220
21815	18.18	46	2.530	46	0	2.530	0.000
21816	18.18	63	3.465	56	7	3.080	0.385
21946	18.18	44	2.420	42	2	2.310	0.110
21947	18.18	40	2.200	36	4	1.980	0.220
22067	18.18	64	3.520	57	7	3.135	0.385
22069	18.18	47	2.585	41	6	2.255	0.330
22078	18.18	60	3.300	57	3	3.135	0.165
22081	18.18	39	2.145	29	10	1.595	0.550
Total	327.32	865	2.64	802	63	2.45	0.19

14 CROSSTALK AND IPC

14.1 Inter-Pixel Capacitance (IPC)

Inter-pixel capacitance was measured at the DCL during SCA acceptance testing using a single pixel reset method and an Fe-55 method. The average signal in nearest neighbor pixels is reported. Results from the single pixel reset method were used for photon transfer gain correction.

Table 20: Acceptance Testing IPC Crosstalk

SCA #	SCA SN	IPC Crosstalk (%)
1	22081	1.220
2	21815	1.564
3	21946	1.477
4	21115	1.082
5	21816	1.694
6	20663	1.478
7	22069	1.379
8	21641	1.361
9	21813	1.755
10	22078	1.324
11	21947	1.387
12	20829	1.566
13	22067	1.439
14	21814	1.336
15	21645	1.246
16	21643	1.452
17	21319	1.850
18	20833	1.803

IPC was also measured during the tuning phase of the flight FPS TVAC test using the single pixel reset method. These results were used to correct the photon transfer gain calculated during FPS TVAC which were used throughout WFI TVAC data analysis.

Table 21: FPS TVAC IPC Crosstalk

SCA #	SCA SN	IPC Crosstalk (%)
1	22081	1.202
2	21815	1.467
3	21946	1.373
4	21115	1.101
5	21816	1.636
6	20663	1.297
7	22069	1.423
8	21641	1.348

9	21813	1.748
10	22078	1.339
11	21947	1.385
12	20829	1.551
13	22067	1.439
14	21814	1.322
15	21645	1.220
16	21643	1.444
17	21319	1.625
18	20833	1.562

14.2 Crosstalk

Data for measuring output-to-output and SCA-to-SCA crosstalk was collected during Flight FPS TVAC and consisted of injecting a signal pattern into the SCAs in a stable dark environment via the guide-window. The injected signal was placed in a diagonal pattern such that each output channel in an individual SCA read a non-zero signal that did not overlap with the injected signal from any other output channel. Additionally, the region where the signal was injected for a given SCA did not overlap with the injected signal region of any of the other SCAs.
Each science frame was read out in 32 blocks, each block having 128 rows. A 16x16 guide-window was used to inject a signal that mimics saturation of the SCA.
The average of two dark exposures was subtracted from the injected signal exposures to remove background signal. For each block of 128 rows, the mirror 16x16 regions of the injected signal in each SCA was normalized to the total signal of 100%, yielding the crosstalk between the reset channel of an SCA and the rest.
Analysis showed that the noise floor of the detectors during the dark exposures was too high for a 0.001% crosstalk signal to be detected. To verify this, additional analysis was performed with simulated crosstalk signals of 0.001%, 0.01%, and 0.05% shown as green points in the Figure below.

Figure 90: Example of crosstalk analysis for SCA 21815

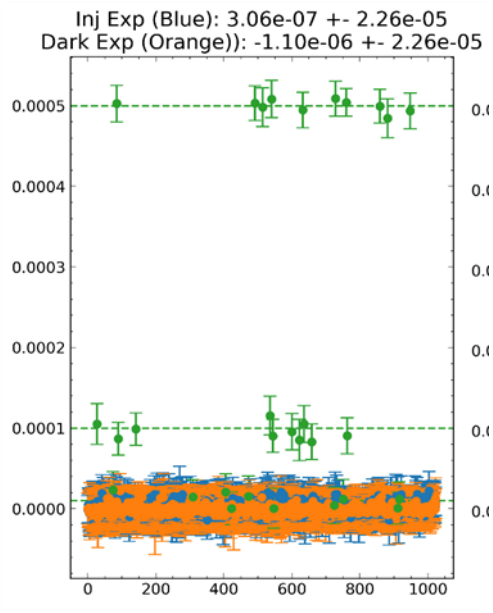

The overlap between the blue and orange points in the above plot show that the crosstalk data collected during flight FPS TVAC is indistinguishable from dark current. The simulated green points with 0.001% crosstalk signal are also dominated by dark current. The elevated green points using 0.01% and 0.05% signal show levels of crosstalk that theoretically would be detectable in this system.

15 ELECTRONICS GAIN

15.1 Summary

Electronics gain (or E-gain) was measured during the semiflight and flight FPS TVAC tests. The data were acquired by holding the SCAs in reset mode and applying varying reset voltages. Then slope of the pixel signal vs reset voltage is calculated in ADU/V and converted to mV/ADU or pixel capacitance in e-/V. SCA 22078 in MPA location 10 is an outlier.

Figure 91: E-gain per channel

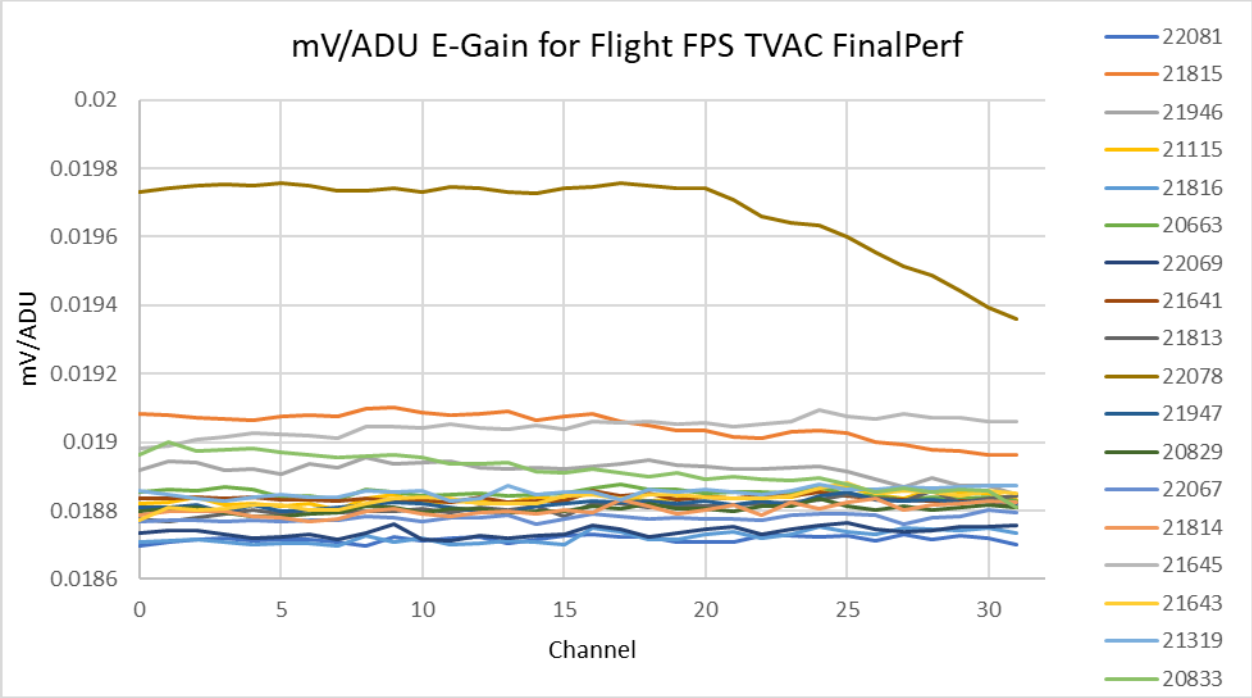

15.2 E-gain: SCA 10, 22078

The E-gain for SCA 10 is higher overall than the other detectors but decreases starting around channel 20. The figure below shows the E-gain per column, as opposed to the per channel view in figure above.

Figure 92: E-gain per column for SCA 10 (mV/ADU)

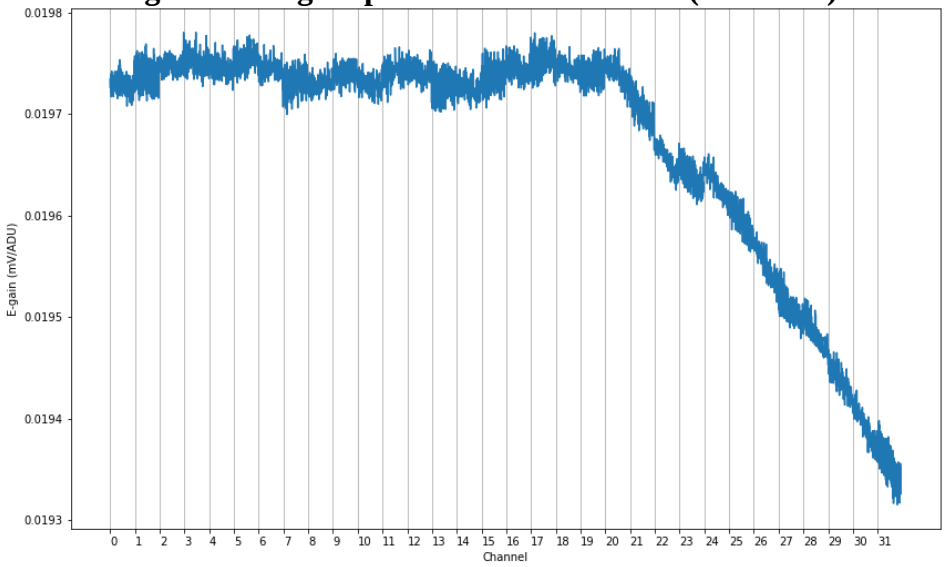

16 GUIDE WINDOWS

16.1 Summary

Each detector has a guide window mode that will be used for star tracking during the mission. Guide window functionality was verified during DCL SCA level testing and guide window data was collected throughout FPS and WFI TVAC testing. The SCAs support real-time programmable guide windows whose size, shape, and position can be customized. During FPS testing guide window data were collected for 16x16, 64x64, 100x100, 16x32, and 170x24 pixel guide windows.

16.2 Guide Window: SCA 12, 20829

SCA 20829 testing initially showed that the guide window was not functioning correctly. Changing the SCA readout to use a different reset mode produced valid guide window data and functionality of the guide window was recovered. *Summary of the Nancy Grace Roman Space Telescope Flight Detector Performance* (Mosby et al., 2025) has more information on operating the guide window for SCA 12.

16.3 Guide Window Noise

Transient fixed pattern noise in the guide windows for all SCAs is documented in risk RST-00447:

“The switch in mode to the guide mode appears to introduce an electrical transient on the pixels in the guide window that has strong pixel-to-pixel variation at a level of hundreds of electrons. This electrical transient is fixed spatially for a given guide window position and decays in time. The centroid of this spatially fixed pattern is likewise fixed, while the centroid of the guide star moves with the star. The centroid of the combination of these two different signals is biased and the derived motion of the star is less than the actual motion.”

Investigations into this behavior showed that when the detectors are operated in a different reset mode (center image in Figure 93) as opposed to the original reset mode (right image in Figure 93) the fixed pattern noise was significantly reduced.

Figure 93: Imaging a spot in full frame (left) and guide window mode. Right: original guide window reset mode. Center: improved guide window reset mode.

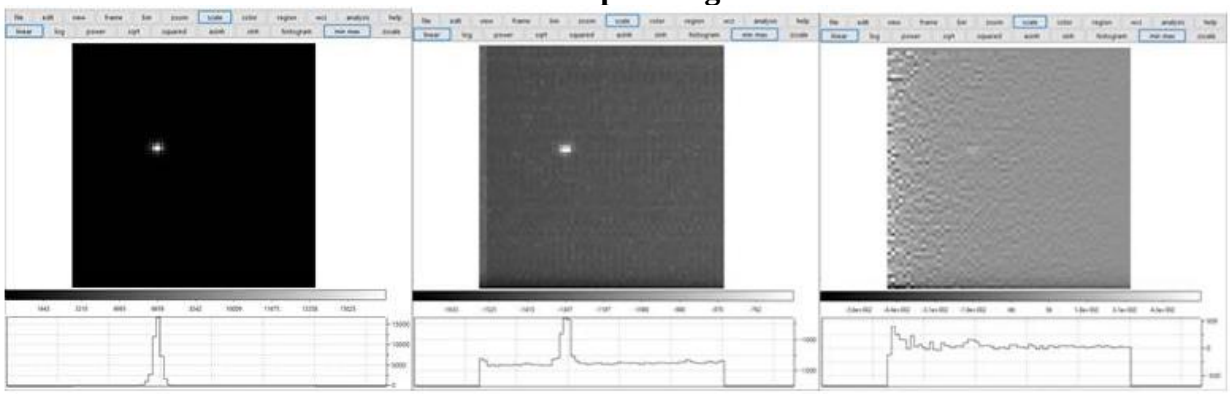

The guide window Multi-Accumulation (MA) tables were also updated to mitigate the fixed pattern noise:

"These multi-accum tables have been tested in the lab and on the WFI instrument during TVAC 1, and the resulting data exhibit the desired reduction in the amplitude of the fixed pattern noise transient."

WFI flight software was updated with these changes to the MA tables during Build 3.3, which was loaded onto the flight Instrument Control and Data Handlers (ICDHs) during execution of WOA-RST-WFI-4540.

17 BINARY OPERABILITY MASKS

17.1 Description

SCA requirements state that at least 95% of pixels across the entire Focal Plane shall be operable. The project defines an operable pixel as one that meets the following performance specifications:

- Dark Current: Less than 0.5 e-/px/s.
- Total Noise: Less than 12 e-/px.
- QE: Greater than 70% Measured from 400nm to 2800nm.
- Persistence: Less than 0.15 e-/s in median for an illumination of 50 ke and less than 0.50 e-/s for 300 ke in median and less than 0.8 e-/sec per pixel.

Additional operability constraints were defined during WFI TVAC1 and TVAC2 to improve image data analysis:

- Linearity: Maximum Normalized Residual (MNR) of classical nonlinearity correction less than 1%.
- Disconnected pixels: Slope of pixel signal during disconnected pixel test within 5σ of median value.
- Flat Field: For normalized flat fields, pixel value should be greater than zero.
- Gain: Does not fail per pixel gain calculation. Pixels that do fail gain calculation are classified as OTHER BAD PIXEL. These pixels belong to the population showing low noise and high nonlinearity discussed in Section 7.5.

The following flags were applied to create binary operability masks for all flight detectors:

- GOOD: 0
- GW_AFFECTED_DATA: 2**4
- PERSISTENCE: 2**5
- DEAD: 2**10
- HOT: 2**11
- LOW_QE: 2**13
- NONLINEAR: 2**16
- UNRELIABLE_SLOPE: 2**24
- OTHER_BAD_PIXEL: 2**30
- FLAT_FIELD: 2**18
- REFERENCE_PIXEL: 2**31

Table 22 summarizes the percentage of pixels passing requirements during the Flight Acceptance Test, Triplet Test, Semi-Flight TVAC, FPS, WFI-TVAC1, and WFI-TVAC2.
Some caveats should be considered when comparing the data:

- SCA temperatures during the flight acceptance and triplet tests were set at 95K.

- SCA temperatures during Nom Ops plateaus during WFI-TVAC1 (89K) and WFI-TVAC2 (89.5K) were lower than in Nom Ops of FPS TVAC (95K).

- Rework of the WFI between WFI-TVAC1 and WFI-TVAC2 caused the background/dark measurement in WFI-TVAC2 to be lower compared to WFI-TVAC1.

- Temperatures were slightly higher during WFI-TVAC2 (89.5K) compared to WFI-TVAC1 (89K).

- Operability was not defined in the same way during all tests:
  - During Flight Acceptance Test, Triplet Test, and FPS only masks of high dark current, total noise, persistence, and QE were applied.
  - During WFI-TVAC 1 and 2, masks for linearity, flat field, and pixels with failed gain were also applied.

- Detectors 22081 and 21115 were not included in the Triplet test and Semi-Flight FPS TVAC.

- Detector 20829 was not included in the Semi-Flight TVAC Test.

- Detector 21115 has low operability compared to the other SCAs due to its high illumination persistence behavior, which initially disqualified it from the flight cohort. It was substituted into location 4 on the FPA at the direction of the DD-ARB.

Table 22: Percentage passing requirements for Flight detectors during the Flight Acceptance Test, Triplet test, Semi-flight TVAC, FPS, WFI-TVAC1, and WFI-TVAC2

SCU#	SCA	FAT (95K)	Triplet (95K)	SemiFlight (95K)	FPS (95K)	WFI-TVAC1 (89 K)	WFI-TVAC2 (89.5K)
1	22081 (*)	97.63			97.50	97.80	97.70
2	21815	99.31	99.39	99.38	99.32	99.35	99.30
3	21946	98.80	99.00	98.82	98.80	98.96	98.89
4	21115	84.78			84.57	84.76	84.70
5	21816	99.13	99.29	99.25	99.21	99.33	99.26
6	20663	99.23	98.97	99.00	98.97	99.25	99.16
7	22069	98.54	98.71	98.53	98.47	98.59	98.53
8	21641	99.20	99.28	99.24	99.22	99.22	99.17
9	21813	99.34	99.43	99.46	99.41	99.42	99.35
10	22078	98.98	98.90	98.41	98.39	98.51	98.40
11	21947	99.00	99.08	99.11	99.09	99.21	99.15
12	20829 (**)	99.48	99.43		99.40	99.50	99.43
13	22067	98.27	98.19	98.03	97.92	98.13	98.06
14	21814	99.21	99.34	99.31	99.25	99.31	99.25
15	21645	99.47	99.47	99.45	99.41	99.49	99.42
16	21643	99.43	99.39	99.42	99.36	99.46	99.38
17	21319	99.26	99.36	99.45	99.37	99.45	99.38
18	20833	99.32	99.28	99.22	99.17	99.21	99.19

Figure 94: Percentage of pixels passing requirements for Flight detectors

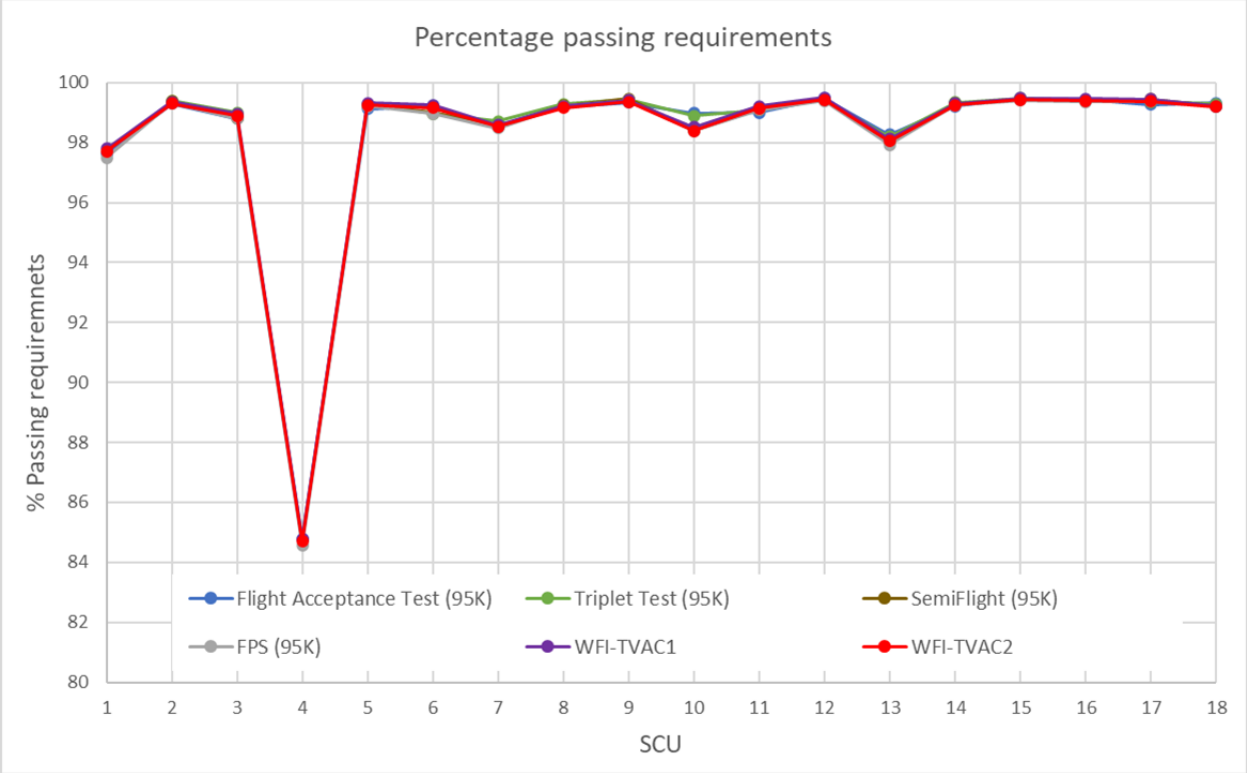

Figure 95: Same as previous Figure but with different scale.

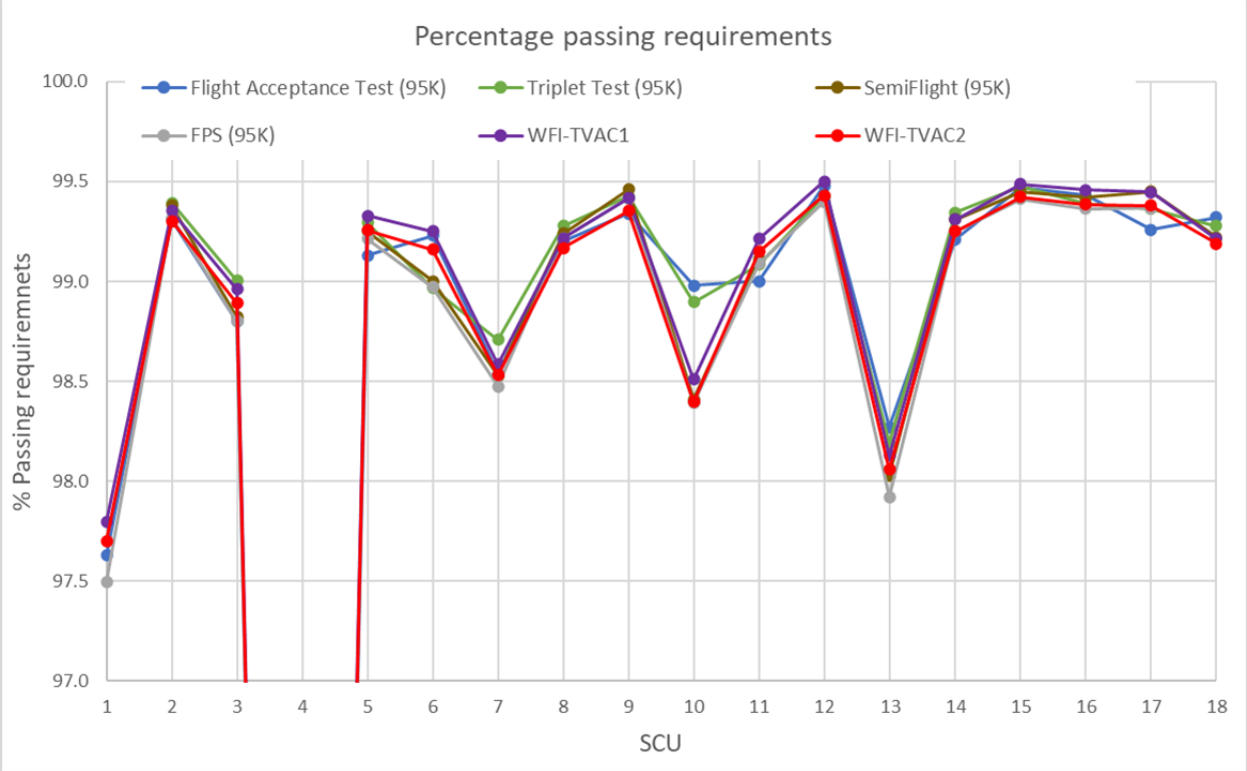

18 TENDRILS

The hybridized SCAs for RST are held together by epoxy between the silicon multiplexer Read Out Integrated Circuit (ROIC) and the HgCdTe crystal detector layer. Underfill of the epoxy is postulated to create “tendril” features from dendritic voids in the RST flight detectors. Tendril features seen in the middle of the SCAs are usually associated with a central defect in the detector material.

Features like "tendrils" appear on all RST Flight detectors. As shown in the flat-field image of SCA 21815 (SCU02) in Figure 96 most come from the top or right side of the detectors, and some come from the middle.

Figure 96: Flat Field image of detector 21815, SCU02 (left). Zoom-in in the central region of one of the tendrils (right).

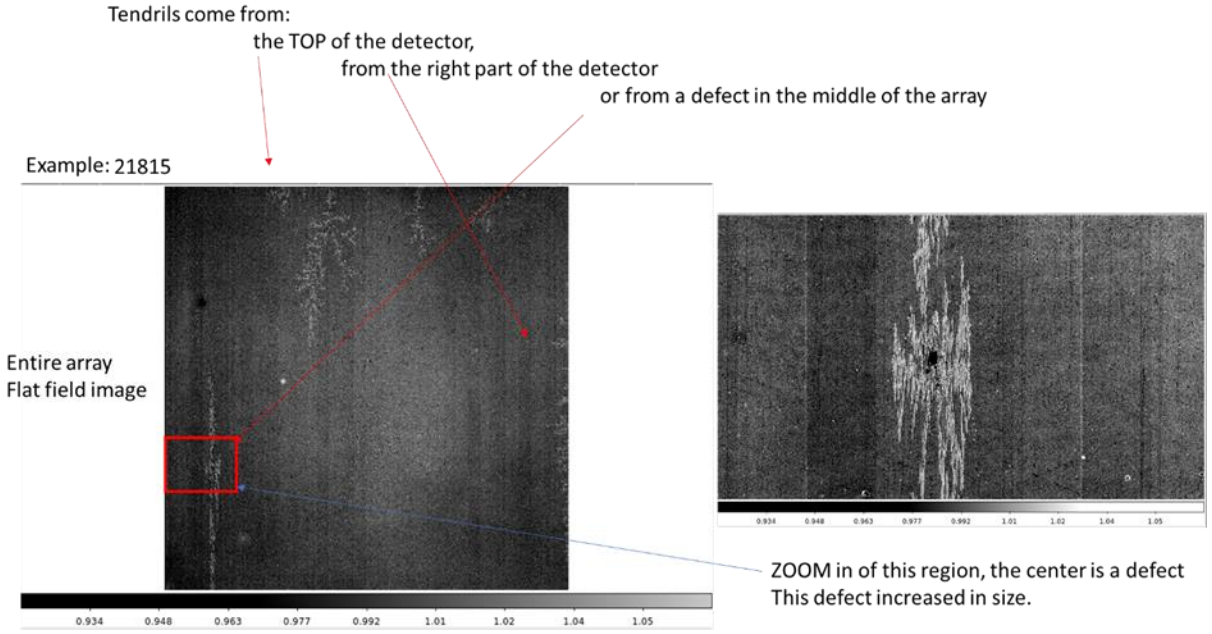

In the dark image from the same detector (Figure 97), the feature in the middle of the "tendrils" increased in size between the Flight Acceptance, Triplet, and Semi-Flight TVAC tests.

Figure 97: Dark current images of 21815 (SCU02). The feature in the middle of one of the "tendrils" increased in size. Units: e/sec.

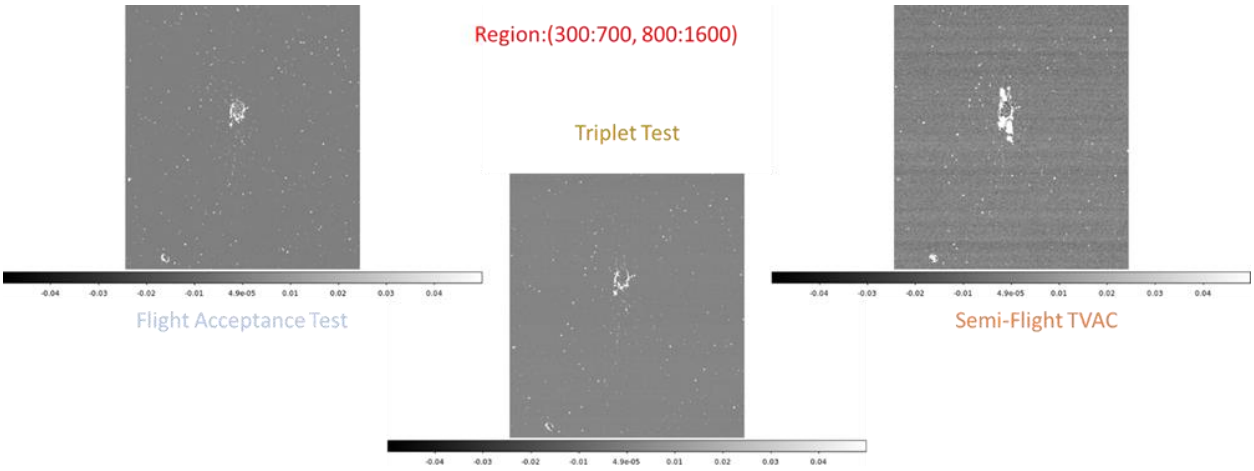

Some tendrils in the middle of the array have a "cross" shape, as shown in the flat field images of detector 21641 (SCU08), 21816 (SCU05), 21946 (SCU03). Other tendrils in the middle of the array have a more complicated shape, as in Figure 99.

Figure 98: Examples of tendrils in the center of the array with a cross-shape: Detectors 21641 (SCU08), 21816 (SCU05), and 21946 (SCU03).

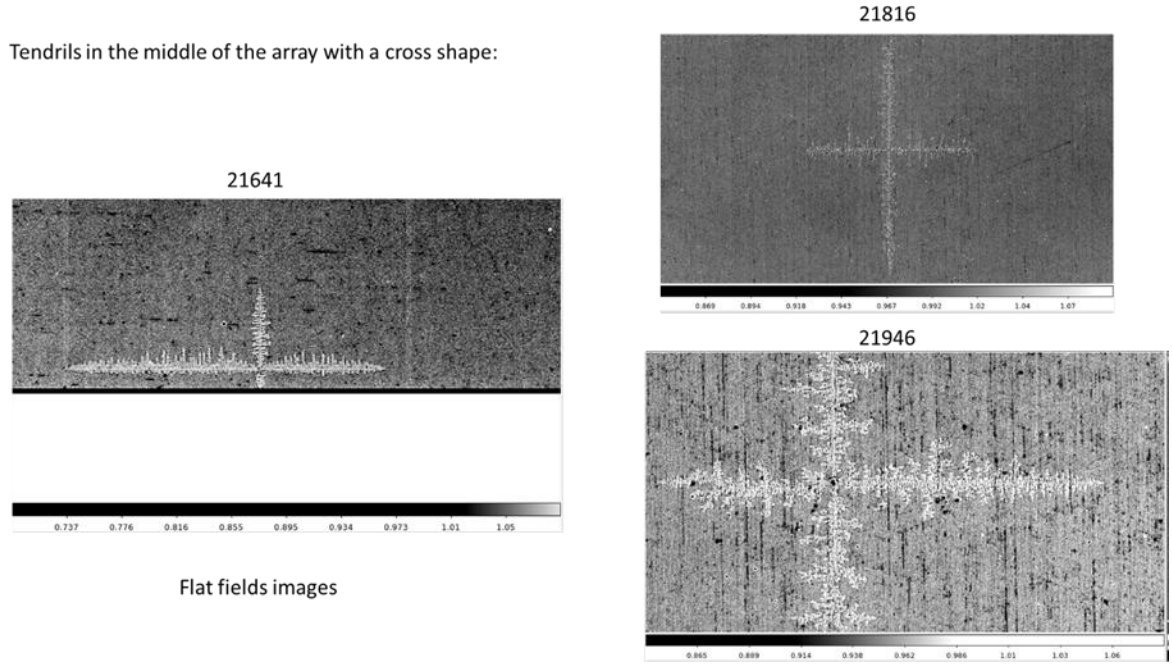

Figure 99: Example of tendrils in the middle of the detector that do not look like a cross: Detector 21813 (SCU09)

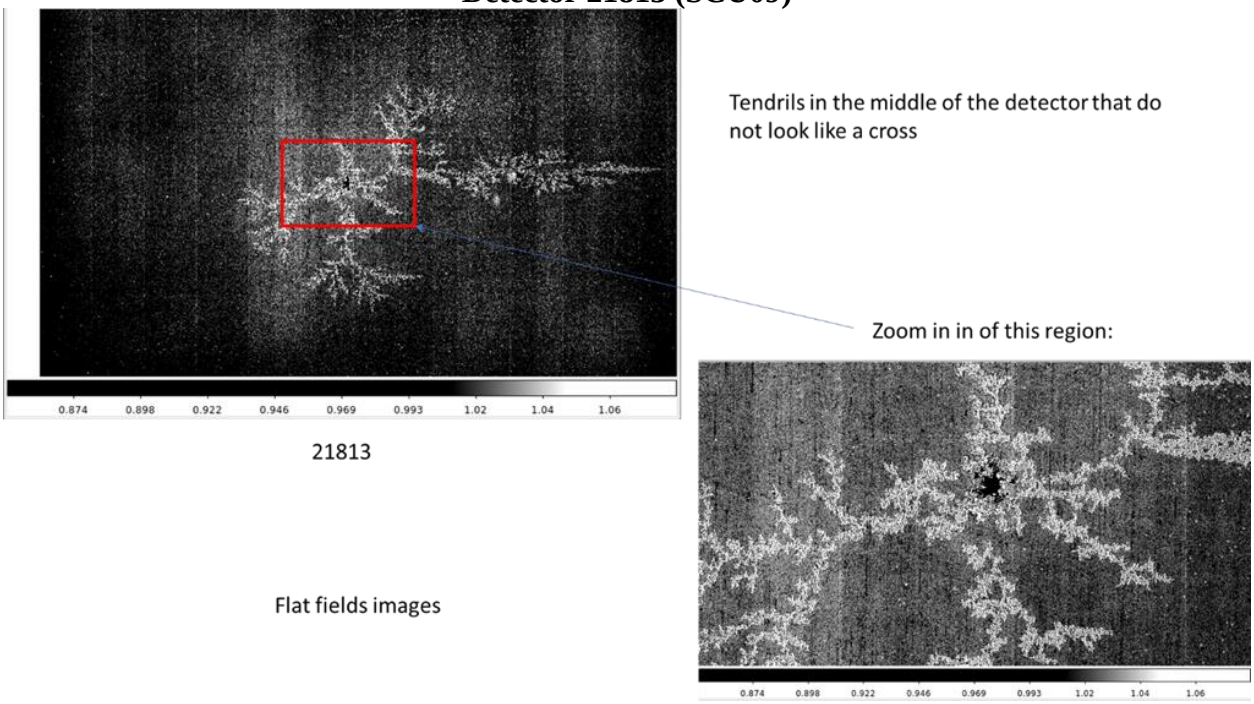

Figure 100 shows the first frame of the persistence cube for detector 22078 (SCU10): The tendrils (and the regions around them) have lower persistence and appear darker than other areas of the detector.

Figure 100: Example of lower persistence in the tendrils and surrounding regions just after illumination: Detector 22078 (SCU10).

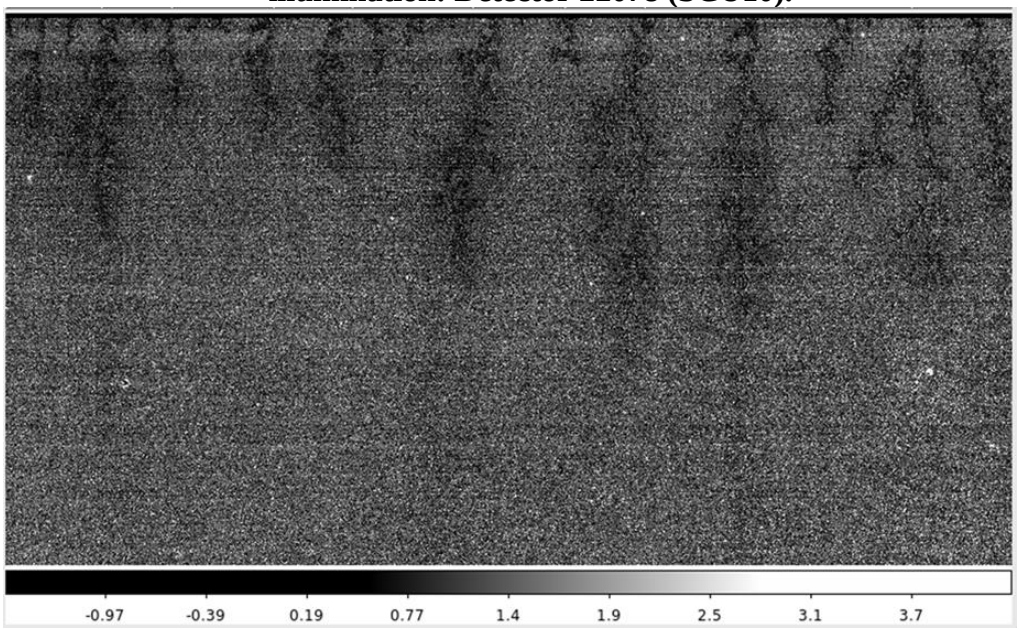

It is worth noting that on detector 22081 (SCU01), one of the areas where disconnected pixels increased over time, appears in regions around the tendrils on the right side of the detector (see Disconnected Pixels section).

An additional observation from a member of the Roman Detectors Working Group is that interpixel capacitance derived from flatfield analysis is lower in observed tendril features.

19 CONCLUSION

This document is a collaborative effort between SCA data analysts, many of whom have been involved with the RST detectors since the early stages of the project. The SCAs in the flight FPA are the best out of a large selection of candidates, and together they have made the WFI a powerful tool for future science with excellent imaging capabilities. But they are not without their quirks. The goal of the FPA Handbook is to document these characteristics in context with the pre-launch test campaigns so that future SCA data analysts can know what to expect.

Appendix A Guide Window Locations

The following tables contain the coordinates for the Guide Window (GW) locations during FPS and WFI level guide window science testing. These locations were chosen to highlight known features within the detectors to verify guide window data validity.

Table 23: 16x16 GW Size and Position

SCA	GW X Start Expected	GW Y Start Expected	SCA	GW X Start Expected	GW Y Start Expected
1	4040	2088	10	661	3680
2	487	1248	11	965	186
3	2422	272	12	1583	3170
4	3782	3354	13	2254	668
5	3907	1706	14	1841	2356
6	564	990	15	3791	3018
7	2090	3147	16	3437	2144
8	1136	595	17	385	626
9	1500	1458	18	538	2664

Table 24: 64x64 GW Size and Position

SCA	GW X Start Expected	GW Y Start Expected	SCA	GW X Start Expected	GW Y Start Expected
1	4016	2064	10	637	3656
2	463	1224	11	941	162
3	2398	248	12	1559	3146
4	3758	3330	13	2230	644
5	3883	1682	14	1817	2332
6	540	966	15	3767	2994
7	2066	3123	16	3413	2120
8	1112	571	17	361	602
9	1476	1434	18	514	2640

Table 25: 100x100 GW Size and Position

SCA	GW X Start Expected	GW Y Start Expected	SCA	GW X Start Expected	GW Y Start Expected
1	3950	1998	10	571	3590
2	397	1158	11	875	96
3	2332	182	12	1493	3080
4	3692	3264	13	2164	578
5	3817	1616	14	1751	2266
6	474	900	15	3701	2928
7	2000	3057	16	3347	2054
8	1046	505	17	295	536
9	1410	1368	18	448	2574

Table 26: 170x24 GW Size and Position

SCA	GW X Start Expected	GW Y Start Expected	SCA	GW X Start Expected	GW Y Start Expected
1	4036	2011	10	657	3603
2	483	1171	11	961	109
3	2418	195	12	1579	3093
4	3778	3277	13	2250	591
5	3903	1629	14	1837	2279
6	560	913	15	3787	2941
7	2086	3070	16	3433	2067
8	1132	518	17	381	549
9	1496	1381	18	534	2587

Table 27: 16x32 GW Size and Position

SCA	GW X Start Expected	GW Y Start Expected	SCA	GW X Start Expected	GW Y Start Expected
1	4032	2088	10	653	3680
2	479	1248	11	957	186
3	2414	272	12	1575	3170
4	3774	3354	13	2246	668
5	3899	1706	14	1833	2356
6	556	990	15	3783	3018
7	2082	3147	16	3429	2144
8	1128	595	17	377	626
9	1492	1458	18	530	2664

Appendix B External Citations

The following is a list of citations to publications outside of NASA TDMS in order of appearance.

Gregory Mosby, Bernard Rauscher, Chris Bennett, Edward S. Cheng, Stephanie A. Cheung, Analia N. Cillis, David A. Content, David A. Cottingham, Roger D. Foltz, John D. Gygax, Robert J. Hill, Jeffrey W. Kruk, Jon S. Mah, Lane A. Meier, Chris A. Merchant, Laddawan R. Miko, Eric C. Piquette, Augustyn Waczynski, Yiting Wen, "*Properties and characteristics of the Nancy Grace Roman Space Telescope H4RG-10 detectors*," J. Astron. Telesc. Instrum. Syst. 6(4) 046001 (19 November 2020)
https://doi.org/10.1117/1.JATIS.6.4.046001

Mosby G., Tonn S., Chervenak J., Hill B., Zandian M., Rauscher B., Kruk J., et al., "*Resolving the dark current anomaly in the Nancy Grace Roman Space Telescope focal plane*". Space Telescopes and Instrumentation 2024: Optical, Infrared, and Millimeter Wave. 2024, vol. 13092, Art. no. 130923K. doi:10.1117/12.3020366.
https://ui.adsabs.harvard.edu/abs/2024SPIE13092E..3KM/abstract

Ori Fox, Augustyn Waczynaski, Yiting Wen, Roger D. Foltz, Robert J. Hill, Randa A. Kimble, Eliot Malumuth, Bernard J. Rauscher, "*The Fe X-ray Energy Response of Mercury Cadmium Telluride Near-Infrared Detector Arrays".* NASA Technical Reports Server. August 24, 2013.
https://ntrs.nasa.gov/citations/20090027672

P.-E. Crouzet, R. Kohley, R. Barbier, P. Strada, B. Shortt, T. Beaufort, S. Blommaert, B. Butler, G. Van Duinkerken, J. Ter haar, F. Lemmel, C. van der Luijt, H. Smit, "*Euclid H2RG detectors: Impact of crosshatch patterns on photometric and centroid errors* ," Proc. SPIE 10709, High Energy, Optical, and Infrared Detectors for Astronomy VIII, 107090Q (6 August 2018);
https://doi.org/10.1117/12.2312692

Martinka, M., Almeida, L. A., Benson, J. D., & Dinan, J. H. (2001). "*Characterization of cross-hatch morphology of MBE (211) HgCdTe*". Journal of Electronic Materials, 30(6), 632-636.
https://doi.org/10.1007/BF02665847

Charles Shapiro, Eric Huff, Roger Smith, "*Intra-pixel response characterization of a HgCdTe near infrared detector with a pronounced crosshatch pattern*," Proc. SPIE 10709, High Energy, Optical, and Infrared Detectors for Astronomy VIII, 1070936 (12 July 2018).
https://doi.org/10.1117/12.2314431

Eric C. Piquette, "*The Effect of Contact Resistance on Short Wavelength Infrared Focal Plane Array Noise*". *J. Electron. Mater.* **53**, 5858–5864 (10 July 2024).
https://doi.org/10.1007/s11664-024-11296-2

A. Canipe, M. Robberto, B. Hilbert. "*A New Non-Linearity Correction Method for NIRCam*", Technical Report JWST-STScI 005167. (20 January 2017).

https://www.stsci.edu/files/live/sites/www/files/home/jwst/documentation/technical-documents/_documents/JWST-STScI-005167.pdf

Gregory Mosby Jr., Bob Hill, Analia Cillis, Roger Foltz, Chris Bennett, Mario Cabrera, Michael Hickey, Chris Merchant, Augustyn Waczynski, Yiting Wen, Bernie Rauscher, Edward J. Wollack, Jeff Kruk, John Auyeung, Joshua Schlieder, Eric Switzer, Maxime Rizzo, Neil Zimmerman, Edward Cheng, Craig Cabelli, Eric Piquette, Jianmei Pan, Mark Farris, Anders Petersen, John Gygax, Colin Stuart, Dave Cottingham, Jonathan Mah, Stephanie Cheung, Lane Meier, Daniel Kelly, Steven Mann, "Summary of the Nancy Grace Roman Space Telescope flight detector performance," J. Astron. Telesc. Instrum. Syst. 11(1) 011210 (28 March 2025) https://doi.org/10.1117/1.JATIS.11.1.011210

Appendix C Abbreviations and Acronyms

Abbreviation/ Acronym	DEFINITION
ACADIA	ASIC for Control and Digitization for Astronomy
ACM	Alignment Compensation Mechanism
ADU	Analog-Digital Units
ASIC	Application Specific Integrated Circuit
ASIST	Advanced Spacecraft Integration and System Test
BAE	British Aerospace
BOL	Beginning of Life
CDS	Correlated Double Sampling
CDF	Cumulative Density Function
CFA	Combinatorial Flux Addition
CM	Configuration Management
CNL	Classical Nonlinearity
CPT	Comprehensive Performance Test
CRNL	Count-Rate Nonlinearity
DCL	Detector Characterization Lab
DD-ARB	Detector Degradation Anomaly Review Board
EMI	Electromagnetic Interference
FAT	Flight Acceptance Test
FEDS	Front End Data System
FDNL	Flux Dependent Nonlinearity
FPA	Focal Plane Assembly
FPE	Focal Plane Electronics
FPGA	Field Programmable Gate Array
FPS	Focal Plane System
GSFC	Goddard Space Flight Center
GW	Guide Window
H4RG	HAWAII-4RG
HgCdTe (aka MCT)	Mercury Cadmium Telluride
HST	Hubble Space Telescope
ICDH	Instrument Control and Data Handler
InGaAs	Induim Gallium Arsenic
IPC	Inter-Pixel Capacitance
JWST	James Webb Space Telescope
LOLO	Lamp On Lamp Off
MA	Multi-Accumulation
MCU	Multiplexer Control Unit
MNR	Maximum Normalized Residual

Abbreviation/ Acronym	DEFINITION
MPA	Mosaic Plate Assembly
OTP	Optical Test Procedure
PED	Photoemissive Defect
PRT	Platinum Resistance Thermometer
PSF	Point Spread Function
QE	Quantum Efficiency
ROIC	Read Out Integrated Circuit
RST	Roman Space Telescope
SCA	Sensor Chip Assembly
SCE	Sensor Control Electronics
SCEA	Sensor Control Electronics Assembly
SCU	SCE Control Unit
SLD	Superluminescent Diode
SORC	Stimulus of Ray Cones
sRCS	Simplified Relative Calibration System
SUTR	Sample Up the Ramp
TBD	To Be Determined
TBR	To Be Revised
TBS	To Be Scheduled
TIS	Teledyne Imaging Systems
TVAC	Thermal Vacuum
WFC3	Wide Field Camera 3
WFI	Wide Field Instrument
ZTO	Zero Time Offset